National Library of Canada
Acquisitions and Bibliographic Services Branch
395 Wellington Street
Ottawa, Ontario
K1A 0N4

Bibliothèque nationale du Canada
Direction des acquisitions et des services bibliographiques
395, rue Wellington
Ottawa (Ontario)
K1A 0N4

Your file Votre référence

Our file Notre référence

NOTICE

The quality of this microform is heavily dependent upon the quality of the original thesis submitted for microfilming. Every effort has been made to ensure the highest quality of reproduction possible.

If pages are missing, contact the university which granted the degree.

Some pages may have indistinct print especially if the original pages were typed with a poor typewriter ribbon or if the university sent us an inferior photocopy.

Reproduction in full or in part of this microform is governed by the Canadian Copyright Act, R.S.C. 1970, c. C-30, and subsequent amendments.

AVIS

La qualité de cette microforme dépend grandement de la qualité de la thèse soumise au microfilmage. Nous avons tout fait pour assurer une qualité supérieure de reproduction.

S'il manque des pages, veuillez communiquer avec l'université qui a conféré le grade.

La qualité d'impression de certaines pages peut laisser à désirer, surtout si les pages originales ont été dactylographiées à l'aide d'un ruban usé ou si l'université nous a fait parvenir une photocopie de qualité inférieure.

La reproduction, même partielle, de cette microforme est soumise à la Loi canadienne sur le droit d'auteur, SRC 1970, c. C-30, et ses amendements subséquents.

Canada

UNIVERSITY OF ALBERTA

IRON SILICIDES IN THIN FILM AND BULK DIFFUSION COUPLES

By

NEIL ROLAND BALDWIN ©

A thesis submitted to the Faculty of Graduate Studies and Research in partial fulfillment of the requirements for the degree of MASTER OF SCIENCE

IN

METALLURGICAL ENGINEERING

DEPARTMENT OF MINING, METALLURGICAL AND PETROLEUM ENGINEERING

EDMONTON, ALBERTA

SPRING 1995

National Library
of Canada

Acquisitions and
Bibliographic Services Branch

395 Wellington Street
Ottawa, Ontario
K1A 0N4

Bibliothèque nationale
du Canada

Direction des acquisitions et
des services bibliographiques

395, rue Wellington
Ottawa (Ontario)
K1A 0N4

Your file *Votre référence*

Our file *Notre référence*

THE AUTHOR HAS GRANTED AN IRREVOCABLE NON-EXCLUSIVE LICENCE ALLOWING THE NATIONAL LIBRARY OF CANADA TO REPRODUCE, LOAN, DISTRIBUTE OR SELL COPIES OF HIS/HER THESIS BY ANY MEANS AND IN ANY FORM OR FORMAT, MAKING THIS THESIS AVAILABLE TO INTERESTED PERSONS.

L'AUTEUR A ACCORDE UNE LICENCE IRREVOCABLE ET NON EXCLUSIVE PERMETTANT A LA BIBLIOTHEQUE NATIONALE DU CANADA DE REPRODUIRE, PRETER, DISTRIBUER OU VENDRE DES COPIES DE SA THESE DE QUELQUE MANIERE ET SOUS QUELQUE FORME QUE CE SOIT POUR METTRE DES EXEMPLAIRES DE CETTE THESE A LA DISPOSITION DES PERSONNE INTERESSEES.

THE AUTHOR RETAINS OWNERSHIP OF THE COPYRIGHT IN HIS/HER THESIS. NEITHER THE THESIS NOR SUBSTANTIAL EXTRACTS FROM IT MAY BE PRINTED OR OTHERWISE REPRODUCED WITHOUT HIS/HER PERMISSION.

L'AUTEUR CONSERVE LA PROPRIETE DU DROIT D'AUTEUR QUI PROTEGE SA THESE. NI LA THESE NI DES EXTRAITS SUBSTANTIELS DE CELLE-CI NE DOIVENT ETRE IMPRIMES OU AUTREMENT REPRODUITS SANS SON AUTORISATION.

ISBN 0-612-01578-5

Canada

UNIVERSITY OF ALBERTA

RELEASE FORM

NAME OF AUTHOR: **Neil Roland Baldwin**

TITLE OF THESIS: **Iron Silicides in Thin Film and Bulk Diffusion Couples**

DEGREE: **Master of Science**

YEAR THIS DEGREE GRANTED: **1995**

Permission is hereby granted to the University of Alberta Library to reproduce single copies of this thesis and to lend or sell such copies for private, scholarly or scientific research purposes only.

The author reserves all other publication and other rights in association with the copyright in the thesis, and except as hereinbefore provided neither the thesis nor any substantial portion thereof may be printed or otherwise reproduced in any material form whatever without the author's prior written permission.

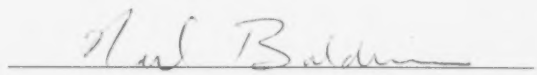

Apt. 1902, 8515 - 112 Street
Edmonton, Alberta, Canada T6G 1K7

DATE: Dec. 1, 1994

UNIVERSITY OF ALBERTA

FACULTY OF GRADUATE STUDIES AND RESEARCH

The undersigned certify that they have read, and recommend to the Faculty of Graduate Studies and Research for acceptance, a thesis entitled **IRON SILICIDES IN THIN FILM AND BULK DIFFUSION COUPLES** submitted by **NEIL ROLAND BALDWIN** in partial fulfillment of the requirements for the degree of **MASTER OF SCIENCE** in **METALLURGICAL ENGINEERING**.

Dr. D. G. Ivey
Supervisor

Dr. B. M. Patchett

Dr. M. L. Wayman

Dr. R. P. W. Lawson

DATE: Nov. 16/94.

Abstract

Iron silicides, the intermetallic compounds of Fe and Si, are the focus of this thesis. Iron silicides, especially β-$FeSi_2$, are currently of research interest to the microelectronics industry, which is constantly searching for new materials with which to make improved and novel devices. The silicide β-$FeSi_2$ is a direct band gap semiconductor that may prove useful in the construction of optoelectronic devices.

The literature on iron silicides, iron silicide films, and the growth of these compounds is reviewed. Published data on the techniques, conditions and kinetics of growth of iron silicides have been compiled. The known epitaxial relationships of iron silicide films with Si substrates are listed and the issues of impurities and iron/silicide islanding are discussed.

The experimental investigation of iron silicides was divided into two components -- the thin film work and the bulk diffusion couple work. For the first of these two parts, thin films of Fe were deposited on Si substrates and annealed to produce iron silicide layers. The growth and microstructure of the silicides were recorded, using transmission electron microscopy (TEM), as functions of time and annealing temperature. The nucleation controlled growth kinetics of β-$FeSi_2$ were directly confirmed by TEM pictures of circular colonies of this phase. Under some conditions, FeSi films displayed preferential orientation to the substrates. The phase Fe_3Si was observed to form continuous layers that were microstructurally separate from the α-Fe solid solution layers.

The bulk diffusion couple work involved the construction and annealing of diffusion couples made from pieces of pure Fe and single crystal Si. Annealing was done at 710°C, 750°C and 800°C for times ranging from 72 to 2070 hours. The diffusion couples yielded information on the stability and compositional ranges of the iron silicides at these temperatures. The activation energy for diffusion controlled β-$FeSi_2$ layer growth was calculated to be 0.83 eV or 80.4 kJ/mol. Results concerning Fe_3Si were in disagreement with the present Fe-Si phase diagram. The silicide was found to be stoichiometric with almost no compositional range, while the phase diagram predicts a wide range of homogeneity.

Acknowledgements

Dr. Douglas Ivey has encouraged and assisted me throughout the completion of this study and for this I am deeply appreciative. On many occasions I turned to him for advice or a valuable second opinion and he spent a great deal of his time having these discussions with me.

The Natural Sciences and Engineering Research Council of Canada, the Alberta Microelectronic Centre (AMC), and the University of Alberta have all provided the financial assistance that allowed me to undertake this degree. I wish to thank the staff of AMC also for their work in depositing the Fe films and sawing the wafers.

Ms. Tina Barker deserves thanks for the patience and trust she demonstrated during my use of the scanning electron microscope and Mr. Bob Konzuk kindly provided me with the benefit of his machining knowledge.

My wife, Petra, continues to be a constant source of ideas and enthusiasm and I am grateful for her involvement in this and all that I do.

Table of Contents

Chapter 1

Introduction 1

Chapter 2

Literature Survey 3

2.1 Methods of Silicide Formation 3

2.2 Substrate Cleanliness 3

2.3 Annealing Procedures 4

2.4 Properties of Iron Silicides 5

2.4.1 Fe_3Si 5

2.4.2 ε-FeSi 6

2.4.3 $FeSi_{(CsCl)}$ 6

2.4.4 α-$FeSi_2$ 6

2.4.5 β-$FeSi_2$ 6

2.4.6 γ-$FeSi_2$ 7

2.5 Iron Film Formation 7

2.6 Conditions of Silicide Formation with Solid Phase Epitaxy (SPE) 9

2.7 Silicide Kinetic Growth Behaviours with Solid Phase Epitaxy 12

2.8 Conditions of Silicide Formation with Reactive Deposition Epitaxy (RDE) .. 13

2.9 Conditions of Silicide Formation Using Ion Implantation 14

2.10 Conditions of Formation/Transformation of the Pseudomorphic Silicides ... 15

2.11 Epitaxial Relationships of Iron Silicides 17

2.12 The Islanding Problem 19

2.13 Impurities and Oxide Layers 20

2.14 Growth Kinetics -- Bulk Versus Thin Film Diffusion Couples 22

Chapter 3

Thin Film Diffusion Couples 26

3.1 Experimental Methods 26

3.1.1 Deposition of Iron 26

3.1.2 Annealing 26

3.1.3 Transmission Electron Microscopy (TEM) Sample Preparation 28

3.1.4 Characterization 30

3.2 Results and Discussion 30
3.2.1 Conditions and Sequence of Silicide Formation 30
3.2.2 FeSi Preferred Orientation 36
3.2.3 Silicide Grain Sizes and Morphology 37
3.2.4 Performance of SiO_2 Capping Layer 39
3.3 Conclusions and Recommendations 39

Chapter 4
Bulk Diffusion Couples 59
4.1 Experimental Methods 59
4.1.1 Fabrication of Couples 59
4.1.2 Annealing 60
4.1.3 Metallographic Preparation 61
4.1.4 Characterization 62
4.2 Results and Discussion 63
4.2.1 EDS Work: Phases and Compositions 63
4.2.2 Fe_3Si in the Fe-Si Phase Diagram 69
4.2.3 Growth Kinetics of β-$FeSi_2$ and FeSi 70
4.2.4 Other Interesting Results 72
4.3 Conclusions and Recommendations 74

Chapter 5
Comparison of Thin Film and Bulk Diffusion Couple Results 92

References 93
Appendix A 98
Appendix B 103

List of Tables

Table 2-1 Conditions of Formation of Iron Silicides by Solid Phase Epitaxy..... 10

Table 2-2 Epitaxial Relationships for β-$FeSi_2$ on Si..... 18

Table 3-1 Relative Layer Thicknesses for Equivalent Iron Content..... 31

Table 3-2 Annealing Conditions Studied with Transmission Electron Microscopy..... 31

Table 3-3 Orientation of FeSi Film..... 36

Table 3-4 Mean Grain Sizes in Iron Silicide Films..... 38

Table 4-1 Gibbs Free Energies of Oxidation..... 61

Table 4-2 Bulk Diffusion Couples Produced..... 63

Table 4-3 Phases Observed in Bulk Diffusion Couples..... 64

Table 4-4 Number of EDS Measurements Taken..... 65

Table 4-5 Ranges of EDS Results on Iron Silicides..... 66

Table 4-6 Computed Compositional End-Points, Ranges and Gradients of the Silicides..... 67

Table A-1 Lattice Positions of α-Fe..... 98

Table A-2 Lattice Positions of α_2 Fe_3Si..... 98

Table A-3 Lattice Positions of $FeSi_{(CsCl)}$..... 98

Table A-4 Lattice Positions of α_1 Fe_3Si..... 99

Table A-5 Lattice Positions of ε-FeSi 99

Table A-6 Lattice Positions of β-$FeSi_2$ 100

Table A-7 Lattice Positions of γ-$FeSi_2$ 102

Table B-1 Crystallographic Interplanar Spacings for α-Fe 103

Table B-2 Crystallographic Interplanar Spacings for α_1 Fe_3Si 103

Table B-3 Crystallographic Interplanar Spacings for α_2 Fe_3Si 103

Table B-4 Crystallographic Interplanar Spacings for FeSi 104

Table B-5 Crystallographic Interplanar Spacings for β-$FeSi_2$ 104

List of Figures

Figure 1-1 Fe-Si Phase Diagram..... 2

Figure 2-1 Three Epitaxial Growth Modes..... 24

Figure 2-2 Example of the Effect of Oxygen on Silicide Kinetics..... 25

Figure 3-1 System for Location of Sample Pieces in Original Wafers..... 42

Figure 3-2 Construction of Cross-sectional Transmission Electron Microscopy Samples..... 43

Figure 3-3a As-Deposited Fe Film on Si(111) Shown in Cross-Section..... 44

Figure 3-3b As-Deposited Fe Film on Si(111) Shown in Plan View..... 44

Figure 3-4a Fe Film Annealed at 300°C for 1 Hour Shown in Cross-Section..... 45

Figure 3-4b Fe Film Annealed at 300°C for 2 Hours Shown in Cross-Section..... 45

Figure 3-4c Fe Film Annealed at 300°C for 3 Hours Shown in Cross-Section..... 45

Figure 3-4d Fe Film Annealed at 300°C for 2 Hours Shown in Plan View..... 45

Figure 3-5 Selected Area Diffraction Pattern From Fe Film Annealed at 300°C for 2 Hours..... 46

Figure 3-6 Schematic Showing Iron Silicide Film Thicknesses as a Function of Annealing Time at 400°C..... 47

Figure 3-7 Fe Film Annealed at 400°C for 30 Minutes Shown in Cross-Section..... 48

Figure 3-8 Selected Area Diffraction Pattern From Fe Film Annealed at 400°C for 30 Minutes..... 49

Figure 3-9 Fe Film Annealed at 400°C for 1 Hour Shown in Cross-Section..... 50

Figure 3-10 Fe Film Annealed at 400°C for 2 Hours Shown in Cross-Section..... 51

Figure 3-11 Selected Area Diffraction Pattern From Fe Film Annealed at 400°C for 2 Hours..... 52

Figure 3-12 Fe Film Annealed at 500°C for 15 Minutes Shown in Cross-Section..... 53

Figure 3-13 Subcritical Nucleus of β-$FeSi_2$ in Fe Film Annealed at 500° C for 1 Hour and Shown in Cross-Section..... 54

Figure 3-14 β-$FeSi_2$ Colony in Fe Film Annealed at 600°C for 1 Hour and Shown in Plan View..... 55

Figure 3-15 High Magnification Plan View of Thin Film FeSi..... 56

Figure 3-16 High Magnification Plan View of Thin Film β-$FeSi_2$..... 57

Figure 3-17 Selected Area Diffraction Pattern From Fe Film Annealed at 650°C for 30 Minutes..... 58

Figure 4-1 Diagram of Steel Clamp Plate for Bulk Diffusion Couple..... 76

Figure 4-2 Backscattered Electron Image of a Fe-Si Bulk Diffusion Couple..... 77

Figure 4-3 Fe Concentration Profile in the Si of a Bulk Diffusion Couple..... 78

Figure 4-4 Si Concentration Profile in the α-Fe of a Bulk Diffusion Couple..... 79

Figure 4-5 Experimental and Theoretical Concentration Profiles Across Fe-Si Bulk Diffusion Couples..... 80

Figure 4-6 Compositional Profile Across Fe_3Si of a Bulk Diffusion Couple Annealed at 710°C for 1518 Hours..... 81

Figure 4-7 β-$FeSi_2$ Layer Thickness as a Function of Annealing Time at 710°C in Bulk Diffusion Couples..... 82

Figure 4-8 β-$FeSi_2$ Layer Thickness as a Function of Annealing Time at 750°C in Bulk Diffusion Couples..... 83

Figure 4-9 β-$FeSi_2$ Layer Thickness as a Function of Annealing Time at 800°C in Bulk Diffusion Couples..... 84

Figure 4-10 Plot to Determine the Activation Energy of β-$FeSi_2$ Growth in the Bulk Diffusion Couples..... 85

Figure 4-11 FeSi Layer Thickness as a Function of Annealing Time at 710°C in Bulk Diffusion Couples..... 86

Figure 4-12 FeSi Layer Thickness as a Function of Annealing Time at 750°C in Bulk Diffusion Couples..... 87

Figure 4-13 FeSi Layer Thickness as a Function of Annealing Time at 800°C in Bulk Diffusion Couples..... 88

Figure 4-14 Backscattered Electron Image of Bulk Diffusion Couple with β-$FeSi_2$ Locally Consumed..... 89

Figure 4-15 Secondary Electron Image of Bulk Diffusion Couple with Step Change in β-$FeSi_2$ Layer Thickness..... 90

Figure 4-16 Schematic Explaining the Consumption of the β-$FeSi_2$ Layer in Bulk Diffusion Couples Subjected to Sufficiently Long Anneals..... 91

Chapter 1 Introduction

According to the Fe-Si binary phase diagram shown in Figure 1-1 [1], iron forms numerous stable compounds when reacted with silicon. These compounds, known as iron silicides, are Fe_3Si (α_1 and α_2 forms), Fe_2Si, Fe_5Si_3, FeSi, β-$FeSi_2$, and α-$FeSi_2$.

The primary reason for the rise in research interest in iron silicides is that the β-$FeSi_2$ phase is thought to be a direct band gap semiconductor [2-15]. If thin films of β-$FeSi_2$ can be prepared so as to have microstructures and electrical properties of sufficiently high quality, this compound could be used to fabricate components in opto-electronic devices. Most important to note is that this semiconductor could be bonded directly to single crystal silicon substrates and therefore devices made from it would be compatible with existing silicon-based integrated circuit technology. If the perceived potential of β-$FeSi_2$ is to be realized, it is important that the technology be developed so that the phase can be grown not only on top of silicon, but epitaxially on top of silicon. Without epitaxy, the microstructure, and consequently the electrical properties, will likely be too irregular to allow reliable device fabrication.

Before large areas of epitaxial iron silicides can be reproducibly formed on silicon, more research must be committed towards understanding many basic aspects of the Fe-Si interactions which have been previously ignored in the haste to form β-$FeSi_2$. The work described in this thesis examined iron silicides by two approaches. Thin films of iron silicides were grown on Si substrates and thicker layers of iron silicides were grown in bulk Fe-Si diffusion couples. The main objective of the thin film part was to record the iron silicide growth kinetics and microstructures as functions of time and temperature. The bulk diffusion couple work was originally intended to provide estimates for the diffusion coefficients through the various iron silicides. Although it did not prove possible to get this data, the bulk couple work did provide other worthwhile results. A value for the activation energy of β-$FeSi_2$ (diffusion controlled) growth was calculated and results indicate a revision necessary to the Fe-Si equilibrium phase diagram.

Chapters 2 through 4 are the three major sections of this thesis: Chapter 2 is a survey of the literature published to date, including studies of thin film iron silicides as well as more general papers written on silicide growth kinetics. Much of the knowledge of iron silicide films applies equally to bulk crystals. No literature on the fabrication of bulk Fe-Si diffusion couples could be found. Chapter 3 describes the research done on thin film iron silicides and Chapter 4 is concerned with the study of iron silicides in bulk diffusion couples. Chapter 5 is a brief comparison of the thin film and bulk diffusion couple results.

This figure has been removed to comply with copyright restrictions. The phase diagram can be found in reference [1].

Figure 1-1. Fe-Si phase diagram [1].

Chapter 2 Literature Survey

2.1 Methods of Silicide Film Formation

There are various methods that have been employed to produce thin film iron silicides on (or near the surface of) single crystal Si. Most of these can be placed in one of three categories -- solid phase epitaxy (SPE), reactive deposition epitaxy (RDE), and ion beam methods.

Solid phase epitaxy involves depositing a layer of pure iron onto a clean Si surface at (or near) room temperature. The iron may be deposited by sputtering, thermal evaporation, electron beam evaporation, or by using a Knudsen cell in a molecular beam epitaxy (MBE) system. In any case, the resulting sample, consisting of an iron film on a silicon substrate, is then annealed to react the two elements and form intermediate silicide phases. During the annealing of SPE samples, the silicide phases present change as the metals continue to interdiffuse.

By contrast, reactive deposition epitaxy is the depositing of iron onto a Si surface held at elevated temperature. The metals react as the deposition occurs and therefore no subsequent anneal is done. Again the iron can be deposited by a variety of techniques. Another way of doing RDE is to co-deposit both Fe and Si, instead of only Fe. This can be done with an MBE system or by using two electron beam sources, as in [12,16]. By carefully controlling the deposition parameters, the two metals can be deposited at specific flux ratios to achieve desired stoichiometry.

Ion beams of Ar^+ can be used to ion mix the as-deposited SPE samples prior to the anneal. The Ar^+ bombardment is believed to speed the annealing reactions by intermixing the Si and Fe atoms near the interface, and to break up impurity concentrations or SiO_2 layers at the interface that could hinder interdiffusion [17]. Another way of using ion beams in iron silicide synthesis, is to implant Fe^+ ions into the Si substrate. This provides atomic mixing and avoids the wafer surface impurities altogether, as they are left at the surface while the silicides form underneath. Annealing can be performed during iron implantation, afterwards, or both.

2.2 Substrate Cleanliness

It is generally acknowledged that the cleanliness of the Si surface is an important factor in thin film silicide preparation. Higher degrees of surface cleanliness correspond to

faster reaction, lower reaction temperatures and greater reproducibility. Therefore methods have been developed to ensure that the Si surface is as clean as possible before iron deposition. *Ex situ* cleaning techniques are applied prior to placing the Si wafers within the vacuum environment for iron deposition. *In situ* cleaning procedures are done in the vacuum just prior to deposition.

Ex situ cleaning usually consists of a chemical clean in an acid solution. This solution may be a mixture of acids but most commonly it is simply diluted HF, which etches off any SiO_2 that is on the wafer. The wafer is then rinsed in deionized water and blown dry with a pure inert gas.

In situ cleaning can be done using numerous methods. The Si substrate may be heated to 800°C, or even higher temperatures, to desorb any SiO_2 still on the surface and speed surface diffusion of Si atoms. Since an atomically flat surface is the lowest energy configuration, this high temperature heating will lead to surfaces as flat as possible, given the small unintentional misorientations (typically <0.5°) of the wafers. Often a low flux of Si is directed toward the substrate surface during this heating to assist in surface repair. Alternatively, surface contamination can be removed by argon sputtering of the wafer. Oxygen plasma cleaning involves using gases which react with the contaminants to form volatile compounds that can be pumped away.

It is of benefit to researchers to be able to verify that the Si surface is in fact clean before proceeding with deposition. The most common way to check that the surface is atomically clean is with low energy electron diffraction (LEED). Atomically clean Si(111) surfaces reconstruct to display a sharp 7x7 pattern [18], while clean Si(100) surfaces give a sharp 2x1 pattern, as shown in [19].

2.3 Annealing Procedures

Since SPE is the most commonly used technique to fabricate thin films of iron silicides, and SPE requires subsequent annealing of the thin film couples, annealing methods will be briefly mentioned. Annealing can be done *in situ*. That is, the sample can be annealed in the same vacuum environment in which the deposition was just carried out. This is the preferable way to anneal an SPE sample as the iron is not exposed to oxygen or other contaminants at all, even at room temperature. But if *in situ* annealing is not possible, as-deposited samples can be annealed in vacuum furnaces or in purified flowing N_2 or Ar. Conventional annealing involves heating the sample to a predetermined temperature and maintaining that temperature for typically one half to three hours. This time is sufficiently

long that all parts of the annealing sample are at the one annealing temperature for most of the heating cycle. Rapid thermal annealing, in contrast, involves heating the sample very rapidly to a more elevated temperature for a much shorter period of time, ranging from fractions of a second to several minutes. Usually the annealing, done by conventional furnace anneal or rapid thermal anneal, involves only one heat treatment. However, some experiment evidence suggests that two-step annealing may be advantageous [17,20,21]. An initial anneal at relatively low temperature helps Fe and Si to interdiffuse across the interface and disperses interface impurities, but is not sufficiently hot to promote phase changes. The second annealing step at higher temperature yields the silicide formation, as usual, but gives better results than without the first step.

2.4 Properties of Iron Silicides

The main emphasis of almost all research on iron silicides is on the β-$FeSi_2$ phase. Therefore almost all experiments in which iron silicides are formed are carried out below 800°C. The major exception to this are the efforts of a few researchers to form α-$FeSi_2$ and then convert this to the semiconducting β-$FeSi_2$. Since most research is done below 800°C, neither Fe_5Si_3 nor Fe_2Si have been reported anywhere in the iron silicide film literature. These two silicides are excluded from this summary of iron silicide properties. The lattice positions of the iron silicides are given in Appendix A.

2.4.1 Fe_3Si

According to the Fe-Si phase diagram (Figure 1-1), Fe_3Si has a wide range of stoichiometry and two different crystal structures, denoted α_1 and α_2 [1]. The two forms of this silicide are supposedly not distinct phases from the α-Fe solid solution, but rather simply ordered alterations of α-Fe. The α_1 form is cubic and has a lattice parameter of 0.5640 nm, its Pearson symbol being cF16 and its space group $Fm\bar{3}m$. The α_2 form is also cubic and has a lattice parameter of 0.2840 nm. Its Pearson symbol is cP2 and its space group is $Pm\bar{3}m$.

2.4.2 ε-FeSi

The monosilicide, ε-FeSi, is commonly referred to as simply FeSi and will be for the remainder of this thesis. The silicide melts at 1410°C and has a 1:1 Fe:Si stoichiometry with a compositional range of less than 1 atomic percent [1]. The crystal structure is cubic and the lattice parameter is 0.449 nm. The Pearson symbol is cP8 and the space group is $P2_13$.

2.4.3 $FeSi_{(CsCl)}$

It was only very recently that this form of the monosilicide was discovered [22]. It is denoted as $FeSi_{(CsCl)}$ because it has a CsCl crystal structure. This metallic phase does not appear in the equilibrium phase diagram because it only occurs as very thin layers arranged pseudomorphically on Si substrates.

2.4.4 α-$FeSi_2$

The crystal structure of α-$FeSi_2$ is tetragonal with lattice parameters of a = b = 0.264 nm and c = 0.783 nm. The Pearson symbol for this structure is tP3 and the space group is P4/mmm. The composition is not stoichiometric and about 13 % of the Fe lattice spots are vacant [1]. The α-$FeSi_2$ phase exhibits metallic electrical conduction. The temperature below which this form of $FeSi_2$ is not stable is not precisely known, but is believed to be approximately 937°C [1].

2.4.5 β-$FeSi_2$

Unlike the α form, the low temperature form of iron disilicide is stoichiometric in composition and has almost no compositional range. The orthorhombic crystal structure is a distorted CaF_2 structure with lattice parameters of a = 0.9863 nm, b = 0.7791 nm and c = 0.7833 nm [23]. The Pearson symbol is oC48 and the space group is Cmca. This form of $FeSi_2$ is stable below about 982°C. The density of β-$FeSi_2$ is 4.93 g/cm^3 [23].

Experimental evidence has shown quite conclusively that β-$FeSi_2$ is a direct band gap semiconductor. The first widely acknowledged measurement of the band gap of β-$FeSi_2$ was made by Bost and Mahan [2]. Using optical data, they estimated the band gap to be a minimum of 0.87 eV and confirmed that the band gap is direct. They later revised

this number to 0.89 eV after further study showed that their value for the index of refraction used in the band gap calculation had originally been in error [3]. The electronic structure of β-$FeSi_2$ was probed with high-resolution electron energy-loss spectroscopy (HREELS) by Rizzi *et al.* [4,5], who suggested a direct band gap 0.8 eV based on their electron spectroscopy data. The band gap was again verified to be direct by Lefki *et al.*, who also used optical measurements to arrive at a band gap of 0.85 eV [6]. Another recent study of electronic structure led to a suggested β-$FeSi_2$ band gap value of 1.0 ± 0.2 eV [7], while Dimitriadis *et al.* concluded that photothermal deflection spectroscopy results pointed to a direct band gap of 0.85 eV [8]. Other research investigations that have verified the direct nature of the band gap and measured its value include [10-15].

To complement the experimental work being done, some researchers have done theoretical calculations to predict the electronic structure of β-$FeSi_2$. Christensen concluded that the silicide is a semiconductor with a direct band gap of approximately 0.8 eV [9]. However Eppenga [24] has written that the disilicide should have a band gap of only 0.44 eV and that this gap is actually indirect, making β-$FeSi_2$ unsuitable for promising light-emitting applications.

2.4.6 γ-$FeSi_2$

A third form of the disilicide, dubbed γ-$FeSi_2$, was first reported just three years ago by Onda *et al.* [25]: MBE was used to form films of $FeSi_2$ at only 250°C and these films were found to be metallic and to possess a CaF_2 crystal structure. This was in agreement with the calculations of Christensen [9], who predicted the possibility of a $FeSi_2$ phase with a CaF_2 structure and a lattice constant of 0.5389 nm. Other research groups have since confirmed the existence of γ-$FeSi_2$ [26-29].

Like $FeSi_{(CsCl)}$, γ-$FeSi_2$ is stable only as a very thin film which can be stabilized by the Si substrate. Upon sufficient heating the fluorite structure of the γ form is distorted into the orthogonal β form, the critical temperature depending on the film thickness [25,30,31].

2.5 Iron Film Formation

There are thought to be three epitaxial growth modes which are thermodynamically possible during the deposition of metal atoms on a clean semiconductor substrate surface [32]. These are (i) layer-by-layer growth (also called Frank-van der Merwe growth), (ii)

three-dimensional island growth (or Volmer-Weber growth) and (iii) a combination of an interface covering of one monolayer and three-dimensional island growth (Stranski-Krastanov growth mode). Figure 2-1 provides a schematic representation of the three growth modes.

Urano *et al.* [33,34] were among the first to study the growth of thin iron films on single crystal silicon. They used Auger electron spectroscopy (AES), low-energy electron diffraction (LEED) and angle resolved ultraviolet photoelectron spectroscopy (ARUPS) to monitor the formation of iron films on Si(111) and concluded that the growth mode was layer-by-layer. For Fe films of less than one monolayer (ML) thickness, iron atoms appeared to remain at the surface for temperatures as high as 600°C with no interdiffusion between the Si and Fe. Films of Fe thicker than one ML seemed to interdiffuse with the Si upon low temperature annealing, leaving a single ML remaining at the surface. It was also reported that this single ML film of Fe at the surface took on a pseudomorphic configuration, the Fe atoms arranged as if a continuation of the Si lattice.

A later investigation by Kennou *et al.* using similar spectroscopic methods, did not identify the growth mode of Fe on Si as layer-by-layer [35]. Iron film growth on the substrate was concluded to be of the three-dimensional island mode. Furthermore, interdiffusion between the Fe and Si was found to be considerable, even at room temperature. It should be noted that Fe was deposited onto Si(100), rather than Si(111), as in [33,34].

But other experimental results by Gallego *et al.* point to the layer-by-layer growth mechanism [36,37]. Their AES data showed that the Fe atoms completed one layer at a time on the Si(100) substrate at room temperature. Regarding the interdiffusion of the two elements, ion scattering spectroscopy results showed Si was present at the outer surface after the deposition of several ML of Fe. The AES data suggested considerable dissolution of Si in the Fe film during metal deposition (with a cold substrate). It has been noted by Gallego *et al.* [36] that there is contradiction with the results of Kennou *et al.* [35].

After observing the deposition of Fe on Si(111) at room temperature by means of AES, Lagomarsino *et al.* [38] have suggested the only growth mechanism not previously considered -- Stranski-Krastanov growth. The authors note that their conclusion is different from those of [35] and [36,37], and point out that they used Si(111) substrates instead of Si(100) and that during the other investigations of [35-37] no means, other than the usual quartz microbalance, was used to determine the amount of Fe actually deposited on the Si surfaces.

Using the scanning tunneling microscope (STM) instead of AES, Brodde *et al.* have obtained direct images of the early stages of Fe film growth on an atomically clean Si(111) surface [19]. They observed the Fe to form three dimensional islands during room temperature deposition. These islands were of irregular size and shape, when compared to similar islands formed during the deposition of Ag (which does not react with Si) on Si(111). This led to the conclusion that considerable intermixing with Si , or possibly even compound formation, was occurring at room temperature.

2.6 Conditions of Silicide Formation with SPE

This section and numerous sections to follow discuss the conditions under which the iron silicides have been observed to form as thin films or small particles. The experimental results of many research groups are categorized by the method used to form the silicides. A special section is devoted to the two new pseudomorphically stabilized phases, γ-$FeSi_2$ and $FeSi_{(CsCl)}$.

Iron silicides are most commonly formed by the room temperature deposition of an Fe film on a Si substrate and a subsequent annealing to promote interdiffusion and compound formation. This is the solid phase epitaxy (SPE) technique previously mentioned. When a bulk diffusion couple comprised of two metals is annealed, all the possible intermetallic compounds which are stable at that temperature can be expected to form layers between the metals and remain there simultaneously, given sufficient time. However it is now widely accepted that, in many systems, an annealed thin film binary diffusion couple will not exhibit all the phases at once that would be expected from the appropriate equilibrium phase diagram. In fact, often only one intermetallic compound forms at a time, the silicides appearing one by one in a reproducible sequence [39]. This is generally assumed to be the case for the Fe-Si system. Most researchers do not seem to check whether the growth period of different iron silicides overlaps somewhat. Certainly all of the "equilibrium" iron silicides have never been observed to exist simultaneously in a thin film diffusion couple. By now, thin film iron silicides have been formed by SPE by many researchers, with most reporting the same formation sequence. (The only major point of contention currently is which phase forms first in ultrathin films of only 1-4 monolayers.) This formation sequence is explained in the following:

Some researchers report that one of the ordered Fe_3Si structures forms prior to FeSi formation [8,17,21,36,40]. Because the α_1 and α_2 structures are generally viewed as being ordered forms of the α-Fe solid solution, rather than distinct phases, many

investigators do not seem to view Fe_3Si as a phase of much interest. The majority of studies that have not reported Fe_3Si formation have not claimed to have searched for it either. Therefore there is no clear evidence at this time of a real discrepancy in the SPE literature with regard to Fe_3Si. The monosilicide, FeSi, is the next compound formed. It grows to consume all the Fe_3Si film and, as annealing continues at sufficiently high temperature, is completely consumed itself by the β-$FeSi_2$ phase. This silicide remains stable to higher temperatures, whereupon it is progressively transformed into the metallic α-$FeSi_2$ form, which has an even higher atomic percentage of Si than β-$FeSi_2$ because ~13% of its Fe sites are vacant.

Table 2-1: Conditions of Formation of Iron Silicides by Solid Phase Epitaxy

Data Source	Fe dep. (nm)	Si orient.	UHV anneal	Temperature (°C)			Fe_3Si observed
				FeSi	β-$FeSi_2$	α-$FeSi_2$	
[21]	30	both	no	400	600	800	yes
[17]	30	both	no	--	--	--	yes
[40]	100	both	no	450	550	--	yes
[8]	150	100	no	700	750	950	yes
[36]	1.1	100	yes	325	450	--	yes
[41]	1.6	100	yes	--	600	--	no
[4]	2.0	111	yes	400	550	--	no
[42]	2.4	111	yes	400	550	--	no
[35]	2.5	100	yes	--	527	--	no
[43]	4.0	111	yes	--	527	--	no
[44]	3.0	111	yes	400	500	--	no
[44]	2.0	111	yes	200	500	--	no

Table 2-1 summarizes the results of many of the SPE experiments done in which the phases formed and the formation temperatures were recorded. The table includes only results from room temperature depositions of pure Fe onto single crystal Si wafers followed by annealing. In some experiments substrates are heated (RDE), amorphous Si is deposited on the substrate or on the Fe, or the sample is rapidly thermally annealed. The results of such experiments are not included in Table 2-1. The thickness of the Fe layer initially deposited is indicated, since it is apparent that the limited supply of one reactant can influence the phases which are formed. In the third column of the table, the substrate

orientation is shown. "Both" means both (111) and (100) wafers were used. The next column of the table indicates those experiments in which the annealing step was done in UHV (10^{-10} torr or better) and the as-deposited samples were not exposed to the atmosphere prior to annealing. It has become apparent that vacuum conditions can greatly influence results with iron silicides and therefore should be borne in mind when considering experimental findings. The temperatures at which the phases first appear are given in degrees Celsius. A space in the table with no entry signifies that the temperature of formation or the presence of the phase was not recorded -- not that the phase was systematically checked for and was proven to have not formed. To the best of this author's knowledge, no one has ever reported a different phase formation sequence for SPE experiments with Fe-Si thin film couples. The observance of the ordered Fe_3Si structure is indicated in the last column. Not all of the investigators attempted to determine if Fe_3Si was present.

It must be borne in mind that each of the above experiments has been conducted with slightly different conditions and procedures than the others. Nevertheless, the collected results from the SPE experiments show that:

(1) The same formation sequence has always occurred when a thin film of Fe has been deposited at room temperature on single crystal Si and annealed in vacuum. No other sequence has ever been reported.

(2) There seems to be little difference between formation temperatures for (111) Si substrates and for (100) Si substrates. Of the sources in the table, none reported a meaningful difference in formation temperatures for Si(100) and Si(111) and this is why the results were lumped together in the table.

(3) The Fe_3Si disorder-order transformation seems to occur in most cases. In the experiments done with the very thin Fe layers, the researchers were usually focussing on the formation of β-$FeSi_2$ and admittedly were not concerned with checking for the presence of Fe_3Si.

(4) Most work has reported FeSi to first appear in the range of 400-450°C.

(5) Most work has reported β-$FeSi_2$ to first appear in the range of 500-600°C.

(6) As predicted by the phase diagram, α-$FeSi_2$ does not seem to form until quite high temperatures. This means that it should be easy to avoid its formation when the semiconducting disilicide is the desired product.

(7) On average, the UHV experiments report lower phase formation temperatures.

2.7 Silicide Kinetic Growth Behaviors with SPE

Surprisingly little work has been done on the kinetics of the growth of iron silicides. The kinetic growth behavior of a growing thin film phase can be determined by making systematic measurements of the layer thickness after different annealing times. One of the few experiments done involving such a procedure is summarized in the 1975 paper by Lau *et al.* [40]. Rutherford backscattering spectrometry (RBS) was used to measure the thickness of FeSi formed as 100-150 nm thick Fe films on single crystal Si were annealed. It was observed that the FeSi growth rate was inversely proportional to its thickness -- that is, the growth was parabolic with time, indicating that the rate controlling step is probably diffusion across the silicide. The activation energy for FeSi growth was calculated from the kinetic data to be 1.67 ± 0.15 eV or 161 ± 14 kJ/mol. By inert marker experiments, the same researchers found that Si is the dominant diffuser in the formation of FeSi. Formation rates of FeSi seemed to be slightly higher on the Si(111) substrates than on the Si(100) substrates. The β-$FeSi_2$ phase was also formed in [40], but kinetic data was not given.

More recently, Radermacher *et al.* performed similar experiments to determine the growth kinetics of iron silicide films [45]. The main procedural difference between the two investigations is that Radermacher *et al.* used rapid thermal annealing instead of conventional annealing. The activation energy for FeSi diffusion controlled growth on Si(111) was determined to be 1.36 ± 0.25 eV or 131 ± 24 kJ/mol, somewhat lower than the result in [40]. The choice of annealing procedure was given as a possible factor in this difference. In order to estimate the activation energy for β-$FeSi_2$ growth, thickness measurements were taken from relatively thick disilicide films that had passed the nucleation controlled stage and moved on to diffusion controlled kinetics. The activation energy for the diffusion controlled growth of β-$FeSi_2$ films on Si(111) was calculated to be 2.6 ± 0.5 eV or 250 ± 50 kJ/mol.

The kinetics of β-$FeSi_2$ growth on single crystal and amorphous silicon (α-Si) have been compared by Erlesand *et al.* [46]. The β-$FeSi_2$ grown on crystalline (111) substrates demonstrated nucleation-controlled kinetics, while that grown on α-Si showed diffusion to be rate controlling. The activation energy for the growth of β-$FeSi_2$ on α-Si was calculated to be 1.5 ± 0.1 eV or 150 kJ $\pm$ 10 kJ/mol. A marker experiment similar to the one done in [40] was carried out to determine the major diffusing species during the formation of β-$FeSi_2$ from the FeSi. Marker displacement was small but appeared to show Si as the major diffuser. Optical micrographs of the disilicide/silicon interfaces supported the claim of

nucleation control on the Si(111) and diffusion control on the α-Si. The former interface was rough and marred by island structures, while the latter was smooth and uniform.

That a nucleation mechanism controls the growth of β-$FeSi_2$ from FeSi on crystalline Si is supported by Dimitriadis and Werner [8], who studied the surfaces of β-$FeSi_2$ films and concluded that "formation of β-$FeSi_2$ proceeds laterally by a nucleation-controlled exothermic reaction mechanism which results in a typical ring-shaped surface pattern." These ring-shaped patterns caused significant surface roughness which is typically an indication that growth is proceeding via a nucleation-controlled process, with nuclei of critical size suddenly expanding out in three dimensions. The most novel conclusion of the study [8] was the proposal that the heat released during the formation of β-$FeSi_2$ from FeSi travels outward from a nucleation site as a circular heat wave, which is not quickly conducted away because of the low thermal conductivities of the materials involved. The disilicide forms thus by an "explosive crystallization" process. The idea of such explosive crystallization was first suggested by Goetzberger [47].

2.8 Conditions of Silicide Formation with RDE

Compared to the study committed to the conditions of formation and the growth kinetics of iron silicides by SPE, the experimental study thus far devoted to RDE-grown iron silicides is minimal indeed. Numerous sources have reported using RDE to fabricate thin film iron silicides, but usually attention is focussed on the final product, rather than the formation process.

It has been found that depositing Fe onto the cleaned surface of Si(100), while the substrate is held at 350°C, will cause the appearance of β-$FeSi_2$ [36]. The disilicide is the first phase formed -- FeSi is not formed first as with SPE. The β-$FeSi_2$ may initially exist as three dimensional islands of reacted iron, separated by patches of clean Si surface. It is thought that there are still clean areas of Si because of the presence of a 2x1 LEED pattern, characteristic of an atomically clean Si(100) surface, during the RDE iron deposition [36].

Other work seems to indicate that an even lower temperature -- 235°C -- is sufficient to promote β-$FeSi_2$ formation during RDE [37].

However others have found that FeSi instead can be the first phase formed during RDE [48]. At 475°C, only 50 seconds was needed for FeSi to appear on the Si(100) surface. It seems that the rate at which iron is delivered to the surface must play a large role in determining which silicide forms at any given temperature.

Powalla and Herz have been performing experiments where the substrates are held at elevated temperatures and, unlike normal RDE, both Si and Fe are deposited simultaneously [12,16]. Their substrates, sapphire and Corning 7059 glass, did not need to be Si because Si for the silicidation was evaporated onto the surface. Evaporating the elements in a Fe:Si flux ratio of 1:2, they formed β-$FeSi_2$ as the first phase in this modified RDE process at 324°C.

2.9 Conditions of Silicide Formation Using Ion Implantation

There are several different schemes by which ion implantation has been employed to form silicides, the emphasis generally being placed on forming β-$FeSi_2$ as the final product. In some experiments, Fe^+ ions are implanted into Si substrates and the substrates are subsequently annealed [49,50]. In other experiments, the substrates are held at elevated temperatures during the Fe^+ implantation and sometimes annealed subsequently as well [14,45,49,51-54]. Another variation of the technique is to bombard the samples during annealing with a Si^+ flux [31,50]. Yet another method is to attempt to stimulate silicide formation by implanting Ar^+ ions which do not interact chemically but create many defect sites and speed the interdiffusion of the metals [55]. Whatever the procedure of choice, there seems to be a consensus among those working on these techniques that ion bombardment speeds silicide reactions in two ways. First, either through direct injection or by Ar^+ mixing, the ion beams create a mixed layer of Fe-Si. This makes long range diffusion of large amounts of material, as occurs in SPE, unnecessary and this has advantages. Reactions are not limited by the speed with which material can diffuse across very long distances and the crucial diffusion flux cannot be intercepted at any point by layers of contamination, again a problem typical of SPE methods. The second way that ion beams can speed the formation of silicides is through the energy they inject in the form of local defects and disorder. Defects sites and local disorder can provide the energy necessary for silicides to nucleate, especially phases such as β-$FeSi_2$ which is known to be hampered in its kinetics by a large activation energy of nucleation.

There are many different parameters in these types of experiments and so it is difficult to compare experimental results. But some of the conditions under which different iron silicides have been fabricated with these ion implantation methods are mentioned here.

Namavar *et al.* found that implanting Fe^+ ions into Si(100) at 350°C resulted in FeSi, while implanting Fe^+ at room temperature and annealing at 400°C for 30 minutes produced β-$FeSi_2$ [49].

Oostra *et al.* managed to produce continuous buried and surface layers of β-$FeSi_2$ by implantation at 320°C and annealing at 600°C for 30 minutes and 900°C for 30 or 150 minutes [51].

Radermacher *et al.* have found a slightly different route for producing continuous buried β-$FeSi_2$ layers with Fe^+ implantation [14,53,54]. Iron was implanted into Si(111) wafers held at 350°C. Much of the Fe in the as-implanted wafers was found to be precipitated as β-$FeSi_2$, not FeSi as in [49]. The samples were then rapid thermal annealed at 1150°C for 10 seconds. This produced α-$FeSi_2$ layers which were annealed to β-$FeSi_2$ by treatment at 750-800°C for up to 20 hours. It was claimed that this method, whereby the semiconducting phase is produced indirectly, leads to a better microstructure with fewer isolated precipitates.

Lin *et al.* have produced $FeSi_2$ precipitates -- γ and β forms -- in Si wafers by implanting Fe^+ at room temperature and then annealing, with or without bombardment of the sample by a Si^+ beam [31,50]. During 320°C annealing, Si^+ bombardment was necessary to produce $FeSi_2$, which was entirely of the γ structure. During 520°C anneals, both γ-$FeSi_2$ and β-$FeSi_2$ precipitated under Si^+ bombardment; without the Si^+ beam only β-$FeSi_2$ resulted.

2.10 Conditions of Formation/Transformation of the Pseudomorphic Silicides

The recently discovered γ-$FeSi_2$ and $FeSi_{(CsCl)}$ phases both occur pseudomorphically on Si substrates. Only when the ratio of interfacial area (with Si) to silicide volume is very large can these phases exist. The γ-$FeSi_2$/Si and $FeSi_{(CsCl)}$/Si interfaces are energetically favorable over the β-$FeSi_2$/Si and ε-FeSi/Si interfaces, but the γ-$FeSi_2$ and $FeSi_{(CsCl)}$ crystal structures themselves are higher energy configurations than their more common counterparts. The greater the interfacial area and the smaller the silicide volume, the more stable (or less unstable) these newly discovered structures become. This explains why researchers have reported that the temperature required to induce the transformation γ-$FeSi_2$ ⇒ β-$FeSi_2$ increases as the $FeSi_2$ film thickness is decreased.

There is more literature on the γ-$FeSi_2$ than on $FeSi_{(CsCl)}$, probably because many people hope that γ-$FeSi_2$ may be the key to better epitaxial β-$FeSi_2$. Onda *et al.*, in the original publication on γ-$FeSi_2$, reported the initial formation of this phase at 250°C in an MBE system on Si(111) surfaces [25]. The films could be made thicker at room temperature after an initial film of γ-$FeSi_2$ had crystallized. They found that the irreversible

transformation to β-$FeSi_2$ occurred at 200°C for γ-$FeSi_2$ films of 30 nm thickness and at 500°C for thinner films of only 1.4 nm. This research group has performed the most work on this phase and further details of their work are contained in references [25,30,56-59].

Kafader *et al.* have also investigated the thermal stability of γ-$FeSi_2$ thin films [28]. They deposited Fe films between 3 and 10 monolayers (ML) in thickness on Si(111) and annealed the films to form γ-$FeSi_2$. The thickest of these films, those which formed from 10 ML of Fe, were approximately 2.9 nm thick and were found to transform to β-$FeSi_2$ at 550°C. The γ-$FeSi_2$ films of less than 2 nm thickness were even more stable and did not transform prior to islanding at ~600°C.

The Si(111) surface is usually used for the formation of γ-$FeSi_2$ but it has been shown that the Si(100) surface also stabilizes the silicide at sufficiently low temperatures and thicknesses [11].

Particles of γ-$FeSi_2$ can also be stabilized by the Si matrix below the surface of the substrate. Lin *et al.* have been using ion implantation techniques to make small precipitates of γ-$FeSi_2$ in Si [31,50]. Silicon implanted with iron and then annealed at 320°C produced $FeSi_2$ precipitates -- all of them the γ form. On the other hand, implanted wafers annealed at 520°C produced β-$FeSi_2$ precipitates. If implanted wafers were bombarded with Si^+ ions during 520°C annealing, both γ and β-$FeSi_2$ particles resulted. The group concluded that the difference in product results because without Si^+ implantation the $FeSi_2$ formation is entirely thermally activated, while with bombardment the silicide formation is activated by the defects generated as well as the temperature. As would be expected, it was found that the smallest particles of γ-$FeSi_2$ were the most resistant to the transformation to β-$FeSi_2$. Many of the smallest particles remained untransformed after a 30 minute anneal at 900°C, a very high temperature for this phase.

The $FeSi_{(CsCl)}$ phase was originally reported in 1992 by von Känel *et al.* [22]. A slightly later paper by the same group on the same topic is [60]. Molecular beam epitaxy was used to grow thin films of the silicide on Si(111) at <100°C. The most interesting result of the research was the discovery that the $FeSi_{(CsCl)}$ films responded to annealing in various ways, depending on the thickness of the silicide. Films less than 1.5 nm thick increased in Si content without loss of epitaxy until they had transformed to γ-$FeSi_2$. Further annealing transformed the γ-$FeSi_2$ to β-$FeSi_2$. Films thicker than 1.5 nm transformed instead to ε-FeSi. In addition, the ε-FeSi was epitaxial if the film thickness had been less than 2.5 nm, and only randomly oriented if the film thickness had been greater than 2.5 nm.

2.11 Epitaxial Relationships of Iron Silicides

A silicide which is formed epitaxially on silicon has a definite consistent orientation relationship with the substrate and this gives rise to some favorable characteristics which make epitaxial silicides more attractive for electronic applications than "polycrystalline" (randomly oriented) silicides. Epitaxial silicides generally have greater thermal stability, smoother interfaces, more consistent electrical and mechanical properties, and fewer of the problems associated with grain boundaries. Therefore, the conditions necessary to obtain epitaxy, especially for β-$FeSi_2$, are the focus of many experiments.

To date, many researchers have obtained iron silicide films in which all the crystals were epitaxially aligned with the substrates. But there are two difficult obstacles still to be overcome. First, the average grain size of these epitaxial films is still quite small. Only a few very recent studies, such as [59], have produced epitaxial β-$FeSi_2$ grains larger than a few micrometres in width. Ideally, one would want continuous single crystal films across the entire interface. Related to increasing the grain size is the second challenge, to prevent the formation of rotational domains within epitaxial layers. This is particularly important with respect to epitaxial β-$FeSi_2$, which is orthorhombic. Rotational domains in epitaxial silicide layers are a result of the higher symmetry of the Si surface than that of the contacting plane of the silicide. To illustrate, the Si(100) surface is cubic while β-$FeSi_2$ has no cubic planes. It can be easily seen that there are 2 equivalent orientations when matching a rectangular surface to a square surface. Each orientation of the silicide is energetically equal and therefore just as probable as the other. On the Si(111) surface, which shows hexagonal symmetry, epitaxial β-$FeSi_2$ forms as 3 rotational domains. The rotational domains are dispersed among each other but, as shown in a very interesting micrograph in [59], generally each domain covers a significantly sized area. Some method must be devised to favour one azimuthal orientation over the others, so that they are not all energetically equal.

The epitaxial relationships which have been observed for β-$FeSi_2$ on Si are tabulated with literature sources in Table 2-2. Equivalent rotational domains are grouped together because they represent a single epitaxial relationship.

Table 2-2: Epitaxial Relationships for β-$FeSi_2$ on Si

Epitaxial Relationship	References
β(100) ‖ Si(100) and β[010] ‖ Si[011] β(100) ‖ Si(100) and β[010] ‖ Si[0$\bar{1}$1]	[11,35,59,61,62]
β(100) ‖ Si(100) and β[010] ‖ Si[010] β(100) ‖ Si(100) and β[010] ‖ Si[001]	[61,62]
β(001) ‖ Si(100) and β[010] ‖ Si[011] β(001) ‖ Si(100) and β[010] ‖ Si[0$\bar{1}$1]	[11]
β(001) ‖ Si(111) and β[010] ‖ Si[0$\bar{1}$1] β(001) ‖ Si(111) and β[010] ‖ Si[$\bar{1}$01] β(001) ‖ Si(111) and β[010] ‖ Si[$\bar{1}$10]	[63]
β(001) ‖ Si(111) and β[100] ‖ Si[11$\bar{2}$] β(001) ‖ Si(111) and β[100] ‖ Si[1$\bar{2}$1] β(001) ‖ Si(111) and β[100] ‖ Si[$\bar{2}$11]	[56]
β(101) ‖ Si(111) and β[010] ‖ Si[0$\bar{1}$1] β(101) ‖ Si(111) and β[010] ‖ Si[$\bar{1}$01] β(101) ‖ Si(111) and β[010] ‖ Si[$\bar{1}$10]	[13,43,56]
β(100) ‖ Si(111) and β[001] ‖ Si[0$\bar{1}$1] β(100) ‖ Si(111) and β[001] ‖ Si[$\bar{1}$01] β(100) ‖ Si(111) and β[001] ‖ Si[$\bar{1}$10]	[56]
β(100) ‖ Si(111) and β[010] ‖ Si[0$\bar{1}$1] β(100) ‖ Si(111) and β[010] ‖ Si[$\bar{1}$01] β(100) ‖ Si(111) and β[010] ‖ Si[$\bar{1}$10]	[56]

Table 2-2 (continued)

$\beta(110) \parallel Si(111)$ and $\beta[001] \parallel Si[0\bar{1}1]$ $\beta(110) \parallel Si(111)$ and $\beta[001] \parallel Si[\bar{1}01]$ $\beta(110) \parallel Si(111)$ and $\beta[001] \parallel Si[\bar{1}10]$	[43]

In the last several years, it has been noted that FeSi too can be grown epitaxially on single crystal silicon. The only epitaxial relationship reported thusfar is

$$FeSi(111) \parallel Si(111) \quad \text{and} \quad FeSi[1\bar{1}0] \parallel Si[2\bar{1}\bar{1}].$$

This epitaxy has been noted to occur by several different groups [10,26,60,63,64], none of whom claim to have produced epitaxy in FeSi films more than 10 nm thick. Again, this epitaxy is expected to exhibit 3 equivalent rotational domains.

2.12 The Islanding Problem

There have been many reports of the islanding or agglomeration of iron or iron silicide layers, especially β-$FeSi_2$ layers, during annealing [4,5,28,35,36,38,43,65-68]. Islanding has been reported for γ-$FeSi_2$ [28] as well as for β-$FeSi_2$ and α-Fe. The driving force behind this islanding process is the minimization of interfacial and surface energies. At a critical temperature, the surface silicide layer breaks into separate islands, exposing large clean areas of the silicon substrate. The reported values for this critical temperature of agglomeration onset range from 600°C to 740°C. Probably the temperature of islanding is a function of many variables, including the thickness of the silicide layer and the concentrations of contaminants such as oxygen at interfaces and surfaces. Impurities at interfaces and surfaces could alter the associated surface energies. Another important factor in islanding could be the crystallographic orientations of the silicides and substrate. Among the recent theoretical papers on islanding in thin films are [69-71].

Many experimental studies do not encounter the problem of agglomeration because they aim to produce β-$FeSi_2$ in UHV at a temperature too low to induce the problem [4,35,36,41-43]. But other experimenters, using conventional vacuum annealing, have made use of capping layers to avoid the islanding behavior [17,20,21,67,72]. After depositing the iron on the Si substrate, SiO_2, α-Si, or both are deposited on top. A

capping layer is typically several tens of nanometers thick and is intended to stop oxygen in the annealing atmosphere from reacting with or interdiffusing in the iron layer. A drawback to this capping technique is that, during annealing, an iron layer will react with a capping layer of α-Si, as well as with the crystalline Si substrate. This can severely complicate the interpretation of experimental results intended to elucidate the kinetics of iron silicide formation. The reaction kinetics of Fe reacting with α-Si are significantly different than the kinetics of Fe reacting with crystalline Si, as shown by Erlesand *et al.* [46]. It is suspected that Fe reacts more quickly with α-Si than with crystalline Si [73].

2.13 Impurities and Oxide Layers

Impurities present in a thin film diffusion couple of Fe/Si can interfere with the bonding and/or diffusion of Fe and Si atoms, altering silicide reaction kinetics. Any atoms other than Fe and Si are considered here to be impurities. There are four sources from which impurities may originate:

(1) Dopant elements are added to single crystal Si wafers to make them extrinsically semiconducting.

(2) The Si substrate can have surface contamination in the form of SiO_2, moisture, adsorbed gas molecules, fluorine ions (from the HF cleaning), or hydrocarbons such as the oils used in some vacuum systems.

(3) The iron used for the deposition will invariably contain some amount of impurities.

(4) Atoms from the annealing environment can diffuse into the diffusion couple.

Dopant atoms are added to essentially all single crystal Si grown because without their presence the Si cannot be used for fabrication of integrated circuitry devices. Therefore this source of impurities is not usually avoidable. Surface contamination of the Si substrate is minimized by cleaning procedures designed to remove the SiO_2 just before delivery of the substrate into the vacuum environment for iron deposition. It is not possible to remove all the oxide or contaminants from the Si surface using only *ex situ* cleaning methods alone, and hence the development of the *in situ* methods previously discussed. The purity of the iron available is of course limited by technological, if not economic, constraints. The extent to which a sample is contaminated by the fourth type of impurities, those from the annealing environment, is a function of the atmosphere and the pressure used in annealing. The best experimental results, in terms of result reproducibility, lowest reaction temperatures, best epitaxy, and the avoidance of islanding have been obtained with

UHV annealing. The higher the vacuum (ie. the lower the pressure), the better. If a purified gas, like N_2 or Ar, must be used as an annealing atmosphere, the concentration of O_2 in the gas is critical because iron oxidizes rapidly and oxygen is believed to be the contaminant element that most significantly affects metal/Si thin film kinetics [74].

It has been observed that impurities are capable of not only slowing reaction kinetics, by hindering reactant interdiffusion, but of actually producing a deviation from the usual phase formation sequence. An example, from Ottaviani [74], is the effect of oxygen on the Ni/Si reaction sequence, represented schematically in Figure 2-2. If vacuum annealed, the Ni and Si react to make an intermediate layer of Ni_2Si that grows until all the metal is consumed. A second silicide, NiSi, then forms at the Ni_2Si/Si interface. In contrast, if Ni/Si couples are annealed in flowing N_2 of 99.5% purity, NiSi begins to grow before the Ni_2Si has depleted the Ni source. Ottaviani conjectures that the impurities from the flowing gas, notably oxygen, diffuse through the Ni layer to the Ni/Ni_2Si interface and lower the diffusion flux of Ni atoms, allowing the NiSi to begin growing.

Another point to note about impurities is that they are thought to become segregated at interfaces as silicide growth proceeds [74]. Dopants in the silicon can become increasingly higher in concentration near the Si/silicide interface, just as dissolved oxygen becomes higher in concentration in the metal near the silicide/metal interface. Arsenic, phosphorus and antimony, commonly used as dopants in Si, are thought to concentrate at the silicide/Si interface in this way, especially during relatively low temperature anneals [75].

Swart and Berning [76] examined the effects of oxygen contamination on iron silicide formation by depositing iron films in oxygen pressures of $2\text{-}5 \times 10^{-6}$ torr. The resulting oxygen atomic concentrations in the Fe films were 2, 3, 10, and 35%. For the 2% oxygen samples, Fe was found to be the primary diffusing species during the formation of FeSi. Normally, without this contamination, Si is the primary diffuser during FeSi formation [40]. During the formation of FeSi, a layer of SiO_x formed at the Fe/FeSi interface. Presumably this layer grew thicker as the oxygen was transported to and concentrated at the interface. Further annealing of the 2% oxygen material produced β-$FeSi_2$ with the primary diffusing species switching to Si. In the samples containing higher concentrations of oxygen, silicide formation was prevented by the formation of iron oxides throughout the Fe films.

Chemelli *et al.* also investigated the effect of oxygen on iron silicide formation [77]. Instead of incorporating oxygen into the film, they allowed native oxide to form on cleaned Si(111) wafers and deposited pure iron films on these substrates. They estimated the SiO_2

layer to be ~0.5 nm thick. Annealing as high as 450°C did not promote any silicide formation but, at temperatures above this, the barrier was incapable of preventing metal diffusion and silicidation. However it was the iron, and not the silicon, that diffused through the oxide at these higher temperatures.

It is apparent too, that impurities such as oxygen discourage epitaxy. It seems clear that the recent improvement in attainable epitaxy corresponds directly to a continuous improvement in cleaning procedures and vacuum systems, both for film deposition and, more importantly, for annealing. Early attempts to obtain epitaxial β-$FeSi_2$ on Si(100) failed, while later experiments, using similar procedures but with vastly improved cleanliness, were successful. Samples are now usually cleaned *in situ* as well as *ex situ*. Instead of performing depositions in a "conventional" ~10^{-7} torr vacuum, many depositions are done in UHV (~10^{-10} torr) and many deposition systems are now equipped to anneal and even characterize the films *in situ*, making protective capping layers unnecessary.

2.14 Growth Kinetics -- Bulk Versus Thin Film Diffusion Couples

In a bulk diffusion couple composed of two different pure elements, it is usual that all of the binary compounds that are stable at the annealing temperature are observed simultaneously in the couple after sufficient annealing time. The annealing time must be "sufficient" in order to form compound layers thick enough to be detectable and separable from the relatively rough and dirty interfaces that exist in bulk couples. The compound layers are arranged between the pieces of elements A and B so that the atomic concentration of A falls steadily with increasing distance from the layer of element A.

In contrast, it is now accepted that thin film diffusion couples, such as those in SPE experiments, do not display all of the stable binary compounds simultaneously, or even at all. Often only one compound (other than the solid solutions of the starting elements) exists at any one time. The simultaneous growth of many different phase layers, as commonly seen in bulk diffusion couples, does not occur.

At present, there is no complete explanation for the difference observed between these two situations -- bulk diffusion couples and thin film diffusion couples. But there are two obvious differences between the two cases that are surely factors in the explanation. First the amounts of available reactants differ. In bulk couples, both reactant layers are much thicker than the distance that either element diffuses into the other. The extent of each reactant is equivalent to infinite when considering the diffusion gradients within the couple. However, in thin film diffusion couples, only one reactant (the substrate) can be considered

to be infinitely thick. The other reactant (the deposited film) is finite in thickness. Not only do diffusion gradients in the film intersect the outer boundary of the layer, but the supply of this element is completely exhausted after some period of annealing.

The second difference between the two types of diffusion couples is in the way the experiments are conducted. Bulk diffusion couples are annealed for much longer times because the interfaces of bulk couples are rougher and less clean and the characterization techniques typically used are not as sensitive as the equipment used for thin film diffusion couples. What happens in the initial annealing stage of a bulk diffusion couple is not known. The binary phases may all grow simultaneously, as they do later when they are much thicker, or only certain layers may be present in this early growth, just as only some phases are found in the thin film experiments. Thin film diffusion couples are monitored by equipment with great resolution that probes the very earliest stages of interdiffusion and compound growth.

Various research groups have contributed ideas and theories to help explain why simultaneous growth of all stable compounds is not observed in thin film diffusion couples and what it is that determines the sequence of phase formation in these couples [78-94]. Several of the largest contributors to this area now agree that the magnitudes and ratio of the diffusion fluxes arriving at any reaction interface comprise one of the most significant factors in determining the phase which forms at that interface [78-86,91]. Different fluxes will cause different phases to be preferred for formation. Two separate research groups have proposed the nature of this preferredness of formation. They have theorized that, given an interface with certain fluxes arriving for reaction, the phase formation which is preferred (and therefore will occur) is the reaction which can maximize the rate at which the system decreases its free energy [83,88]. To clarify this, they believe that the phase which forms in a given situation is the one which can result in the most negative value of $\partial G/\partial t$, where G is the Gibbs free energy of the system and t is time.

layer-by-layer

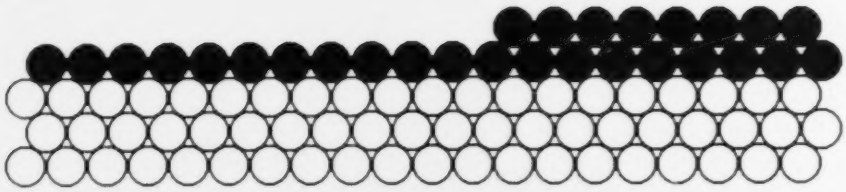

3D islands

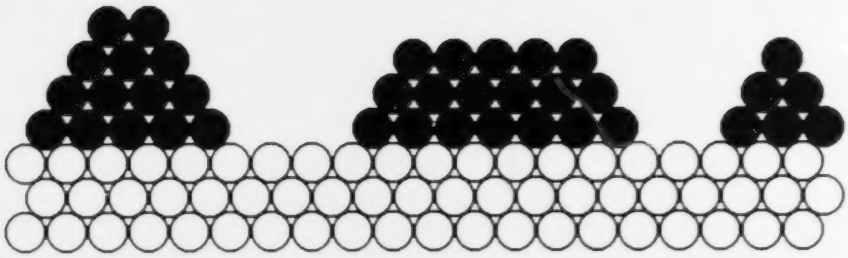

interface + 3D islands

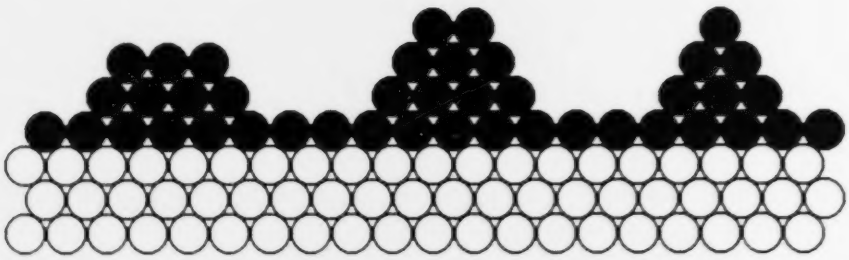

Figure 2-1. Three epitaxial growth modes [19].

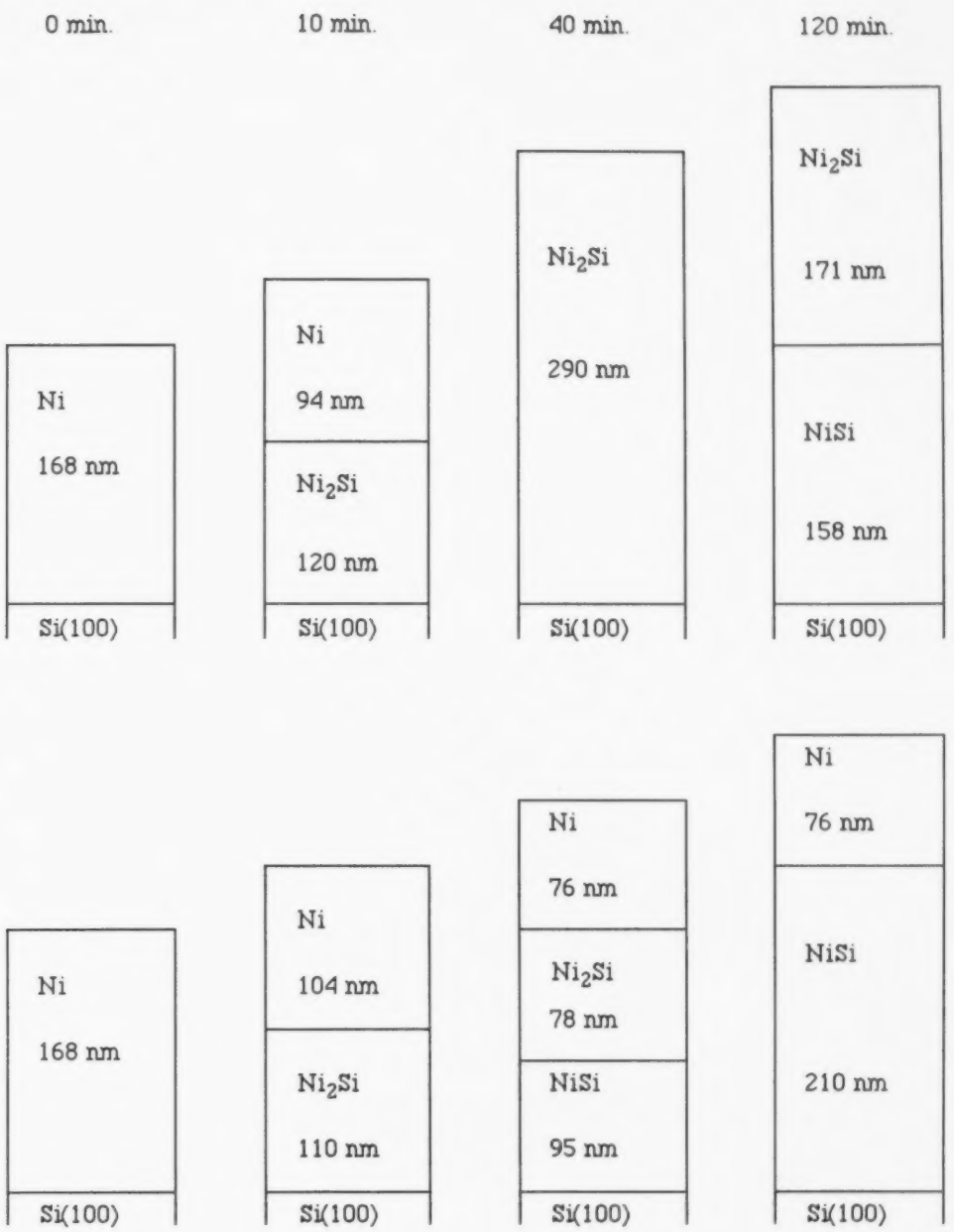

Figure 2-2. Example of the effect of oxygen on silicide kinetics [74]. Thin films of Ni on Si were annealed at 350°C. The formation sequence shown at the top of the page resulted from vacuum furnace annealing. The bottom sequence resulted from annealing in commercially pure flowing N_2.

Chapter 3 Thin Film Diffusion Couples

3.1 Experimental Methods

3.1.1 Deposition of Iron

The substrates used were two 3 inch Si(111) oriented wafers doped with boron to a resistivity of 1.0 - 10.0 Ω·cm. The wafers were cleaned in a 10:1 buffered hydrofluoric acid solution for about 1 minute. They were then thoroughly rinsed in deionized running water and blown dry with dry N_2. Immediately after cleaning, the substrates were loaded into the electron beam evaporation chamber and the chamber was evacuated.

Iron films were deposited onto Si(111) wafers by electron beam evaporation from a 99.95% pure Fe target, which had been recently degassed. In the same vacuum chamber, a protective capping film of SiO_2 was immediately evaporated on top of the Fe. The capping layer has been found to be necessary to prevent oxidation and agglomeration of the Fe film during *ex situ* annealing [67]. Base pressures were ~$4x10^{-8}$ torr and deposition pressures were ~$3x10^{-6}$ torr for the Fe and ~$5x10^{-7}$ torr for the SiO_2. The Fe was deposited at a rate of ~1.7 nm/s and the SiO_2 at a rate of ~0.2 nm/s. Film thicknesses were monitored during deposition by a quartz thickness monitor, but were more accurately determined later by cross-sectional transmission electron microscopy (TEM). The Fe layer was found to be ~40 nm thick; the SiO_2 was ~120 nm thick.

In order to facilitate TEM cross-sectional sample construction, one wafer was cut into pieces, each piece measuring 4.5 mm by 1.5 mm, with a computer-controlled diamond saw. Plan view TEM samples require round pieces of the specimen, rather than rectangular pieces. So the second as-deposited wafer was left unsawn and an ultrasonic disc cutter was used to cut discs from this wafer.

3.1.2 Annealing

Silicidation was achieved during anneals within a small quartz furnace. The furnace temperature was monitored and controlled by an electronic controller. Ramp up and ramp down times from the preset temperature were not included in the annealing time. Ramp up times were quite short because of the small heat capacity of the furnace and sample. Typically, the furnace required 45 to 90 seconds to reach the preset temperature from room temperature. The furnace was always at room temperature when the samples were loaded.

Ramp down times were longer, but only about 3 minutes were needed for the temperature to fall below 250°C, a temperature at which the silicide reactions occur many times slower than at the preset annealing temperatures.

During each anneal, only enough material was placed in the furnace to make one TEM sample. Cross-sectional samples required two of the previously sawn rectangular pieces measuring 4.5 mm by 1.5 mm. Plan view samples needed a single disc of 3 mm diameter. The amount of material annealed during one cycle was minimized so that ramp times would be as short as possible and so that as-deposited material would not be wasted. Careful conservation of the as-deposited material ensured that all of this research was carried out on the same two wafers which were covered with the Fe and SiO_2 films under identical conditions and at the same time. In this way, some potential variables in the TEM sample material are eliminated.

One variable in the films that could not be eliminated was the small spatial variation in film thickness that can be expected to exist because of the geometry of the deposition conditions. A virtual point source of evaporated material will not evenly cover a flat substrate if the width of the substrate is significant in comparison to the distance between it and the source. In order to check for spatial variation in initial Fe film thickness and be able to eliminate its effect on the silicide growth results, the original location of every piece of wafer material was recorded. The wafer was divided into rectangular sections as illustrated in Figure 3-1, each section having enough pieces to construct nine cross-sectional samples. The center two pieces were used to make the as-deposited sample that would determine the as-deposited thickness for that section. The surrounding pieces were made into samples, always chosen by adjacent pair to minimize possible variations, and the silicide thicknesses observed in these samples were compared to the as-deposited value for that section.

The substrate pieces necessary for the sample were placed in the furnace stage with the film side up to avoid contamination from the stage surface. A piece of unused Si wafer was placed flat on top of the pieces to be annealed. This cover piece was about 1 cm square and its polished side faced the film surface of the sample material. The sample material and the cover piece were cleaned in both acetone and ethanol and dried before loading into the furnace.

The cover piece was necessary to prevent condensation of contaminant elements on the SiO_2 film surface during the cooling after annealing. The major contaminant was indium, thought to be present in the furnace because of annealing done previously on InP wafers. Indium has a low melting point and high vapor pressure and some small amount

of the element remained on the inner surfaces of the furnace. Large crystals of indium compounds were observed by scanning electron microscopy to have grown on unprotected surfaces during annealing cycles in this furnace. It is known that indium did not contaminate the thin film diffusion couples of this work however, because energy dispersive spectrometry (EDS) analysis on numerous TEM samples indicated the presence of only iron, silicon and oxygen.

After placing the cleaned sample material and covering piece in the furnace and closing the chamber, the furnace was purged for several minutes with pure nitrogen gas. The flow rate was then lowered for the anneal and the electronic controller engaged. Annealing times (excluding the ramp up and ramp down times) ranged from 7 minutes to 3 hours. Annealing temperatures used were 300°C, 400°C, 500°C, 600°C and 650°C. After annealing the furnace was not opened until it had cooled to below 100°C. This prevented any oxidation of the iron phases.

3.1.3 TEM Sample Preparation

Two types of TEM samples were constructed -- cross-sectional and plan view. To make a cross-sectional sample, the two rectangular pieces of annealed wafer material are glued together with silver epoxy so that the film surfaces face each other as shown in Figure 3-2. Other pieces of plain silicon with the same dimensions are glued on either side as in the diagram. The 10 pieces of silicon are held together tightly in a small screw-tightened press, which is put into a furnace and heated at 85°C for 80-90 minutes to harden the epoxy.

After hardening the epoxy, the press is removed from the furnace and the silicon-epoxy composite released. The sample is then ground plane from both sides by mounting it on a small steel stage, which sits in the center of a flat steel grinding jig. The stage is about 1 cm in diameter and is heated on a hot plate to about 120°C. A small amount of low-melting-point glue is placed on the stage and the sample placed in the melted glue. Upon cooling, the glue hardens and the sample is attached to the stage and can be ground with the jig. The sample can be removed from the steel stage by melting the glue and the glue is cleaned from the sample with acetone.

Once the cross-sectional sample has been ground so that its two sides are plane and parallel and the sample thickness is approximately 400 μm, a 3 mm diameter disc is cut from the material. The sample is glued to a flat piece of expendable aluminum and an

ultrasonic disc cutter is used to cut the disc, which is centered on the interface containing the silicide films.

At this point, the cross-sectional sample is of the same dimensions as the plan view sample as it exists after annealing -- a 3 mm diameter disc of about 400 μm thickness. The remaining steps of the sample-making procedure are the same for both types of samples.

The steel stage and jig are again used to decrease the sample thickness to between 100 and 150 μm. At this thickness, the sample is ready for dimpling. A Gatan Model 656 Dimpler is used to mechanically polish a round dimple into one side of the sample. If the sample is of the plan view type, it is imperative that the dimpled side be the side without the films of interest. If the sample is cross-sectional it does not matter which side is dimpled. The dimpler consists of a small rotating bronze wheel which is lowered onto the sample as the sample revolves on a stage. Small amounts of water and diamond paste (with 3 or 6 μm diamond particles) are fed onto the wheel as it polishes the dimple into the sample. Micrometers allow reasonably accurate control of the position and depth of the dimple.

For dimpling, the sample is placed on a transparent stage so that a light can be shone on the lower surface of the sample. Silicon becomes noticeably transparent to red light at thicknesses below about 10 μm and this can be used, especially with cross-sectional samples, to determine the thickness at the center of the dimple. Once the thickness at the sample center is thought to be less than 10 μm, the dimple is deep enough and is ready to be polished smooth. The bronze dimpler wheel is exchanged for a cloth covered one and the abrasive chosen is no coarser than 3 μm. It is important that the dimple surface be very smooth because ion milling, the next and final stage in sample preparation, tends to amplify any surface roughness through shadowing effects.

An ion milling machine is simply a sputtering chamber. Usually when sputtering, one is concerned with the surface that receives the sputtered flux. But when ion milling, the concern is the sputtering target. The TEM samples are the target of the Ar^+ flux and are gradually worn thinner. Damaged layers of mechanically deformed material are removed one atomic layer at a time to leave a very thin area in the center of the TEM sample which is as similar as possible to the original, undisturbed material of interest. Cross-sectional samples are ion milled from both sides simultaneously. Plan view samples were first ion milled for about 6 minutes on the film side to remove the SiO_2 and then milled on the Si substrate side. All samples are milled until a small hole in the center of the sample is detected by a laser-detector system in the ion mill. Cross-sectional samples are cooled by a liquid nitrogen stage during ion milling to minimize differential ion milling rates of the

various phases exposed to the ion flux. The ion mill used was a Gatan Model 600 Dual Ion Mill.

3.1.4 Characterization

The TEM cross-sectional and plan view samples were examined in three microscopes -- a Hitachi H-7000, a Philips EM400T and a JEOL 2010. The actual magnification produced by each microscope at each nominal magnification setting was checked using standards. Selected area diffraction data was calibrated by computing camera constants from the internal Si standards. The JEOL microscope, which is fitted with EDS equipment (a Ge ultrathin window x-ray detector), was used to check the composition of silicide grains in cross-sectional samples. In particular, the various phases were checked for unintentional oxidation, contamination, and Fe:Si atomic ratios. Actual atomic concentration (C) ratios of Fe:Si were calculated by determining a Cliff-Lorimer factor (k) from pure FeSi and β-$FeSi_2$ standards and multiplying this factor by the intensity (I) ratios of the two elements.

$$\frac{C_{Fe}}{C_{Si}} = k \cdot \frac{I_{Fe}}{I_{Si}} \qquad \text{where } k \approx 0.6 \text{ (in this work)} \qquad (1)$$

3.2 Results and Discussion

3.2.1 Conditions and Sequence of Silicide Formation

One of the as-deposited cross-sectional samples is shown in Figure 3-3. The as-deposited Fe layer in plan view is also pictured. The as-deposited thickness was found to vary negligibly across the wafer area used in this work. The Fe layer thickness is calculated from micrographs to be about 40 nm. This initial Fe layer contains many voids though, because of the low temperature and rapid rate at which it was deposited. Measuring the thickness of completed β-$FeSi_2$ layers and knowing the unit cell volume of the disilicide and Fe, the as-deposited layer is found to be equivalent in Fe content to a fully dense layer of about 35 nm. Table 3-1 lists the relative layer thicknesses of each phase that contain the same number of atoms of Fe. These numbers were used to calculate Fe mass balances to check phase identifications.

Table 3-1: Relative Layer Thicknesses for Equivalent Iron Content

Fe	Fe_3Si	FeSi	β-$FeSi_2$
1	1.26	1.91	3.18

The Fe-Si phases that were observed in the thin film diffusion couples are α-Fe with dissolved Si, Fe_3Si, FeSi and β-$FeSi_2$. The annealing conditions which were examined with TEM are listed below.

Table 3-2: Annealing Conditions Studied with Transmission Electron Microscopy

Temperature (°C)	Time (hour:min.)	Temperature (°C)	Time (hour:min.)	Temperature (°C)	Time (hour:min.)
300	1:00	500	0:30	600	2:00
300	2:00	500	1:00	600	2:30
300	3:00	500	1:30	650	0:07
400	0:30	500	1:45	650	0:10
400	0:50	500	2:00	650	0:15
400	1:00	600	0:15	650	0:30
400	2:00	600	0:30	650	1:00
500	0:15	600	1:00	650	2:00

As would be expected, the rate at which the silicides are formed increases as the annealing temperature is raised. However the sequence of silicide formation was not observed to be a function of annealing temperature. All observations made at all five temperatures support the same formation sequence:

(1) Si dissolves into the α-Fe layer.

(2) Fe_3Si begins forming a continuous layer between the α-Fe and Si.

(3) FeSi nucleates between Fe_3Si and Si while Fe_3Si continues to grow.

(4) Fe_3Si and FeSi both grow as diffusion controlled layers simultaneously.

(5) α-Fe is completely consumed and Fe_3Si begins to shrink.

(6) FeSi is the only silicide, having completely consumed Fe_3Si.

(7) Small nuclei of β-$FeSi_2$ form between FeSi and Si.

(8) A few of the β-$FeSi_2$ nuclei reach a critical size, whereupon they grow rapidly into large circular colonies, spreading laterally through the FeSi.

(9) The β-$FeSi_2$ colonies converge on one another, all of the FeSi is consumed and the reaction sequence is finished.

There is the possibility that at the highest temperatures, 600°C and above, the reaction steps prior to the formation of the FeSi layer were not the same as described here. No attempt was made to study the formation of the solid solution or Fe_3Si layers at the highest temperatures because, under these conditions of very rapid diffusion, these initial reactions are difficult to observe -- catching the desired silicide growth stage becomes a matter of seconds. As well, it was felt that with a 3 minute anneal at 600°C, for example, the time spent approaching and leaving the setpoint temperature would become more significant to the final microstructure than the 3 minutes spent at 600°C. For these reasons, most of the study of the early silicide reactions was done at 400°C. At 400°C, the entire sequence of nine steps described above was observed, except for the growth of the β-$FeSi_2$ colonies, which is kinetically hindered at this low temperature.

The growth kinetics that were observed will now be discussed in detail. Selected micrographs and diffraction patterns are included. (For reference, crystallographic spacings have been tabulated in Appendix B.) It should be explained that the EDS results, although quantified against standards, were useful only in making tentative phase identifications and finding sudden concentration changes which would indicate phase interfaces. The phase identifications could later be verified by checking diffraction patterns, calculating Fe mass balances, comparing grain sizes and microstructures, and checking for agreement with phase identifications for other annealing conditions. The EDS results were not, however, accurate enough to provide reliable grain-by-grain phase identification or precise compositional information. The "quantified" atomic concentrations obtained contain large errors, due in part to beam drift and poor counting statistics. In order to focus the TEM electron beam onto very thin layers, its intensity sometimes had to be reduced to a level at which x-rays were generated at very low rates and therefore the raw spectra contained few counts.

At 300°C the silicide reactions progress slowly and Fe_3Si was the only iron silicide formed within 3 hours of annealing. Micrographs of cross-sectional samples annealed at 300°C for 1, 2 and 3 hours are shown in Figure 3-4. The film remained very even in thickness throughout the annealing while grain sizes increased somewhat. No interface which would indicate the presence of more than a single thin film phase can be seen in any of the micrographs. This, combined with plan view micrographs of the film after 2 hours (Figure 3-4d) that look very much like plan views of the as-deposited Fe, would suggest that no silicides were formed within 3 hours. However, in Figure 3-5, a diffraction pattern

taken from the 2 hour plan view sample shows diffuse rings which correspond to the crystallographic spacings of (210) and (200) planes in α_1 Fe_3Si. Normally the (210) planes of this crystal structure would be expected to produce reflections of zero intensity -- systematic absences. However, grains of such small size (<10 nm) and likely poor crystallinity (high defect densities and large distributions in crystal spacings) could produce non-zero intensity reflections from planes which would not be represented in patterns generated from large well-annealed crystals. It seems unlikely that the entire film layer after 2 hours annealing is α_1 Fe_3Si because the diffraction rings representing the Fe_3Si are relatively weak. From work done on samples annealed at 400°C, it is known that Fe_3Si forms a continuous layer that is microstructurally separate from the α-Fe layer. So it is not expected that grains of the two phases are dispersed among each other in the 2 and 3 hour samples. But because no α-Fe/Fe_3Si interfaces could be found in the 300°C samples, the proportions of the phases in the films are unknown.

More study was focussed on the reactions at 400°C, a temperature which speeds the kinetics to more practical rates. The silicide thicknesses measured from 400°C samples are illustrated schematically in Figure 3-6. After 30 minutes of annealing there are two easily distinguished layers separated by a straight interface (Figure 3-7). The outer layer is 30 nm of α-Fe and the inner layer is 10 nm of Fe_3Si. Mass balance calculations agree with these measurements from micrographs. Numerous EDS spectra yielded an average Si content of 10% for the α-Fe layer and confirmed the inner layer to be approximately 25% Si. A diffraction pattern from a plan view of this annealing condition is shown in Figure 3-8. Rings corresponding to the (200) and (210) planes of α_1 Fe_3Si appear in the micrograph negative, although only the (210) ring is strong enough to be seen in Figure 3-8. The rest of the rings of the pattern are ambiguous and therefore not useful. They correspond to more than one of the possible phases. There are some spots in this diffraction pattern that are very useful though. These spots, also indexed in Figure 3-8, represent FeSi. No FeSi was identified in cross-sectional specimens annealed 30 minutes, but this pattern clearly shows spots from (110) and (211) FeSi planes. After half an hour of annealing, FeSi was forming and was highly preferentially oriented to the Si substrate. Preferential orientation is reasonable since the silicide would form next to the single crystal Si. The orientation of FeSi is examined in greater detail in a later section of this thesis.

It is significant that Fe_3Si and FeSi have been observed in this research to grow simultaneously at 400°C. It is usually assumed that iron silicides grow one at a time, each completely consuming the previous phase before a third begins to grow. But most investigations in the literature do not seem to have made systematic efforts to validate this

assumption. Study of samples annealed for 50 minutes, 1 hour and 2 hours show that the two iron silicides do grow together.

Figure 3-9 is a micrograph of a sample annealed for 1 hour at 400°C. The α-Fe layer was about 25 nm thick, slightly thinner than after the half hour anneal, and again contained about 10% Si. The Fe_3Si layer was still about 10 nm thick. Protrusions of FeSi can be seen between the Fe_3Si and the Si substrate. These FeSi growths became a continuous layer with longer annealing. From an iron mass balance calculation, the amount of FeSi present should be equivalent to a uniform layer of 9 nm. This seems to agree with what is seen in the micrographs. Moiré fringes are present in the FeSi grains of Figure 3-9. These fringes were found to be very characteristic of the phase and provided another aid in identification. The fringes are a result of the preferential orientation, with slight mismatch, of the FeSi crystals to the substrate and, therefore, to each other. EDS confirmed that the FeSi protrusions were much higher in Si content than the Fe_3Si layer above them.

After 2 hours at 400°C, the α-Fe layer was completely consumed. At this annealing condition, there were two layers (Figure 3-10). The Fe_3Si averaged 18 nm in thickness; the FeSi averaged 40 nm. Again, these thicknesses were found to be in agreement with a mass balance for iron. The boundary between the Fe_3Si and FeSi was much more irregular than the boundary seen in other samples between the α-Fe and the Fe_3Si. A diffraction pattern from a 400°C 2 hour plan view sample (Figure 3-11) contains strong reflections from both Fe_3Si and FeSi.

At 500°C, the early stages of the silicide growth sequence progress much faster. A sample, shown in Figure 3-12, annealed for only 15 minutes contained a completed layer of FeSi with no Fe_3Si remaining. The silicide layer was the thickness expected for FeSi by mass balance considerations and the Moiré fringes and grain size are identifying features of FeSi. It seems odd that, at 500°C, the progression to a complete layer of FeSi is so rapid, while the appearance of β-$FeSi_2$ colonies is so delayed. Samples after 30 minutes, 1 hour, 1.5 hours, 1.75 hours and 2 hours all looked much like the 15 minute sample -- an even layer of FeSi. No colonies of β-$FeSi_2$ could be found in plan views and diffraction analysis indicated no phase other than FeSi. The reason for this contrast in formation times -- very short for FeSi and long for β-$FeSi_2$ -- is explained by the different natures of their formation kinetics. Both Fe_3Si and FeSi grow as diffusion controlled layers whereas the formation of β-$FeSi_2$ is nucleation controlled. At 500°C, diffusion is quite rapid and the diffusion controlled layers grow quickly, but apparently at this temperature it is still quite improbable that a subcritical β-$FeSi_2$ nucleus will reach its critical size and form a growing

colony. It is interesting that, although no β-$FeSi_2$ colonies formed after 2 hours, subcritical nuclei were found after as little as 1 hour (Figure 3-13). These tiny β-$FeSi_2$ protrusions between the FeSi and Si were found by watching for grain-to-grain contrast while slowly tilting the TEM specimen stage. The β-$FeSi_2$ grains are smaller than almost all the FeSi grains and occur at the FeSi/Si interface with their longest dimension aligned along the interface, presumably to take advantage of the interfacial surface energy available. By comparison, the individual FeSi grains usually extend through the entire thickness of the film. EDS analysis confirmed that the protrusions, including that of Figure 3-13, were significantly higher in Si content than the main FeSi layer.

Annealing at 600°C, as at 500°C, produced completed FeSi layers within 15 minutes. Unlike the lower temperature anneals however, the 600°C samples produced the first growing β-$FeSi_2$ colonies after only about 1 hour of heating. Figure 3-14 shows one of these colonies in plan view. The β-$FeSi_2$ covers a circular area and is easily identified by its grain size, which is much larger than that of FeSi. There were only about a dozen colonies like the one pictured on the entire sample. The distances separating them were typically at least 10 times the width of the colonies.

Although it was previously thought that β-$FeSi_2$ grew by nucleation-controlled kinetics [8], these are believed to be the first micrographs taken of β-$FeSi_2$ colonies. These pictures give more direct and graphic evidence of the way that this silicide grows than previous experimental support has offered.

The β-$FeSi_2$ colonies which form at 600°C grow radially outward through the silicide film until they contact one another. After 2 hours, a small fraction of the film is still FeSi. Only a few tens of grains of FeSi were found in an entire plan view sample after 2.5 hours of annealing.

Small β-$FeSi_2$ colonies are found in plan view samples annealed for only 7 minutes at 650°C. It is really quite uncertain what the earlier silicide reactions are at this temperature, given such rapid kinetics. The β-$FeSi_2$ consumed virtually all of the FeSi after 1 hour of annealing at 650°C. No FeSi at all could be found in a sample that had been annealed for 2 hours.

Figures 3-15 and 3-16 are high magnification images of the FeSi and β-$FeSi_2$ grain structures formed in 650°C samples. Note the profusion of Moiré fringes seen in the FeSi grains, a result of slight mismatches between the crystallographic spacings/orientations of the overlapping FeSi and Si crystals. The β-$FeSi_2$ grains also have an interesting feature. A type of internal microstructure, possibly twins, streaks across most of the grains. This microstructural feature is discussed later in this thesis.

3.2.2 FeSi Preferred Orientation

As mentioned in Chapter 2, FeSi has been reported to grow epitaxially on Si(111) under some conditions [10,26,60,63,64]. The same epitaxial relationship has been found in all cases and it has only been observed in FeSi films thinner than 10 nm.

$$\text{FeSi}(111) \parallel \text{Si}(111) \quad \text{and} \quad \text{FeSi}[1\bar{1}0] \parallel \text{Si}[2\bar{1}\bar{1}]$$

This same preferred orientation was found in some films of this work. It is not known at this time whether what has been observed is complete epitaxy or instead a preferred orientation of the grains. Therefore the dominant relationship of the FeSi to the substrate is referred to as the preferred orientation.

Selected area diffraction patterns indicated the texture in the grains of some of the FeSi films and these diffraction patterns were used to determine the preferred orientation. Table 3-3 shows the samples which were found to contain preferentially oriented FeSi and those in which the FeSi seemed randomly, or at least less, oriented. Note that 75 nm was the thickness of a layer of FeSi that contained all the originally deposited Fe.

Table 3-3: Orientation of FeSi Film

Annealing Condition	Preferred or Random Orientation	FeSi Thickness
400°C 30 minutes	Preferred	very small pockets
400°C 2 hours	Preferred	40 nm
500°C 1.5 hours	Random	75 nm (complete)
600°C 1 hour	Random	75 nm (complete)
650°C 30 minutes	Random	75 nm (complete)

The difference between the two types of diffraction patterns -- preferentially oriented FeSi versus "randomly" oriented FeSi -- can be seen by comparing Figures 3-11 and 3-17. Figure 3-11 is a diffraction pattern from FeSi formed in a 400°C 2 hours sample, while Figure 3-17 is a pattern from the FeSi layer of a 650°C 30 minutes sample. The FeSi rings from the lower temperature condition show regularly occurring variations in intensity while the random intensity variations in the FeSi rings of Figure 3-17 result only because the pattern was taken from relatively few grains.

It is apparent that the strongly preferentially oriented FeSi correlates to lower annealing temperatures and thinner FeSi layers. It is not clear, though, whether all the FeSi films were oriented at sufficiently small thicknesses and the orientation of the thicker films was lost as they grew, or whether the preferential FeSi orientation occurs only at the low temperatures because of differences in kinetic factors. If indeed the FeSi is oriented only at the lower temperatures, perhaps it remains oriented for thicknesses well in excess of the 40 nm that was observed. Even 40 nm is much thicker than any FeSi film previously reported to show non-random orientation to Si(111).

3.2.3 Silicide Grain Sizes and Morphology

Grain sizes were calculated from micrographs of plan view areas. A mean grain size was found by placing a ruler randomly across the micrograph and counting the number of grains that it intersected. The distance along the ruler was divided by the number of grains and further divided by the micrograph magnification. For micrographs with large grains, the average was calculated from several random placements of the ruler rather than only one so that statistical accuracy would be improved. Because it was not possible to distinguish α-Fe from Fe_3Si in plan views, the Fe_3Si grain sizes are estimated from cross-sectional views. Accuracy for FeSi and β-$FeSi_2$ was much better than for the other phases, the grains of which are not as sharply defined. Table 3-4 gives the average grain sizes computed.

From Table 3-4 it is apparent that each silicide phase was larger in grain size than the phase previous to it. The Fe had a very small grain size in the as-deposited samples. Its grain size was seen in cross-sections to grow slightly during annealing. The Fe_3Si grains were similar in size to the grains of annealed α-Fe that they replaced. The FeSi began with approximately the same grain size as the Fe_3Si and grew steadily with annealing, eventually doubling its grain size at 650°C before being consumed. The FeSi grains grew faster at higher temperatures, as would be expected. All the phases except the β-$FeSi_2$ had grain sizes of the same order of magnitude. The β-$FeSi_2$ grain size was an order of magnitude larger.

Consulting the four entries in Table 3-4 for β-$FeSi_2$ grain sizes at 650°C, it is seen that the silicide had a grain size of 130 nm at 7 minutes, likely no more than 100 seconds after formation of the first β-$FeSi_2$. It seems reasonable that the average grain size of the phase then increased during the next several minutes to 220 nm -- larger grains were growing at the expense of smaller. What is surprising is that the mean grain size appears to

have then slowly decreased over a long period of time, after reaching some maximum size within minutes of the appearance of the phase.

Table 3-4: Mean Grain Sizes in Iron Silicide Films

Phase	Annealing Condition	Mean Grain Size (nm)
α-Fe	as-deposited	10
Fe_3Si	400°C 2 hours	20
FeSi	500°C 1.5 hours	24
FeSi	500°C 1.75 hours	25
FeSi	650°C 7 minutes	28
FeSi	650°C 10 minutes	30
FeSi	650°C 30 minutes	33
FeSi	650°C 1 hour	39
β-$FeSi_2$	600°C 2.5 hours	210
β-$FeSi_2$	650°C 7 minutes	130
β-$FeSi_2$	650°C 10 minutes	220
β-$FeSi_2$	650°C 30 minutes	200
β-$FeSi_2$	650°C 1 hour	180

As previously mentioned, the β-$FeSi_2$ grains often displayed internal features that may be twins (Figure 3-16). These features are believed to be the same planar defects which Zheng *et al.* recently detailed in a paper [95]. They concluded that their β-$FeSi_2$ films were composed of parallel "twinlike" structures running along the [100] directions of the β-$FeSi_2$. These lamellae were concluded to be 0.5 to 3 nm in thickness and highly strained.

The grains of β-$FeSi_2$ were also observed to be quite irregular in shape and the size distribution was probably wider than for any of the other phases. Bend contours could be found in almost any grain of β-$FeSi_2$ examined. In contrast, the grains of FeSi were all equiaxed in shape and the distribution of sizes was much narrower. Neither internal features nor bend contours were observed in any FeSi grains. Both of these silicides had very sharply defined grain boundaries.

3.2.4 Performance of SiO_2 Capping Layer

It has been noted by various researchers that Fe thin films will oxidize and show islanding behavior on Si substrates if the films are annealed unprotected in flowing gases rather than in a vacuum [17,20,21,67,72,73]. When Fe films must be annealed in flowing gases, such as N_2 or Ar, capping layers can be deposited on top of the Fe to protect it from the small amounts of oxygen that inevitably remain in the annealing gases. Previous research which compared the effectiveness of various capping layers (Si, SiO_2, and both of these) in protecting Fe thin films from oxidation led to the conclusion that SiO_2 alone is insufficient [67].

The Fe films of this study were protected by SiO_2 evaporated films of 120 nm thickness. If islanding was occurring, complete breaks in the Fe or silicide layers should have been present. However, no break was ever found in any layer in any sample examined. In cross-section, all layers were always continuous. In plan view TEM samples, which enable the examination of larger areas of silicides, no break of any size was ever found in the films. Neither EDS nor diffraction results ever pointed to the presence of iron oxides or any other unexpected phases.

3.3 Conclusions and Recommendations

During the course of this study of thin film iron silicides, the following conclusions have been reached:

(1) A Fe_3Si layer forms at 300°C and 400°C. The mean grain size is approximately 20 nm.

(2) Fe_3Si grows as a continuous, diffusion controlled layer that is microstructurally separate from the α-Fe.

(3) At 400°C, the Fe_3Si and FeSi layers grow simultaneously for some time.

(4) The average grain size of FeSi is on the order of 30 nm. The grain size of this silicide increases with annealing time and temperature.

(5) At some temperatures and film thicknesses, FeSi is strongly preferentially oriented with respect to Si(111) substrates so that FeSi[111] ∥ Si[111] and FeSi$(1\bar{2}1)$ ∥ Si$(1\bar{1}0)$.

(6) β-$FeSi_2$ nuclei of subcritical size are present long before β-$FeSi_2$ colonies begin to grow.

(7) The time required for some β-$FeSi_2$ nuclei of critical size to form is highly temperature dependent. At 650°C, it is no more than 400 seconds; at 600°C, it is about an hour.

(8) β-$FeSi_2$ forms on Si(111) as isolated circular colonies that expand laterally through the FeSi. This growth behavior occurs because the nucleation kinetics are rate-limiting.

(9) Average grain sizes (measured parallel to the film) for β-$FeSi_2$ are typically about 200 nm.

(10) A 120 nm layer of evaporated SiO_2 satisfactorily protects Fe thin film on Si substrates from oxidation during annealing in N_2.

There are many aspects of iron thin film formation that remain to be elucidated. Some suggestions for further study are given:

(1) FeSi is strongly preferentially oriented with respect to the Si(111) substrate at some silicide thicknesses and annealing temperatures. It remains to be seen whether this non-randomness of orientation can be used to orient the successive β-$FeSi_2$ layer, either by depositing a sufficiently thin Fe layer so that the FeSi remains oriented or by creating oriented FeSi at a low temperature and then stepping up the temperature to nucleate β-$FeSi_2$.

(2) Another possibility for exploiting the FeSi orientation to orient β-$FeSi_2$ is to provide some type of artificial nucleation sites for the β-$FeSi_2$. At 400°C FeSi was observed to be strongly preferentially oriented but the activation energy to form a β-$FeSi_2$ nucleus of viable size is unlikely to be provided. Artificial nucleation sites, possibly in the form of defect clusters or stable particles of other phases, could perhaps allow β-$FeSi_2$ growth at this temperature by providing some of the energy necessary to surmount the energy barrier.

(3) Extremely long anneals, on the order of weeks, at 650°C may grow larger β-$FeSi_2$ grains with lower defect densities. This could be easily investigated.

(4) There has been very little study committed to Fe_3Si and much more work could be done on this phase.

(5) The pseudomorphic phases, γ-$FeSi_2$ and $FeSi_{(CsCl)}$ look extremely promising. In themselves, they represent new phases in the Fe-Si system with properties different than the other silicides. These phases also may hold the key to achieving long range epitaxy of β-$FeSi_2$ grains, as growth templates or intermediate layers between the substrate and β-$FeSi_2$. There

may be tertiary elements that can stabilize these metastable phases to greater thicknesses and higher temperatures.

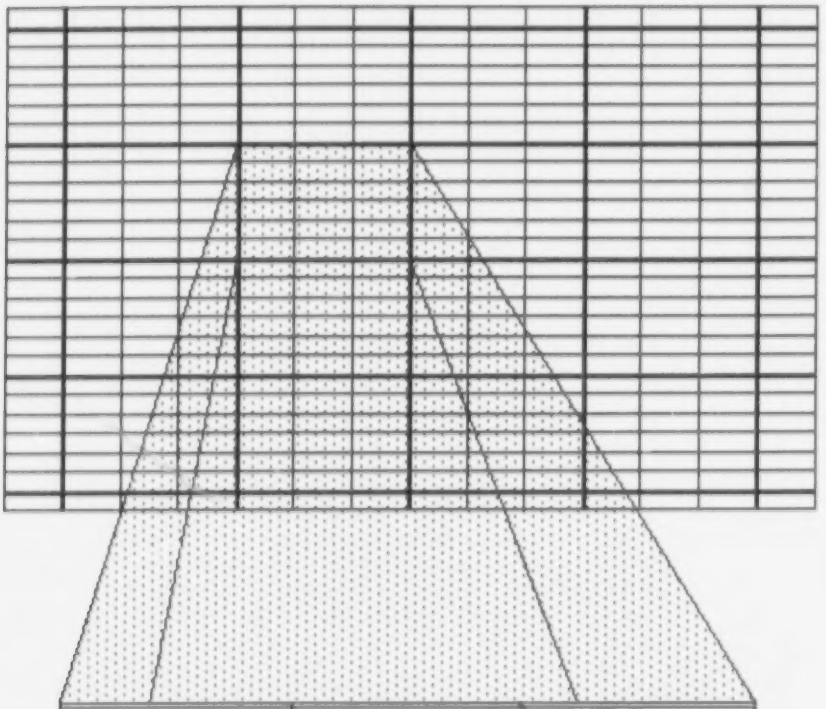

used for sample 1	used for sample 4	used for sample 6
used for sample 1	used for sample 4	used for sample 6
used for sample 2	used for as-deposited	used for sample 7
used for sample 2	used for as-deposited	used for sample 7
used for sample 3	used for sample 5	used for sample 8
used for sample 3	used for sample 5	used for sample 8

Figure 3-1. System for location of sample pieces in original wafers. The centre pieces of each block are used to make an as-deposited TEM sample to determine the initial Fe thickness in the surrounding pieces, which are used to construct eight other TEM samples.

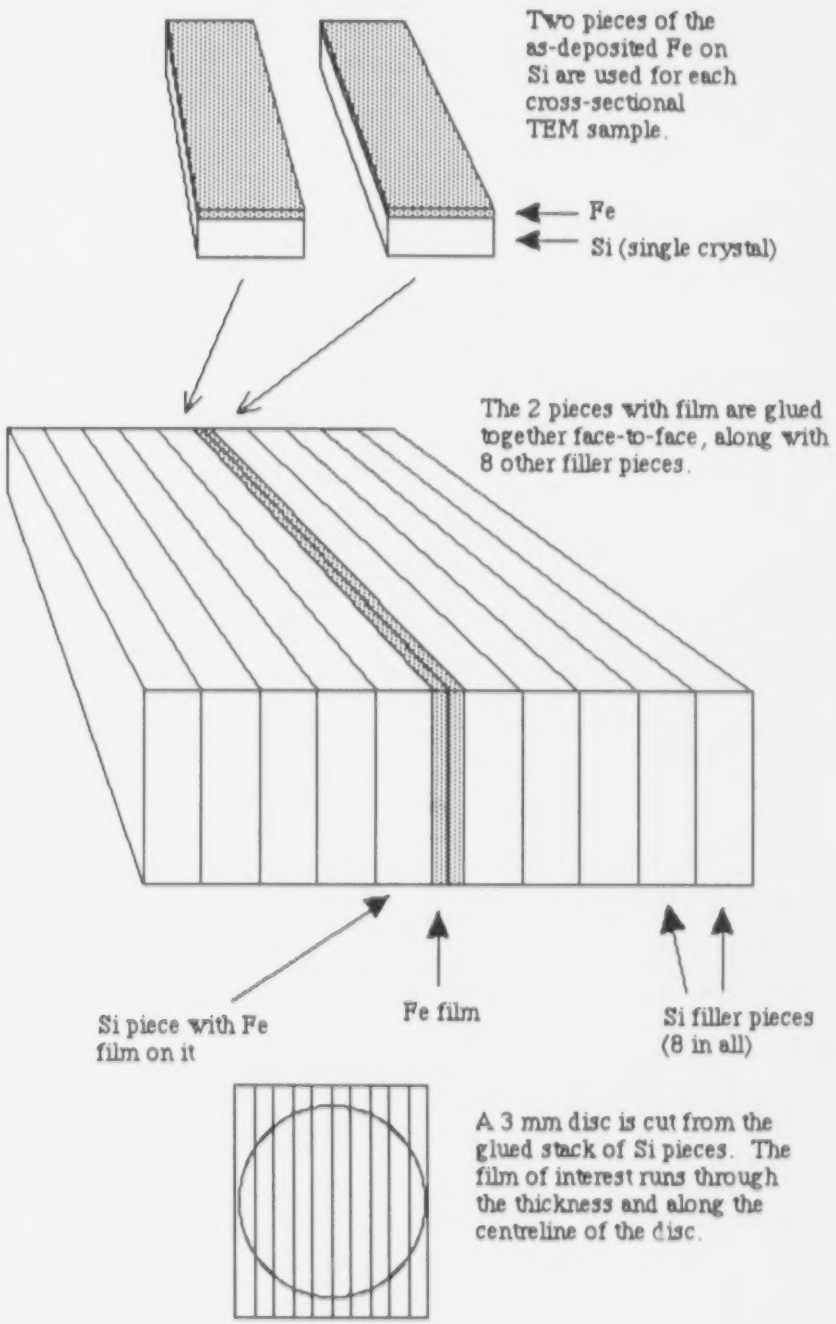
Two pieces of the as-deposited Fe on Si are used for each cross-sectional TEM sample.
Fe
Si (single crystal)
The 2 pieces with film are glued together face-to-face, along with 8 other filler pieces.
Si piece with Fe film on it
Fe film
Si filler pieces (8 in all)
A 3 mm disc is cut from the glued stack of Si pieces. The film of interest runs through the thickness and along the centreline of the disc.

Figure 3-2. Construction of cross-sectional transmission electron microscopy samples.

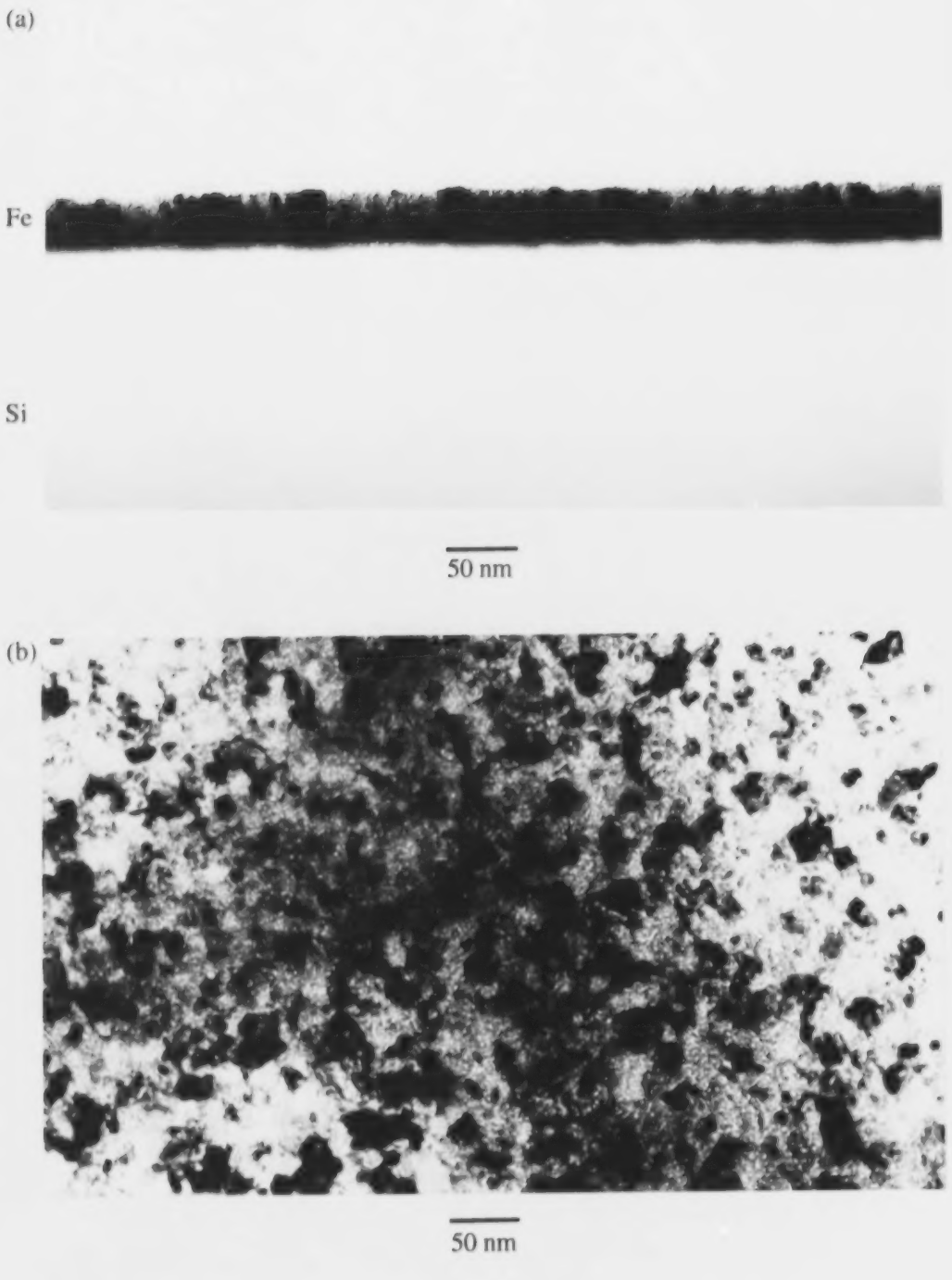

Figure 3-3. As-deposited Fe film on Si(111). Micrograph (a) is a cross-sectional view and micrograph (b) is a plan view.

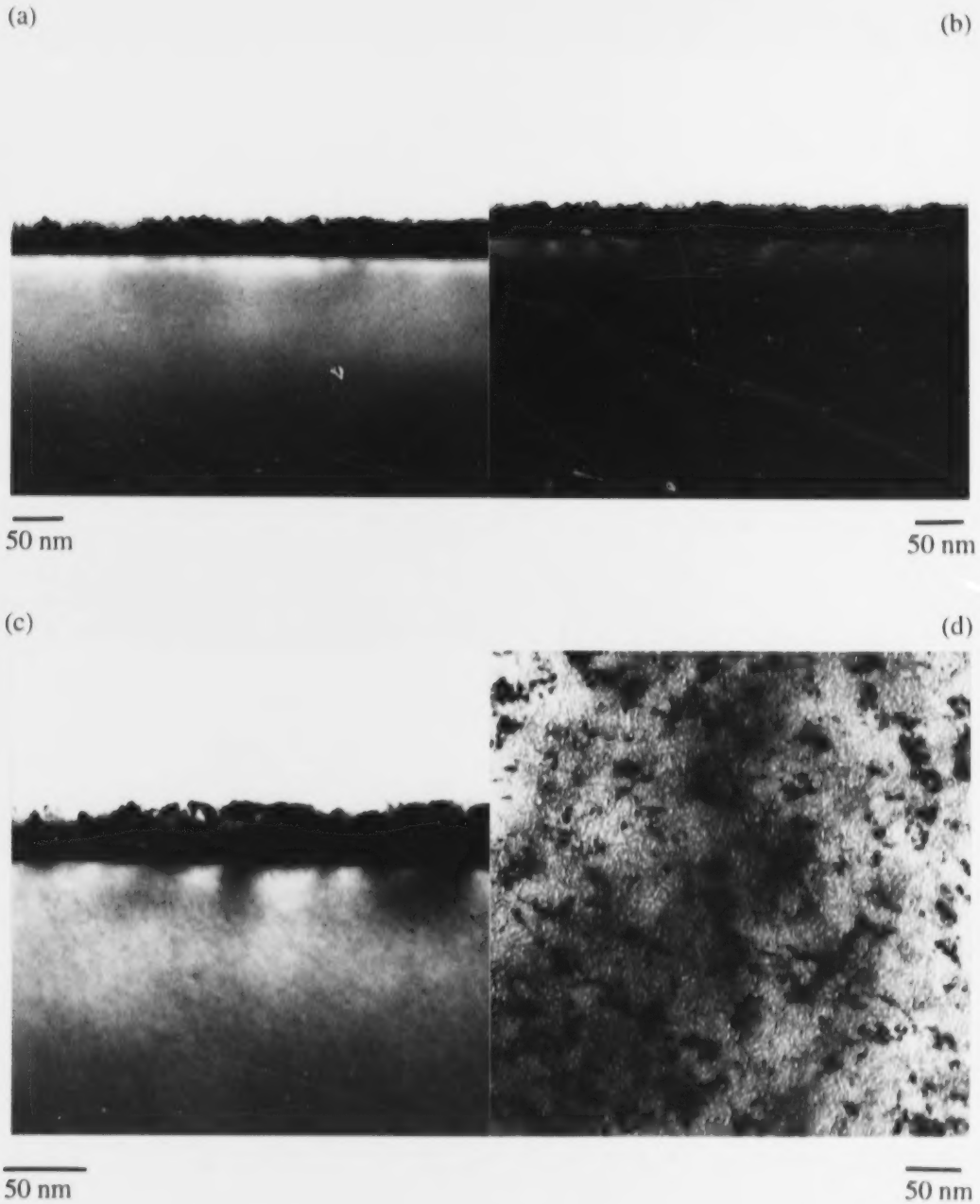

Figure 3-4. Fe film annealed at 300°C. Annealing times are (a) 1 hour, (b) 2 hours, (c) 3 hours and (d) 2 hours (in plan view). It is known that some Fe_3Si is present after 2 hours, but interfaces between α-Fe and Fe_3Si have not been found. It is uncertain what combination of the two phases comprise each of the films seen here.

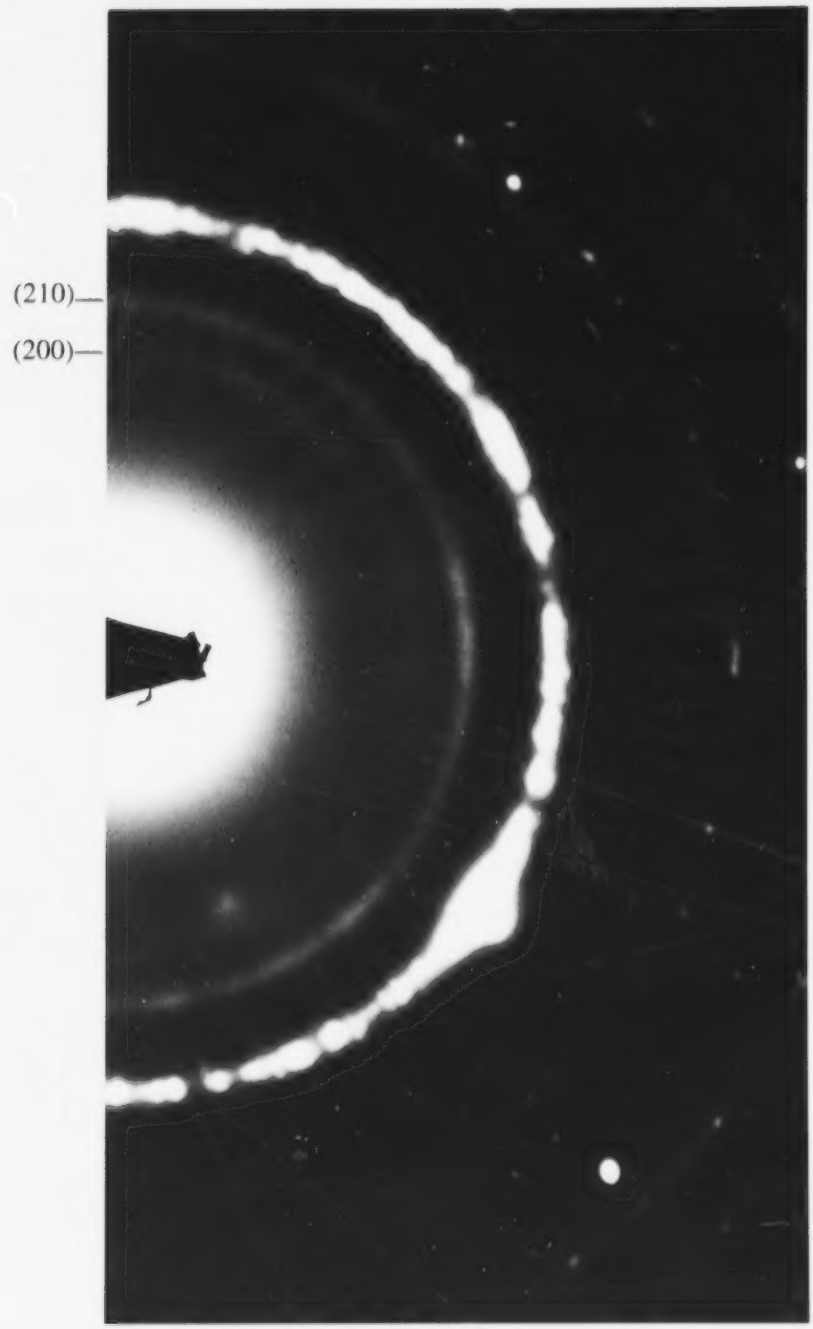

Figure 3-5. Selected area diffraction pattern from Fe film annealed at 300°C for 2 hours. Rings corresponding uniquely to α_1 Fe_3Si planes are identified. The other rings present are ambiguous, and therefore not useful, because they refer to several possible phases.

as-deposited

Si	α-Fe 35 nm

30 minutes

Si	Fe_3Si 10 nm	α-Fe 30 nm

1 hour

Si	FeSi 9 nm	Fe_3Si 10 nm	α-Fe 25 nm

2 hours

Si	FeSi 40 nm	Fe_3Si 18 nm

Figure 3-6. Schematic showing the iron silicide film thicknesses as a function of annealing time at 400°C.

Figure 3-7. Fe film annealed at 400°C for 30 minutes shown in cross-section.

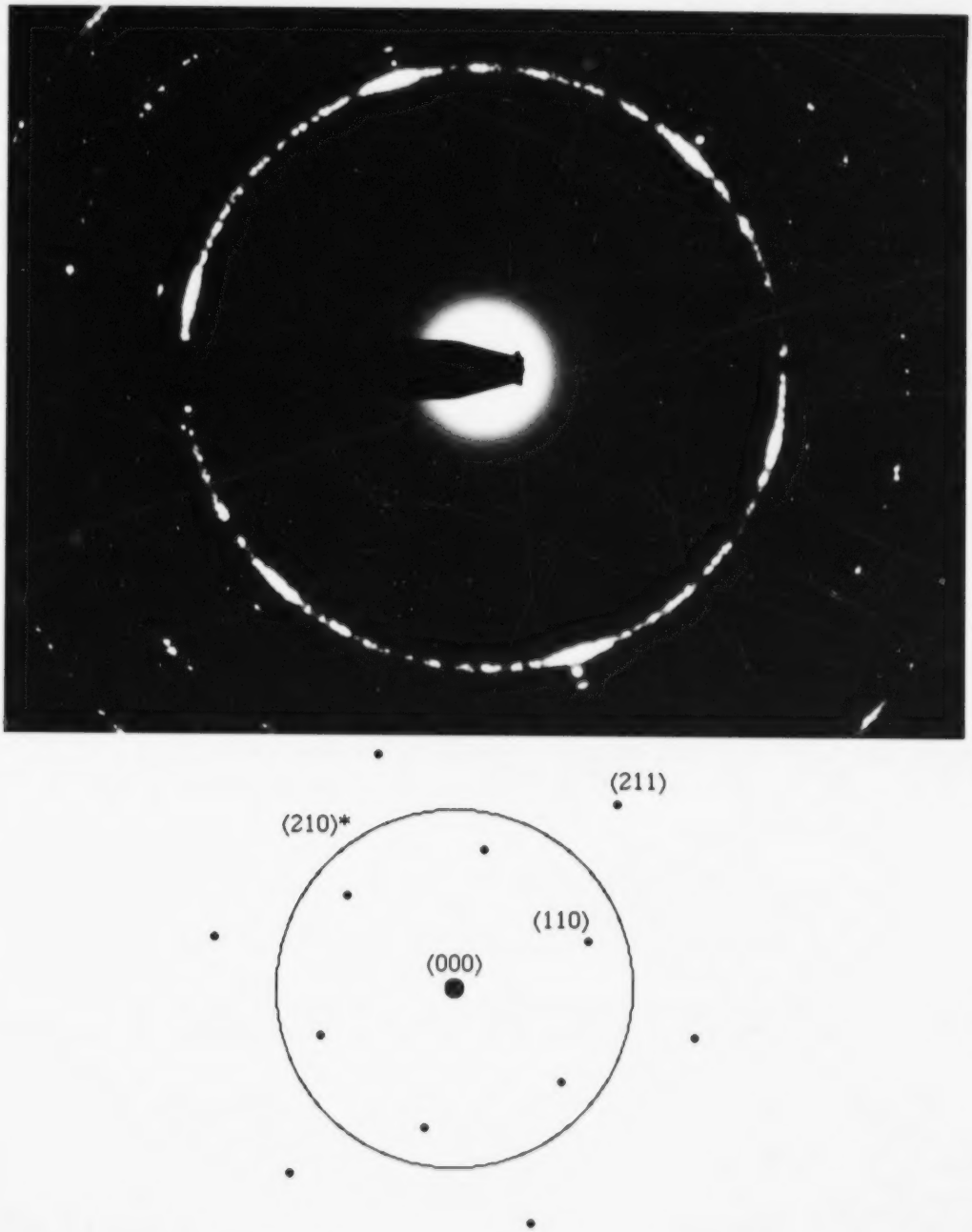

Figure 3-8. Selected area diffraction pattern from Fe film annealed at 400°C for 30 minutes. The FeSi (110) and (211) spots are indexed in the diagram. The α_1 Fe_3Si (210) ring is marked $(210)^*$. The spots just inside the (211) spots are a result of diffraction from Si (220) planes.

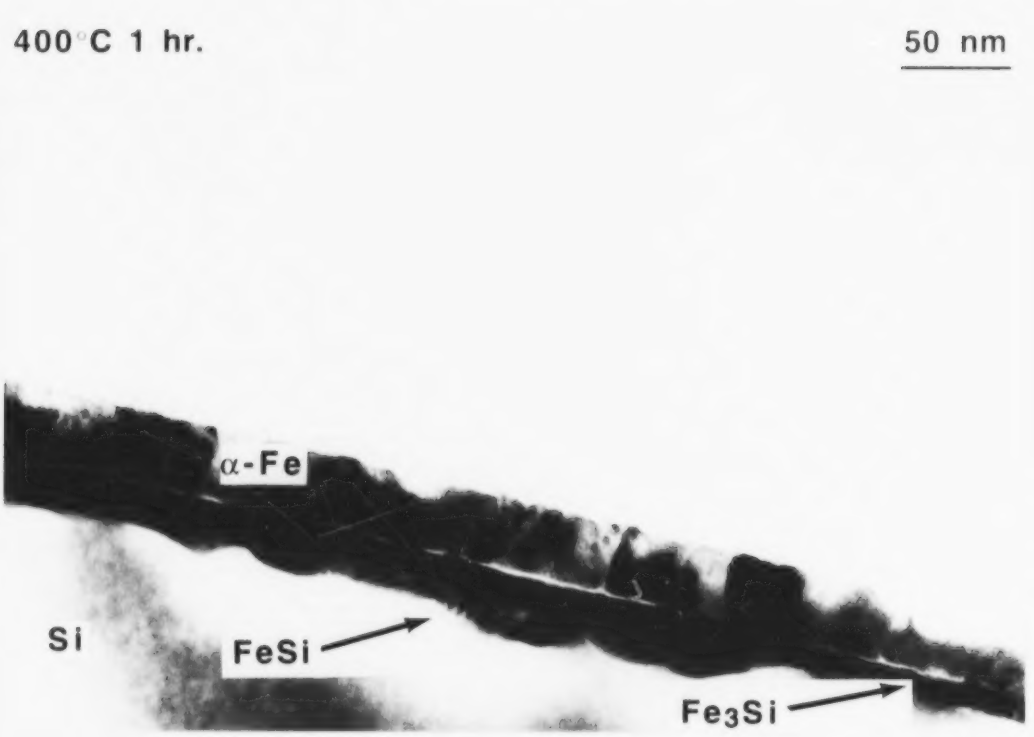

Figure 3-9. Fe film annealed at 400°C for 1 hour shown in cross-section.

Figure 3-10. Fe film annealed at 400°C for 2 hours shown in cross-section.

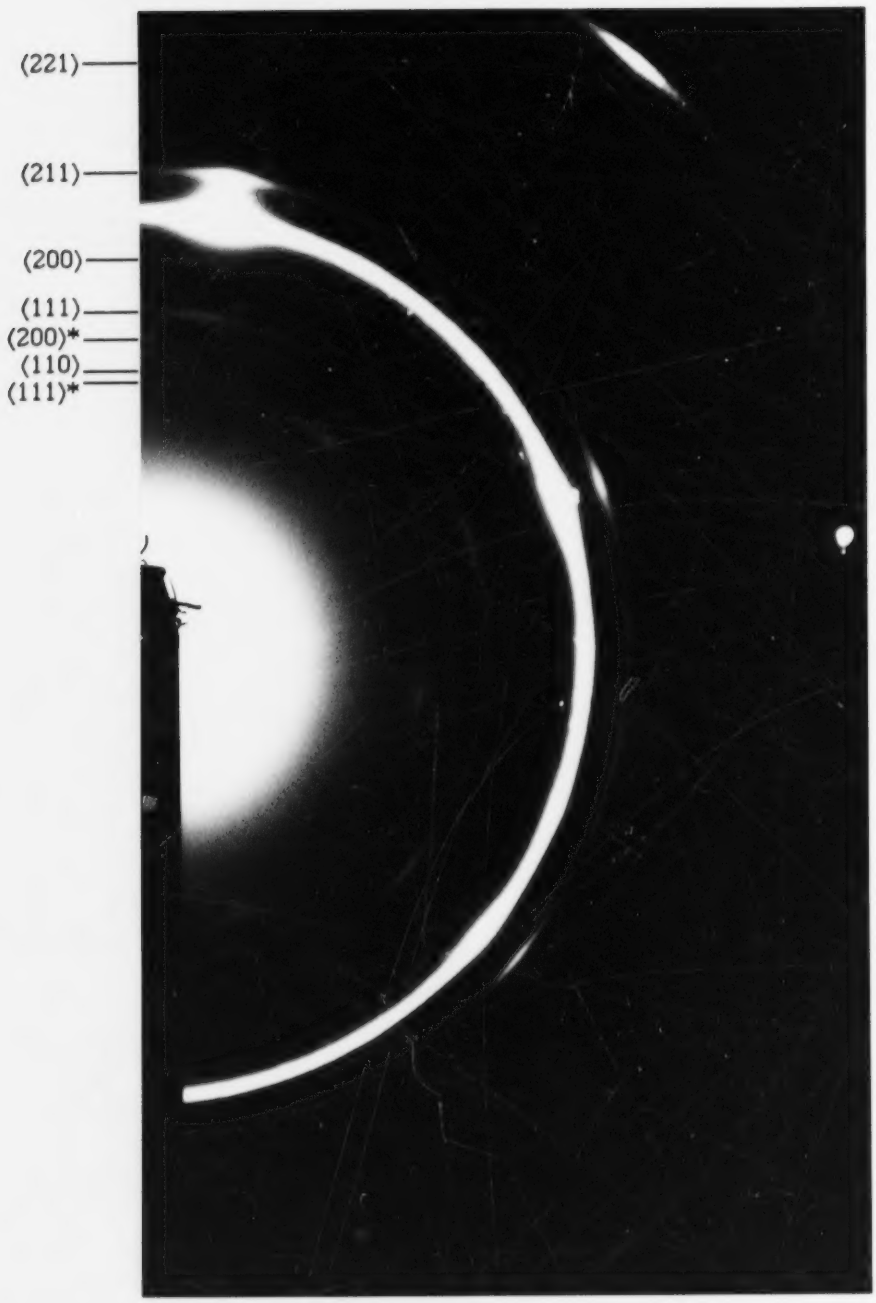

Figure 3-11. Selected area diffraction pattern from Fe film annealed at 400°C for 2 hours. Rings corresponding to both Fe_3Si and FeSi are present. The Fe_3Si rings are indexed as $(hkl)^*$. Rings common to both phases are not indexed.

Figure 3-12. Fe film annealed at 500°C for 15 minutes shown in cross-section. A continuous film of FeSi has formed. The feature indicated by the arrow may be a subcritical nucleus of β-$FeSi_2$. This feature was not characterized as it was found only during the writing of this thesis.

Figure 3-13. Subcritical nucleus of β-$FeSi_2$ in Fe film annealed at 500°C for 1 hour and shown in cross-section. The β-$FeSi_2$ is indicated with an arrow.

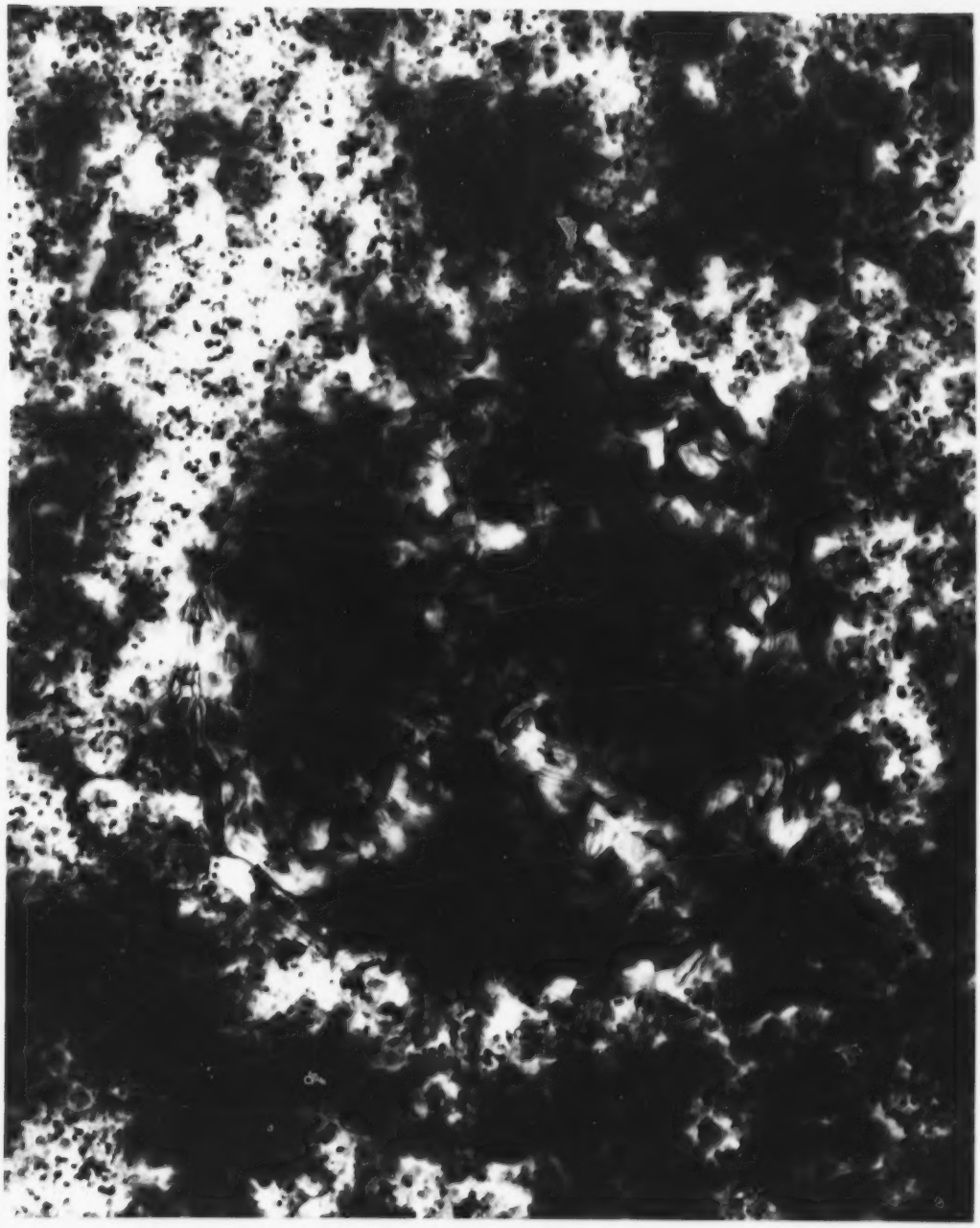

Figure 3-14. β-$FeSi_2$ colony in Fe film annealed at 600°C for 1 hour and shown in plan view. The circular β-$FeSi_2$ colony in the centre is surrounded by FeSi.

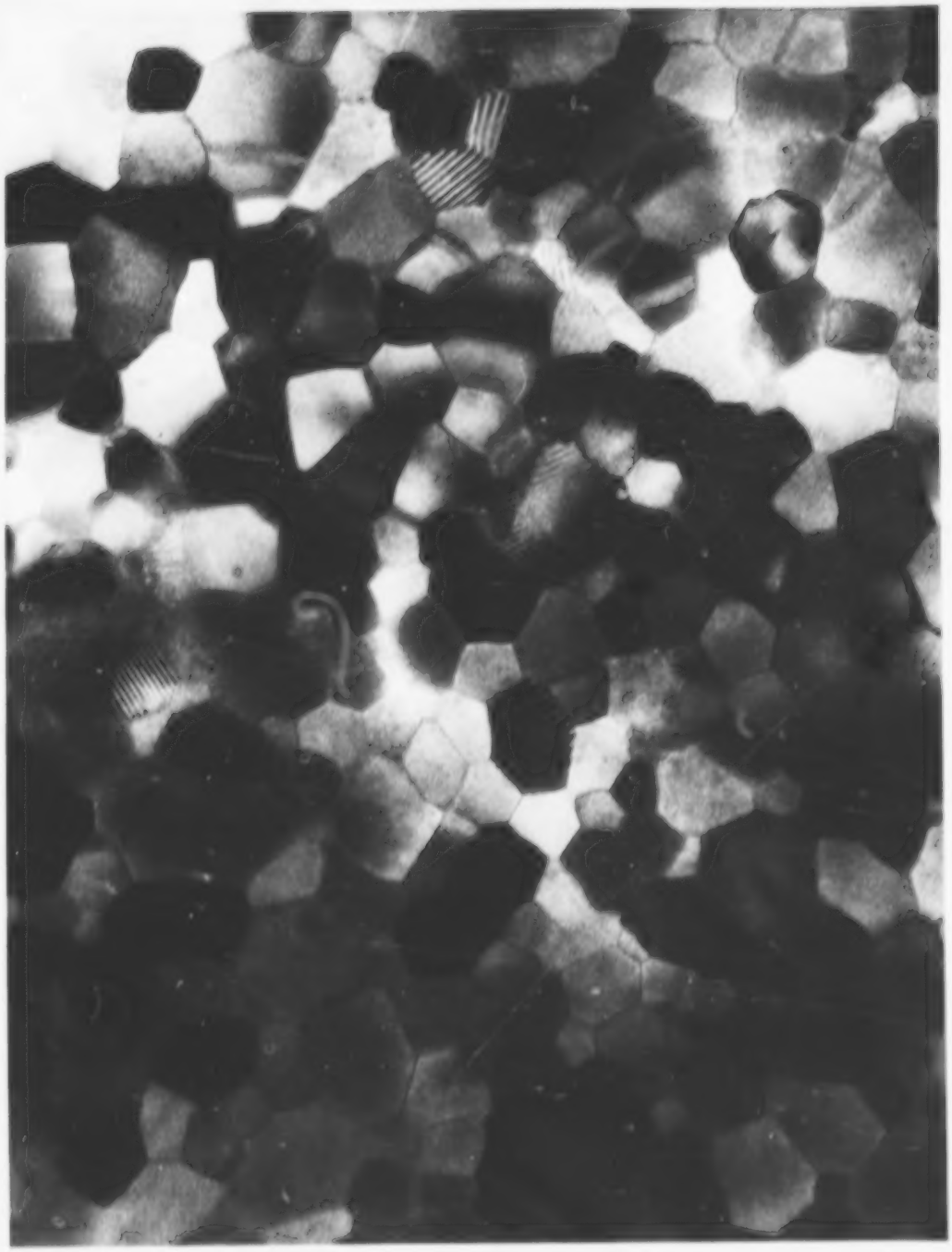

Figure 3-15. High magnification plan view of thin film FeSi.

Figure 3-16. High magnification plan view of thin film β-$FeSi_2$.

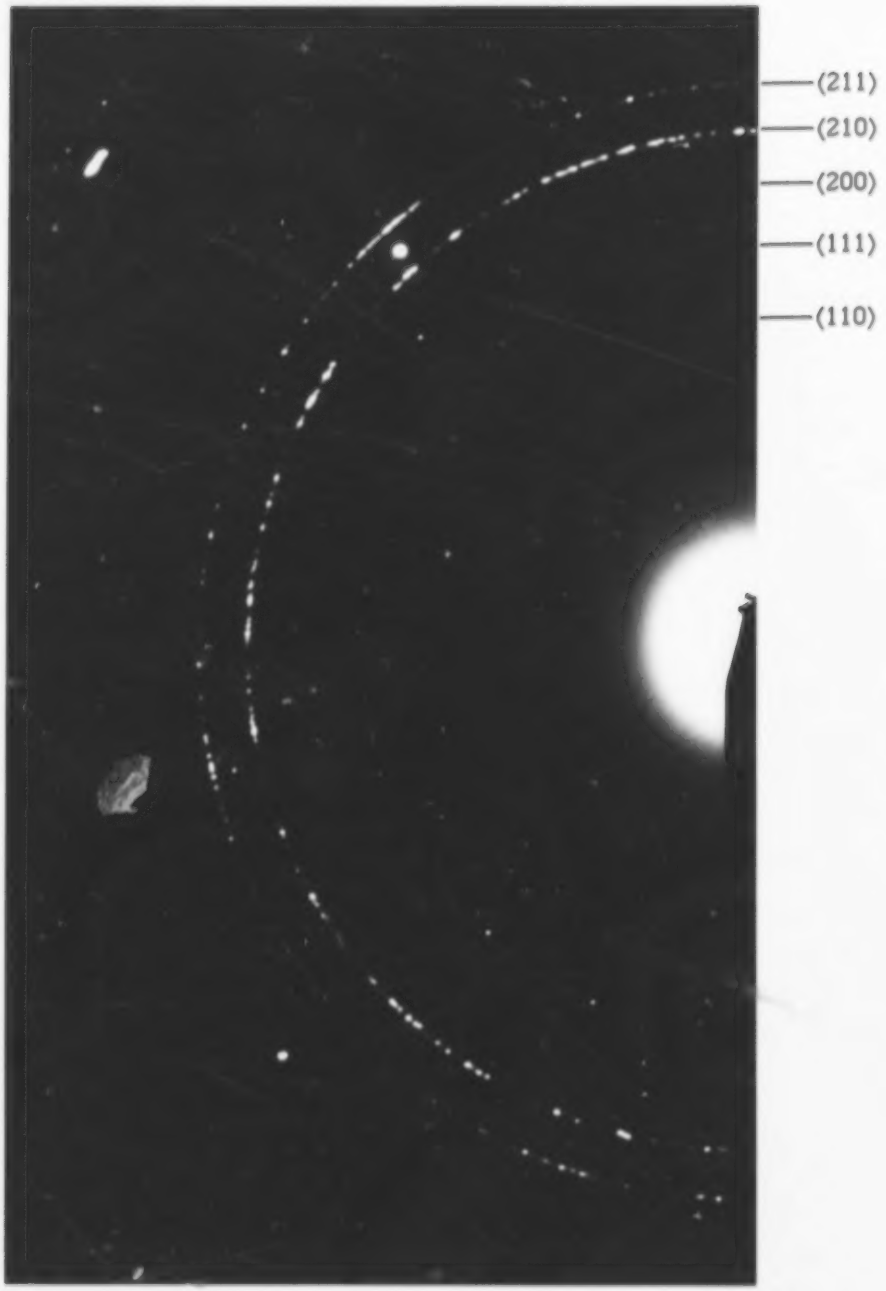

Figure 3-17. Selected area diffraction pattern from Fe film annealed at 650°C for 30 minutes. Rings corresponding to FeSi do not indicate preferential orientation.

Chapter 4 Bulk Diffusion Couples

4.1 Experimental Methods

4.1.1 Fabrication of Couples

Bulk diffusion couples were made by clamping pieces of high purity Fe and Si together between steel plates. The Fe was originally in the form of 6.3 mm diameter rod with a purity of 99.95%. The Si was a cylindrical single crystal about 22 mm in diameter. Its purity is assumed to be very good as high purity is required to grow single crystal Si. Pieces were cut from the Fe rod with a slow speed diamond saw. The Fe pieces were cut perpendicular to the rod axis so that all of the Fe pieces would have the same circular area on their ends. From the Si crystal, slices were cut with the diamond saw and these slices cut into smaller pieces. All the Si pieces were cut so that their area contacting the Fe surfaces would be at least a 5 mm by 5 mm square.

The surfaces of both the Fe and Si pieces were ground and polished using the same steel jig described in the preparation of TEM samples. The piece to be ground was glued with low melting point glue to a cylindrical steel stage that was inserted into the center of the jig. The Fe pieces were ground so that their thickness (along their cylindrical axis) was exactly 4.50 mm. The Si pieces were ground so that their thickness was exactly 3.00 mm. The faces of the pieces that were to be the reacting interfaces were polished to a mirror finish on a 6 μm diamond wheel and a 0.05 μm Al_2O_3 wheel. Polishing, especially in the case of the Fe, was done only shortly before fabrication of the couples so as to prevent oxidation of the polished surfaces. Between polishing and couple fabrication, the Fe and Si components were kept in desiccators.

The clamping device for each couple consisted of two square carbon steel plates measuring 20 mm by 20 mm and ~2 mm in thickness. Four corner holes were drilled in each plate so that the plates could be tightened with screws. The four corners of each plate were ground to arcs parallel to the arcs of the corner holes. The bottom plate of each pair had threaded holes while the holes in the top plate were slightly larger and unthreaded. Threading the bottom holes eliminated the need for nuts. Figure 4-1 is a diagram of a clamp plate. The screws used were $\frac{1}{2}$ inch (12.7 mm) long uncoated carbon steel 4-40 screws with hex heads so that they could be tightened with an Allen key.

All of the clamping material was carbon steel (and verified by EDS to be carbon steel), because early trials in which stainless steel plates and screws had been used failed badly. Chromium from the stainless steel formed volatile phases, thought to be primarily chromium oxides, during the high temperature annealing. These gases rapidly attacked Fe, Si and SiO_2 surfaces to produce ternary and quaternary compounds which condensed as thick films and powdery precipitates.

The diffusion couples were cleaned, assembled and placed in desiccators only hours before they were to be sealed in quartz glass tubes. Clamping plates and screws were ultrasonically cleaned in acetone and ethanol. The polished Fe surfaces were wiped and rinsed in acetone and ethanol and immediately blown dry with N_2. The polished Si surfaces were also wiped clean in acetone and ethanol, then etched in buffered oxide etch for 60 seconds, rinsed in distilled water, and blown dry with N_2. A Si piece and an Fe piece were stacked, polished surfaces together, between each pair of steel plates and the four screws tightened by hand with an Allen key. Care was taken to tighten the screws so that the plates would remain parallel and the pressure uniform. Gloves were worn during the couple assembly.

4.1.2 Annealing

To protect the diffusion couples from oxidation during the anneals, the couples were sealed in individual evacuated quartz glass tubes. It was necessary that the glass be quartz because of the high annealing temperatures. The tubes were approximately 15 cm long and were 1 inch (25.4 mm) inside diameter. Each tube contained 1.0 gram of pure zirconium powder as well as a diffusion couple. The purpose of the Zr was to getter the oxygen still present inside the tube so that surface oxides would not prevent silicides from forming. When just sealed, the tubes were estimated to contain a total pressure of about 10^{-4} torr. Once at high temperature, the Zr acted to further lower the oxygen pressure to below the decomposition pressure of SiO_2 and all Fe oxides. All oxides, including the inner surface of the quartz were reduced by the preferential oxidation of the Zr. The iron and steel surfaces were much cleaner and shinier after removal from the tubes than prior to annealing. As further evidence that Zr does reduce the oxides, Table 4-1 contains the Gibbs free energies for oxidation of the various metals involved [96]. Although the free energies of oxidation are for the standard state of 1 atmosphere pressure, the effect of the low oxygen pressure is approximately the same for all the reactions and the oxidation of Zr is by far the most favored reaction.

Table 4-1: Gibbs Free Energies of Oxidation

Oxidation Reaction	ΔG° at 710°C (kJ/mol O_2)	ΔG° at 750°C (kJ/mol O_2)	ΔG° at 800°C (kJ/mol O_2)
$2\,Fe + O_2 \Rightarrow 2\,FeO$	-393	-389	-384
$6\,FeO + O_2 \Rightarrow 2\,Fe_3O_4$	-381	-370	-357
$4\,Fe_3O_4 + O_2 \Rightarrow 6\,Fe_2O_3$	-221	-208	-195
$Si + O_2 \Rightarrow SiO_2$	-732	-722	-715
$Zr + O_2 \Rightarrow ZrO_2$	-895	-887	-879

Five diffusion couples were annealed at 710°C, six at 750°C and six at 800°C. The furnace controllers were adjusted to maintain the proper temperatures by calibration with an external thermocouple that was accurate to within 1 degree Celsius. The controllers were able to hold the furnaces at the preset temperatures without deviations of 1 degree Celsius in either direction. The diffusion couples were placed quickly into the furnaces, which were already at the annealing temperature, and typically only 3-4 minutes was required for a furnace to be fluctuating in a ± 5°C zone about the setpoint. About 10 minutes after inserting the couples, the furnace temperature would be stable on the setpoint. The diffusion couples were placed in the furnaces so that none were more than 8 cm from the point at which the external thermocouple had calibrated the temperature. Because of the large heat capacity of these furnaces and the significant role of radiation in heat transfer at temperatures above 700°C, it is unlikely that the temperatures of the couples in any one furnace varied by more than one degree.

The annealing times ranged from 72 hours to 2070 hours. Shorter times were used at the higher temperatures since the reactions proceed faster. The annealing times are so long that the few minutes spent between the annealing temperature and room temperature (after couple insertion and removal) represent an insignificant fraction of the total anneal -- on average less than 0.05%.

4.1.3 Metallographic Preparation

After cooling to room temperature, each diffusion couple assembly was removed from its quartz tube and compressed air was used to blow any Zr powder or glass off the couple. Care was taken not to twist or jar the couple so that the brittle silicide layers would not be cracked during handling. The couple -- steel plates, screws and all -- was mounted

in about 20 grams of a cold mount material which solidifies at room temperature, thus making it unnecessary to heat and pressurize the couple during mounting. The mounted couple was then cut perpendicular to the reaction interface with a low speed diamond saw. Of the two halves of each couple, one was polished for examination. Polishing was done on four different polishing wheels: (1) a 10 μm diamond-impregnated wheel, using water as the lubricant and with the motor off, (2) a napless lap with 6 μm diamond paste and an oil lubricant, (3) a napless lap with 1 μm diamond paste and an oil lubricant, and (4) a napless lap with 0.05 μm Al_2O_3 suspension and distilled water for lubricant.

4.1.4 Characterization

The silicide layers formed in the bulk diffusion couples were characterized by scanning electron microscopy (SEM). The SEM used was a Hitachi S-2700 with a Link eXL energy dispersive Si detector with a Be window. Essentially all of the SEM imaging was done with the backscattered electron signal which generated average atomic number contrast between the various phases in the couples.

One of the major goals of the bulk diffusion couple work was to calculate the silicide layer thicknesses as a function of time and temperature. This is why diffusion couples were annealed at three temperatures and various times. The entire length of every diffusion couple interface was imaged and recorded with a video printer connected to the microscope monitor. From these video prints, the average thicknesses of the FeSi and β-$FeSi_2$ layers were determined by hand measurement. In order to make the results statistically meaningful, five different measurements were made on each video print and the positions of the measurements were chosen at random (that is, without looking at the print). Because the interface lengths varied, the number of videoprints taken of an interface and therefore the number of total measurements also varied, but there were always more than 80 and typically about 100 measurements per couple. No measurements were taken in areas where metallographic artifacts/damage obscured the phase boundaries. Areas which were obviously displaying very unrepresentative silicide growth, usually because of large cracks in the Si source or because of close proximity to the end of the interface, were also rejected. Thickness measurements were made perpendicular to the original Fe/Si interface and the video prints were always taken at the same magnification. The widths of voids, of which there were many within the silicide layers, were not subtracted from the silicide thicknesses. From all the thickness measurements for each silicide of each couple, a mean thickness was found and the standard deviation of the data computed.

The second principle component of the SEM work was performing EDS analysis on the diffusion couples to check phase identities and compositional gradients. Spectra were collected from pure powder standards of FeSi and β-$FeSi_2$ and used to quantify the Fe:Si ratios of the analyses. All experimental spectra were collected at a working distance of 12 mm from the level surface, with the backscatter detector out, and during a 100 second live time period with dead time being about 20% of real collection time.

4.2 Results and Discussion

4.2.1 EDS Work: Phases and Compositions

The procedure developed for fabricating Fe-Si bulk diffusion couples proved successful. The annealing temperatures and times for the 17 diffusion couples are listed in Table 4-2.

Table 4-2: Bulk Diffusion Couples Produced

Temperature (°C)	Annealing Time (hours:minutes)					
710	384:06	650:32	971:10	1322:55	1518:14	
750	112:54	310:38	505:26	695:36	923:25	2070:45
800	72:13	144:47	211:07	288:28	357:36	430:50

Every one of the couples produced layers of iron silicides along its entire interface length and the addition of the Zr powder was a crucial part of this success rate -- earlier trials without the Zr produced reaction areas that covered only a small fraction of the total interface. No Zr was detected by EDS to have entered any of the diffusion couples.

Compositional gradients and phase identities were determined with EDS. All of the annealed couples contained the same five phases, each phase having a consistent composition. The five phases and their compositions are listed below in Table 4-3.

Table 4-3: Phases Observed in Bulk Diffusion Couples

Phase	Composition (atomic %)
Si	virtually pure Si
β-$FeSi_2$	33% Fe and 67% Si
FeSi	50% Fe and 50% Si
Fe_3Si	75% Fe and 25% Si
α-Fe	solid solution with ≤ 6% Si

Figure 4-2 is an SEM micrograph of the interface of one of the diffusion couples. The five layers mentioned can all be clearly discerned as a result of the average atomic number contrast in the backscattered electron signal. As well as these layers, a significant gap can be seen running parallel to the interface and between the Fe_3Si and α-Fe. Such a gap of missing material was present in all the diffusion couples and is an artifact of preparation. It is not known conclusively how much of the material that is broken and removed to create a gap is α-Fe and how much is Fe_3Si. However the missing material is believed to be primarily Fe_3Si. The Fe_3Si is brittle and unable to deform like the ductile α-Fe next to it. It is believed to be the sharp contrast in mechanical properties between these two neighboring phases that causes a gap to be consistently created at this interface, while the other interfaces endure polishing very well.

As discussed in the experimental methods section, the EDS was quantified against pure powder standards of β-$FeSi_2$ and FeSi. These standards led to improved accuracy of the analyses, but unfortunately the EDS results could still not be considered fully quantitative. Precision, that is the consistency of measurements, was very good, but accuracy was somewhat lacking.

The error in the EDS work can be considered to consist of three components:

(1) Error in the collection of standard spectra. This leads to an error component that is present and identical in all analyses.

(2) Errors due to differences between specimens. This leads to an error component which is the same for all measurements from a given specimen but varies between specimens.

(3) Errors due to variations between measurements. This error component is different in each individual measurement and causes scatter among all data.

The first type of error, the error generated during standard collection, is thought to be due primarily to the fact that the standards were in powder form. Iron silicides were

available only as powders and so the standards were not the flat, polished, level and semi-infinite surfaces that EDS standards should be ideally. The presence of this type of error explains why the analyses were not scattered about the actual stoichiometries, but instead grouped tightly on one side. The calculated Fe/Si ratios were almost always too high, rather than too low. Typically the computed atomic % of Si was about 0.94 of the actual Si concentration. That both β-$FeSi_2$ and FeSi are actually stoichiometric has been firmly established previously by other researchers[1,23,97].

The second type of error in the EDS analysis is caused by differences between the specimens. Possible variables include surface cleanliness and levelness. Although samples were prepared with the same metallographic procedures and all loaded into the SEM so as to be as level as possible, small variations are inevitable. The existence of such a specimen-to-specimen error is confirmed by the variations seen in the central tendencies of the compositional measurement distributions. To elaborate, although a given phase shows quite a narrow compositional range in both of two different specimens, the means of the two distributions are several standard deviations apart.

The third type of error is easily understood and arises from variables like local contamination of the sample, microscope operation variables, and statistical chance in the collection of the X-rays. This type of error causes the scatter between the individual points and, in some cases, this error was large enough to totally obscure the shallow concentration gradients across phases.

Compositional measurements were made on all five phases found in the diffusion couples. Table 4-4 shows the total number of EDS measurements taken for each phase.

Table 4-4: Number of EDS Measurements Taken

Phase	Total Number of Measurements
Si	4
β-$FeSi_2$	29
FeSi	33
Fe_3Si	45
α-Fe	50

The compositional range across each of the silicide phases was very narrow. Since the stoichiometries of the silicides show little variability, it is difficult to separate scatter in the data from the small compositional gradients that exist. As shown in Table 4-5, a series

of compositional analyses taken at points across the thickness of a silicide layer usually varied by less than 1 atomic % from highest to lowest. In Table 4-5, the highest and lowest atomic percentages of Fe found are listed for each silicide layer on which at least 4 EDS measurements were made. Each couple is identified by the temperature and time of its annealing, the times being written in the form hours:minutes.

Table 4-5: Ranges of EDS Results on Iron Silicides

Phase	Diffusion Couple	Number of EDS Data	Fe Concentration (atomic %)		
			High	Low	Actual
β-$FeSi_2$	710°C 1322:55	4	37.3	37.0	33.3
	750°C 695:36	4	37.7	37.4	
	800°C 144:47	4	35.3	35.0	
	800°C 144:47	5	35.3	34.6	
	800°C 357:36	5	38.0	37.3	
FeSi	710°C 1322:55	4	54.5	54.2	50.0
	750°C 695:36	5	54.7	54.1	
	800°C 144:47	8	51.6	51.3	
	800°C 144:47	8	52.3	51.2	
	800°C 357:36	5	54.6	54.2	
Fe_3Si	710°C 1322:55	5	77.1	76.6	75.0
	710°C 1518:14	4	76.6	76.1	(assumed)
	750°C 310:38	5	75.9	75.5	
	750°C 695:36	4	77.0	76.9	
	800°C 144:47	5	74.9	74.2	
	800°C 144:47	6	74.8	73.3	
	800°C 211:07	7	75.6	75.1	
	800°C 357:36	5	77.1	76.6	

The above table shows how narrowly the data from a layer of a single specimen is distributed. This narrowness reflects both the good precision of the EDS and the very small ranges that exist in the stoichiometries of the iron silicides.

If compositional gradients exist across the silicide layers, they are very shallow. It is difficult to separate such gradients from random scatter. The data taken from any silicide layer falls within a small range, as demonstrated above in Table 4-5. But the data of a compositional gradient would be expected to show not only a range but also a trend, with the concentration of element A being higher near the interface with the neighboring phase that is richer in element A, and lower near the interface with the phase poorer in element A.

Compositional data was collected from across all the silicide layers of one selected couple at each of the three annealing temperatures (710°C, 750°C and 800°C). The data from the silicide layers of these three couples was used in an attempt to determine (1) the stoichiometric ranges of the silicides and (2) whether any gradients can be demonstrated to exist despite the scatter in the data from error sources. Linear regression was performed on each of the data sets and the generated equations used to determine the compositional end-points of the silicide. Direct measurement of the concentration near an interface is not possible because of the volume of sample material that interacts with the electron beam.

Table 4-6: Computed Compositional End-Points, Ranges and Gradients of the Silicides

Temperature (°C)	Phase	Calculated End-Point (atomic % Fe)		Calculated Range of Stoichiometry (atomic %)	Gradient $\delta c/\delta x$ (at.% / mm)
		Low	High		
710	β-$FeSi_2$	37.0	37.4	0.4	12.
750	β-$FeSi_2$	37.4	37.6	0.2	5.
800	β-$FeSi_2$	37.3	38.0	0.7	19.
710	FeSi	54.2	54.5	0.3	6.
750	FeSi	54.2	54.4	0.2	-4.
800	FeSi	54.3	54.4	0.1	3.
710	Fe_3Si	76.5	76.9	0.4	-8.
750	Fe_3Si	76.9	77.0	0.1	-2.
800	Fe_3Si	76.7	77.0	0.3	-4.

In Table 4-6, the calculated end-points are summarized. The stoichiometric range, the difference between a pair of end-points, is more meaningful than the end-points themselves, given the errors in the EDS measurement technique. So the computed range of composition is tabulated as well. The gradient across a layer, $\frac{\delta c}{\delta x}$, is simply the difference

in atomic percentage between the two end-points divided by the physical width of the layer. Computed gradients that did not run in the expected direction are tabulated as being negative.

Several points can be deduced from the computed values of Table 4-6. First, computed stoichiometric ranges of all the silicides are very small, leading to compositional gradients with very shallow slopes. This is in agreement with the present Fe-Si phase diagram in the cases of FeSi and β-$FeSi_2$, but not in the case of Fe_3Si. This discrepancy will be discussed at length later. Second, four of the nine calculated gradients slope the wrong way -- there is no apparent energy source that could promote "uphill" diffusion in these couples. Therefore it seems that these four results must contain significant error. Furthermore, because of the magnitude of error necessary to account for the -8 atomic % / mm gradient, all of the computed gradients are quite questionable. Unfortunately, it seems unlikely that it is possible, using EDS, to quantify the compositional gradients across such iron silicide layers. If the layers were thinner, the gradients would steepen only slightly and fewer independent EDS data could be obtained because of the finite interaction volume, thus degrading the accuracy of statistical calculations.

The two other phases present in the diffusion couples, the α-Fe and the Si, were checked for compositional variation as well. The diffusion couple which was annealed at 710°C for 1518 hours was used to measure Fe diffusion into the Si. Figure 4-3 contains the EDS data obtained from the Si. As would be expected, the concentration of Fe is highest near the interface with the $FeSi_2$ and decreases with distance in an exponential manner. The measurement taken at 1.58 μm from the interface is 1.8 % (atomic) Fe. Judging by experience gained with the EDS system during this work, it is now thought that this measurement was probably too close to the interface to completely exclude signals from the $FeSi_2$. The second EDS point is thought to have been sufficiently far from the interface though (3.98 μm), and at this point the Si concentration was 0.5%. The maximum concentration of Fe reached within the Si was probably between these two values. This is higher than predicted by the Fe-Si phase diagram which shows Fe solubility in Si to be essentially zero at all temperatures below the melting point of Si.

Analysis of the Fe was performed on numerous diffusion couples. The most thorough of these analyses was done on the couple annealed at 800°C for 211 hours. The 16 data points taken for the construction of this concentration profile are plotted in Figure 4-4. An exponential equation, fitting the data very well, is also plotted in the figure. This equation gives a maximum Si concentration of 4.1% (atomic) at the interface. This profile and maximum Si concentration is in agreement with the EDS data collected from various

other diffusion couples. However, all of this experimental data is not in agreement with the present Fe-Si phase diagram, which predicts that α-Fe will dissolve 10-12 atomic percent Si at such temperatures. Furthermore the phase diagram predicts that, at Si concentrations greater than this, an ordered solid solution occurs which dissolves more Si, up to 25%. In the next section, the 0-25% Si region of the phase diagram and the contradiction that this research poses are discussed.

4.2.2 Fe_3Si in the Fe-Si Phase Diagram

The presently accepted Fe-Si phase diagram is drawn in Figure 1-1. The diagram predicts that, in equilibrium, α-Fe dissolves Si up to ~12% (atomic) at 800°C. At 750°C and 710°C the solubility limit is only 1-2% lower. According to the diagram, at Si concentrations between ~12% and ~25%, the Fe-Si solution phase becomes one of two ordered structures, discussed earlier in this paper. The two ordered structures, called α_1 and α_2, are both commonly referred to as Fe_3Si. Presumably, these two ordered structures are labelled in Figure 1-1 as α_1 and α_2 to indicate their difference from the disordered α-Fe phase, yet also to suggest that the three structures are not entirely separate phases. Why Fe_3Si should not be considered as a phase distinct from the α-Fe solid solution is not entirely clear and this corner of the phase diagram seems suspiciously odd.

In any case, the experimental data of this research contradicts the phase diagram as it presently exists. In Figure 4-5, two diffusion couple compositional profiles are contrasted. The profile marked with a solid line is from the diffusion couple annealed at 800°C for 357 hours. Each of the dots is an EDS point that was used to calculate this experimental profile. The profile within each of the three silicides was assumed to be linear and was computed by linear regression for the entire width of the silicide layers. A polynomial equation was fit to the α-Fe data. The second profile of Figure 4-5 is marked with a dashed line and is the result that would be predicted from the phase diagram. This profile is different from the first because it does not have a third step at ~25% Si. Since, in the phase diagram, there are no two-phase regions between the α-Fe, α_2 and α_1, this theoretical profile contains no step. Since the transition from one structure to another is supposed to occur smoothly with no compositional gap between, this profile has no vertical segment between the Fe_3Si and Fe.

It is obvious that, given the number of data points used to construct the experimental profile, there is a most definite disagreement between the phase diagram and this work. The same experimental profile -- three virtually flat steps and an α-Fe solid

solution of <5% Si -- was generated from several other diffusion couples. The experimental findings were completely consistent, at all three temperatures and all annealing times.

The phase diagram is, of course, designed to represent equilibrium conditions. The possibility that the apparently stoichiometric Fe_3Si phase was not actually an equilibrium phase was considered. To test this, the Fe_3Si was checked by EDS after very long anneals. Results from the diffusion couple annealed at 710°C for 1518 hours (≈ 2 months) are in Figure 4-6. The variation in concentration across the entire layer width is not more than 1%. The silicide was still present in large quantities. It did not appear to be disappearing. Results from the couples annealed at 800°C for 430 hours and 750°C for 2070 hours also support the conclusion that Fe_3Si is an equilibrium phase containing ~25% (atomic) Si and having virtually no range of stoichiometry.

4.2.3 Growth Kinetics of β-$FeSi_2$ and FeSi

The average thicknesses of the β-$FeSi_2$ and FeSi layers of each diffusion couple were calculated and plotted. Average thicknesses were not computed for Fe_3Si because the gaps of missing couple material that exist between the Fe_3Si and α-Fe layers prevented measurement of the actual widths of the Fe_3Si. The standard deviation of the thickness of each layer was also calculated so as to provide some measure of the level of confidence in the data. The standard deviations of the FeSi thicknesses were consistently larger than those of the $FeSi_2$ thicknesses, simply because the $FeSi_2$ was invariably the silicide with the highest uniformity of thickness in the couples. This can be seen in Figure 4-2.

It would be expected that such thick silicide layers would follow parabolic growth kinetics, the rate of growth being controlled by diffusion through the layers themselves. The thickness data clearly shows this to be true for the β-$FeSi_2$. Figures 4-7 to 4-9 are the β-$FeSi_2$ mean thickness data sets, for 710°C, 750°C and 800°C anneals respectively, plotted against the square root of time. The error bars represent one standard deviation (±) in thickness. (One point in Figure 4-9 does not have an error bar for reasons discussed in the next section.) Best fit lines by linear regression fall within the error bars of all the data points. The clear linear trend of the data sets verifies that the growth is parabolic and allows a calculation of the temperature dependence of the β-$FeSi_2$ growth.

The equations for the best fit lines of Figures 4-7 to 4-9 are of the form

$$x = k\cdot\sqrt{t} + c \qquad (2),$$

where x is the thickness of the β-$FeSi_2$ layer in μm, t is time in hours, k is a parabolic rate constant and c is a small constant. If the growth kinetics were perfectly parabolic and there were no errors in the linear fits, c would be zero. In actuality, c equals 3.08 μm, 5.32 μm and 0.84 μm for the 710°C, 750°C and 800°C equations respectively. The existence of these small non-zero values for c was disregarded for the purpose of quantifying temperature dependence.

Since diffusion, which controls the growth rate of the silicide layer, is exponentially rate dependent on temperature, it follows that the parabolic rate constant is related to temperature in an exponential way:

$$k = A \cdot e^{(-Q / RT)} \qquad (3).$$

In Equation 3, A is a constant, Q is an activation energy per molar unit, R is the gas constant, and T is the absolute temperature. Taking the natural logarithm of both sides of this equation yields

$$\ln(k) = \ln(A) - \frac{Q}{R}\frac{1}{T} \qquad (4),$$

Equation 4 is a linear equation of ln(k) as a function of the reciprocal of temperature. The slope of the equation, $\frac{Q}{R}$, provides the activation energy for the diffusion controlled growth. Figure 4-10 is Equation 4 plotted with the β-$FeSi_2$ data. The logarithms of the parabolic rate constants show a reasonably good linear relationship. The resulting value for the activation energy, Q, is 80400 J/mol or 80.4 kJ/mol and the constant, A, is approximately 14070 μm / $\sqrt{\text{hour}}$. Substituting these numbers into Equation 3 produces

$$k = 14070 \cdot e^{(-80400 / RT)} \ \ \mu m / \sqrt{hour} \qquad (5).$$

This activation energy of 80.4 kJ/mol is equivalent to 0.83 eV. This is lower than the literature values estimated from thin film β-$FeSi_2$ growth. Radermacher *et al.* published an activation energy of 2.6 ± 0.5 eV (250 ± 50 kJ/mol) for continuous β-$FeSi_2$ films growing on single crystal Si [45]. Erlesand *et al.* obtained an activation energy of 1.5 ± 0.1 eV (150 ± 10 kJ/mol) for β-$FeSi_2$ growing on amorphous Si substrates [46]. It is difficult to explain what factors might account for the variation between these determined

activation energies because none of the experiments were very similar. The value of 0.83 eV for the present study would indicate a lower degree of temperature dependence than was present in the two thin film studies. This may indicate that diffusion, which surely controlled the kinetics in the bulk diffusion couples, was not actually the limiting factor in the thin film work of [45] and [46]. In the bulk diffusion couples, the silicide layers grew much thicker than the silicides of the other two studies. The diffusional gradients were relatively shallow in the bulk couples, resulting in slower diffusion in this experiment. It is possible that kinetic processes other than diffusion were rate limiting in the growth of the thin β-$FeSi_2$ of [45] and [46], but that this step or steps soon ceased to become rate limiting in the bulk diffusion couples once the β-$FeSi_2$ growth had slowed the diffusion flux sufficiently. These possible kinetic processes might include the rate at which Si atoms are released from the Si lattice (or from the α-Si structure), the rate at which FeSi "molecules" are released from their lattice for reaction, and the rate at which the β-$FeSi_2$ "molecules" form and align themselves to the disilicide lattice.

For the FeSi, the mean thickness data for 710°C, 750°C and 800°C are plotted in Figures 4-11 to 4-13. As before, error bars represent one standard deviation (±) in thickness. The error bars are larger relative to the magnitude of the mean thicknesses than in the β-$FeSi_2$ case. The larger errors incorporated into the FeSi thickness data prevented an analysis like that done for β-$FeSi_2$ and no equations were fitted to the FeSi data. Lacking strong experimental support for parabolic kinetics, Figures 4-11 to 4-13 show FeSi thickness simply as a function of time rather than of the square root of time.

4.2.4 Other Interesting Results

There were several other noteworthy observations gathered during the bulk diffusion couple investigation. One of these is that, after very long anneals, the β-$FeSi_2$ layer tends to be less uniform in thickness and appears to have undergone consumption by FeSi. The β-$FeSi_2$ begins to get thinner at some point in time and, eventually, it virtually disappears. Figure 4-14, taken from the diffusion couple annealed at 750°C for 2070 hours, helps to illustrate this behavior. Large areas of Fe_3Si and FeSi are visible in the micrograph, but $FeSi_2$ is totally absent. There is an obvious band of voids running along and parallel to the interface with the Si. This band of voids is curiously even in thickness and is approximately $\frac{2}{3}$ the width of the $FeSi_2$ layer that would be expected from Figure 4-8 to have formed after this annealing time.

Another micrograph, from the 800°C 430 hour couple, gave clues as to the explanation for the $FeSi_2$ consumption. Figure 4-15 shows all three silicides present in that couple. The β-$FeSi_2$ layer is very uneven however, and contains a sudden step change in thickness not seen anywhere in any of the 5 couples annealed at this same temperature for shorter times. In this 430 hour couple though, numerous sudden decreases in the layer thickness were seen along the interface. The sudden decreases, or even total disappearances of the $FeSi_2$ layer did not correspond to any visible features such as interface ends or cracks. It is also interesting to note that in Figure 4-15, a band of heavily voided FeSi continues along the Si interface from where the β-$FeSi_2$ leaves off, and is the same thickness as the β-$FeSi_2$ layer. Pictures such as these have led to the belief that the β-$FeSi_2$ layer, after some temperature-dependent time, begins to be consumed by the FeSi.

The occurrence of β-$FeSi_2$ consumption is the reason for the lack of error bars on the 800°C 430 hour data point in Figure 4-9. Consumption of the β-$FeSi_2$ would have caused the mean thickness to be misleadingly low if the whole interface had been used in arriving at an average value. Therefore, this data point was estimated from small segments of the β-$FeSi_2$ layer that were still very uniform in thickness and appeared to represent the thickness of the layer in the absence of the consumption phenomenon.

It is thought that the β-$FeSi_2$ consumption may be a result of disruptions in the Si supply caused by stresses generated as the silicides grow. As the layers thicken, shear stresses parallel to the interfaces may build. From observations of the diffusion couples, the Si/β-$FeSi_2$ and Fe_3Si/α-Fe interfaces seem like the most likely sites for the relief of stresses in this plane. These two interfaces were often observed to have separated during post-anneal cooling, possibly because of differences in thermal expansivities. The inter-silicide interfaces were never seen separated. So it is possible that shifting along these interfaces occurred after very long annealing periods. The plastic Fe could easily accommodate such movements rapidly, but movements between the brittle Si and β-$FeSi_2$ phases could lead to loss of Si flux for a significant time, long enough perhaps to allow the Fe flux to advance the FeSi through most of the β-$FeSi_2$. Figure 4-16 illustrates this situation schematically.

The recognition of β-$FeSi_2$ consumption is useful because it reveals a limitation on the annealing period of such diffusion couples if they are to yield meaningful growth kinetics results.

It was also observed in several couples that small bits of iron silicides had formed between the steel plates and Si. All three silicides (Fe_3Si, FeSi and β-$FeSi_2$) formed from the steel and Si, and EDS analysis detected no difference between these silicides and those

formed between the pure Fe and Si. The Fe/Si atomic ratios were unaffected by the presence of the other elements, among them carbon.

Finally, the backscattered electron signal of the SEM was able to provide contrast between individual grains in some cases, especially with FeSi. Figure 4-14 is one example of a condition where grains were clearly distinguishable.

4.3 Conclusions and Recommendations

The work on the bulk Fe-Si diffusion couples has led to the listed conclusions:

(1) The procedure developed for constructing Fe-Si bulk diffusion couples was very successful. Of 17 couples made, all produced continuous layers of iron silicides.

(2) The same three iron silicides -- β-$FeSi_2$, FeSi and Fe_3Si -- formed in all couples at 710°C, 750°C and 800°C.

(3) In agreement with previous research, β-$FeSi_2$ and FeSi were found to be stoichiometric phases with almost no compositional ranges.

(4) In disagreement with the present Fe-Si phase diagram, Fe_3Si is also concluded to be a stoichiometric silicide with no detectable range of composition.

(5) The solubility limit of Si in α-Fe was ~5% (atomic), only about half of what is predicted in the binary phase diagram.

(6) β-$FeSi_2$ demonstrated parabolic growth kinetics.

(7) Although growth data for FeSi was collected, results could not conclusively show the kinetics to be parabolic.

(8) The parabolic rate constant for β-$FeSi_2$ growth, k, was calculated to be

$$k = \frac{dx}{d(\sqrt{t})} = 14070 \cdot e^{(-80400 / RT)} \quad \mu m / \sqrt{hour} \qquad (6).$$

The activation energy for the growth process was 80.4 kJ/mol or 0.83 eV.

(9) There is a limit to the useful annealing time of such diffusion couples, if they are to provide kinetic growth data. Disturbances in the Si flux during very long anneals affect the kinetics, and the final layer thicknesses, in ways that cannot be accounted for.

One obvious extension of this bulk diffusion couple work would concern the Fe_3Si. Further investigation is needed to reconcile results of this research with the 0-25% (atomic) Si region of the Fe-Si phase diagram.

Also, the earliest stages of growth in a Fe-Si bulk diffusion couple are of interest because the initial kinetics and order of phase formation are not understood. The bulk couples of this study had interfaces that were too rough and contaminated for examination of the initial silicide formation behaviour. In order to observe this early silicide growth, a thick film of pure Fe, perhaps several μm thick, could be deposited onto an atomically clean Si substrate surface. This material could then be annealed for various times at a number of temperatures and the kinetics investigated by cross-sectional TEM.

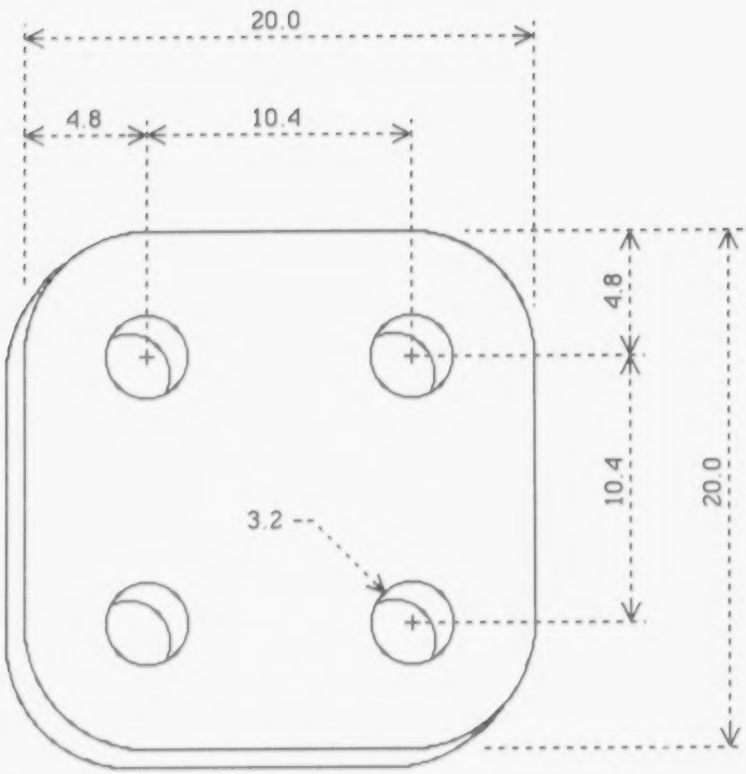

Figure 4-1. Diagram of steel clamp plate for bulk diffusion couple. Dimensions are in mm. Plate thickness was approximately 2 mm.

Figure 4-2. Backscattered electron image of a Fe-Si bulk diffusion couple.

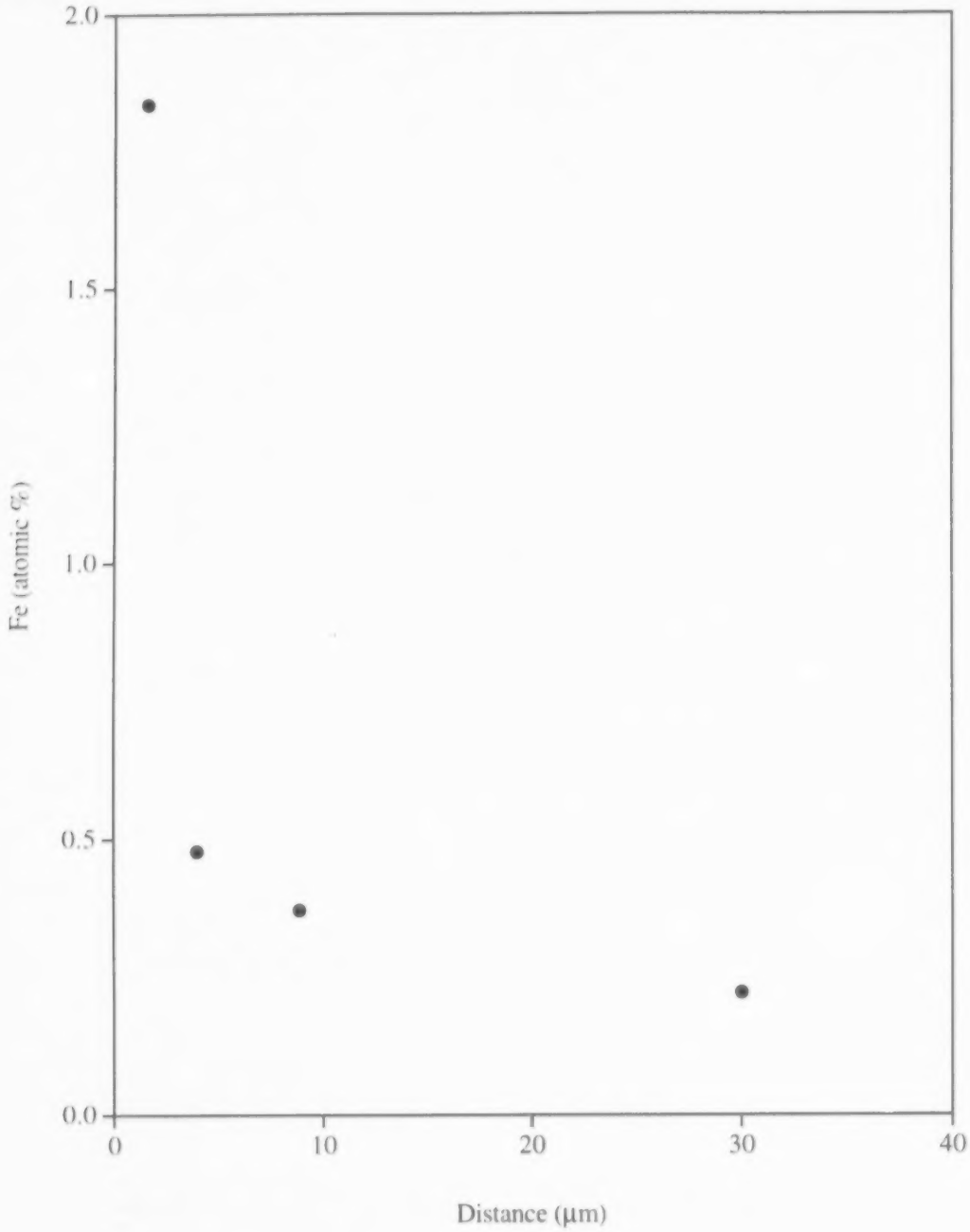

Figure 4-3. Fe concentration profile in the Si of a bulk diffusion couple. This couple was annealed for 1518 hours at 710°C. Distances are measured from the β-$FeSi_2$/Si interface. The data point of highest Fe content was likely obtained too close to the interface to avoid detecting Fe in the β-$FeSi_2$.

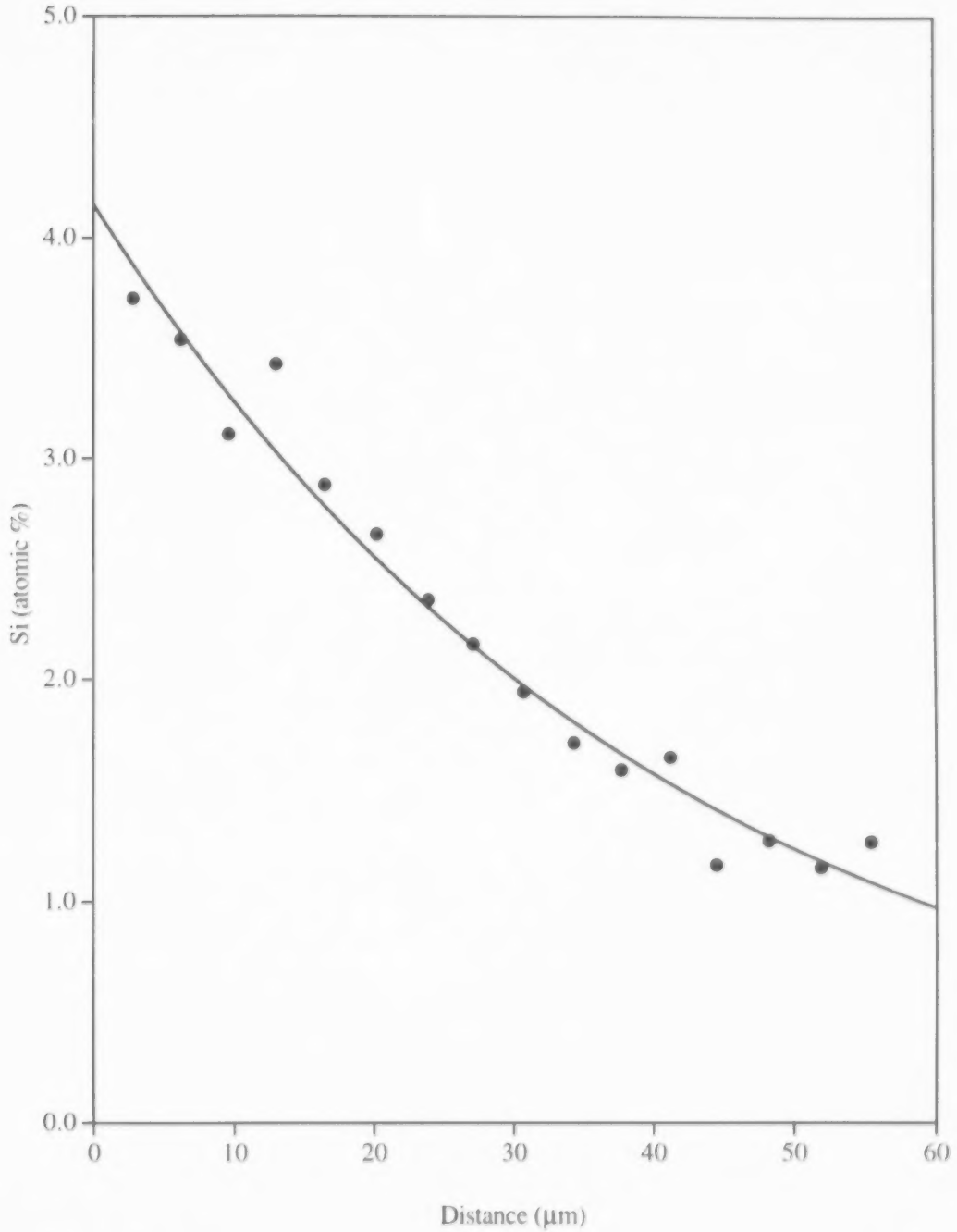

Figure 4-4. Si concentration profile in the α-Fe of a bulk diffusion couple. This couple was annealed for 211 hours at 800°C. Distances are measured from the edge of the α-Fe. The line is an exponential equation fitted to the experimental data.

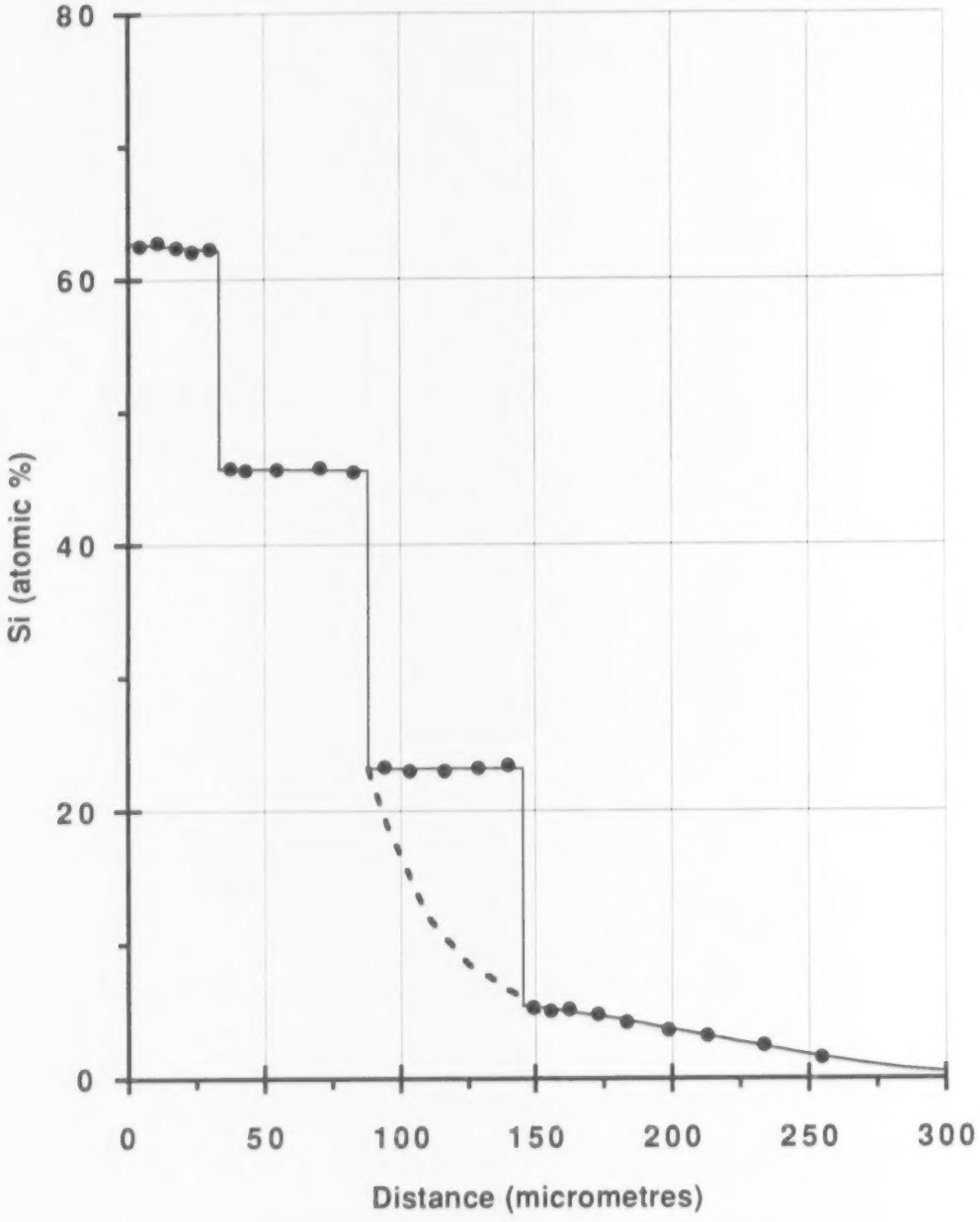

Figure 4-5. Experimental and theoretical concentration profiles across Fe-Si bulk diffusion couples. These experimental EDS data points are from a diffusion couple annealed at 800°C for 357 hours. The solid profile is a combination of equations that were fit to the EDS points. The theoretical profile, represented by the dashed line, deviates from the experimental results in the Fe_3Si region.

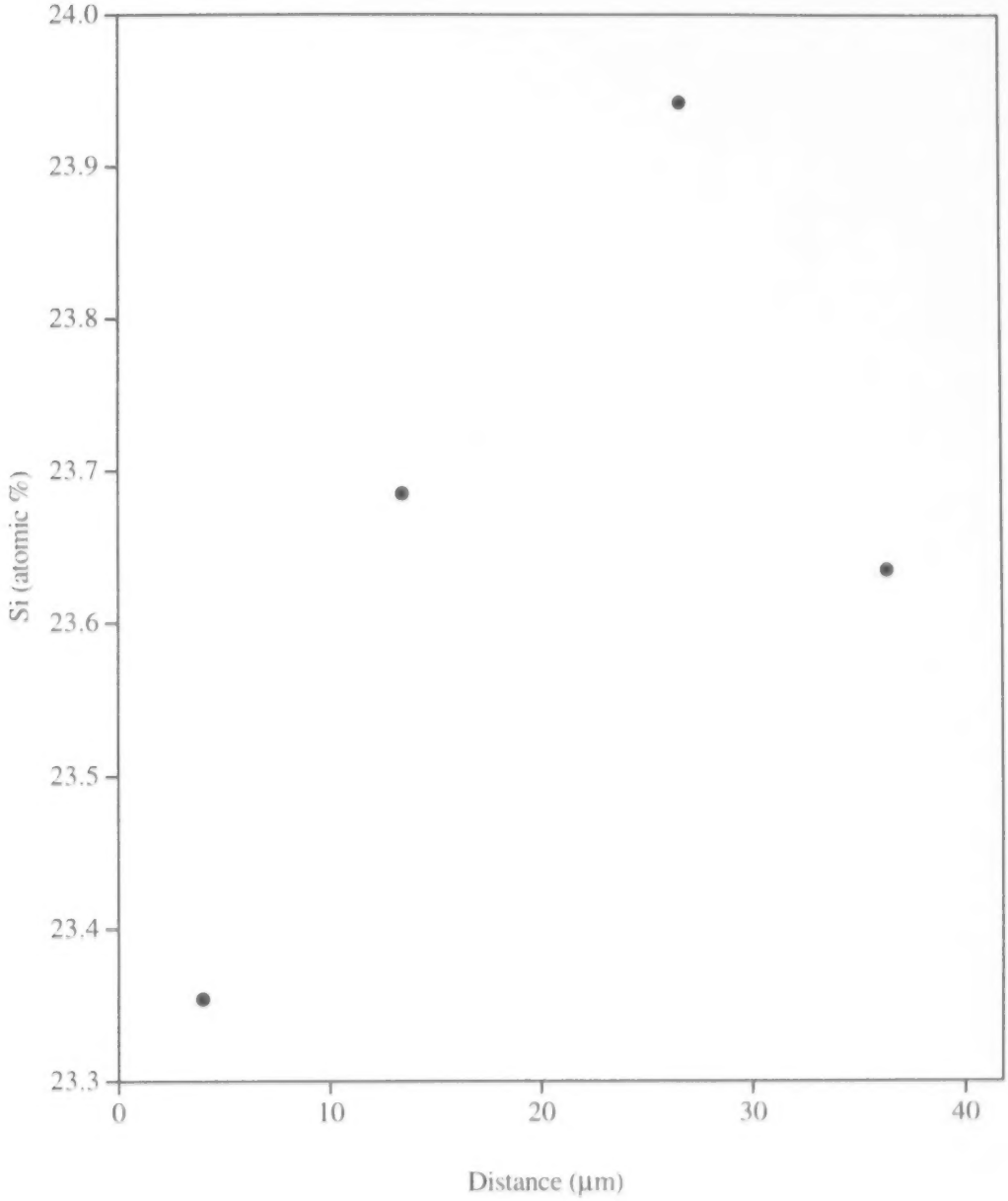

Figure 4-6. Compositional profile across Fe_3Si of a bulk diffusion couple annealed at 710°C for 1518 hours. The entire width of the Fe_3Si layer, about 42 μm, is represented by the graph. The virtually constant composition of the silicide is believed to be ~25% Si, slightly higher than the data would seem to suggest. The EDS data are thought to all contain an error that originates from an inaccuracy in the standard spectrum used to quantify the raw data.

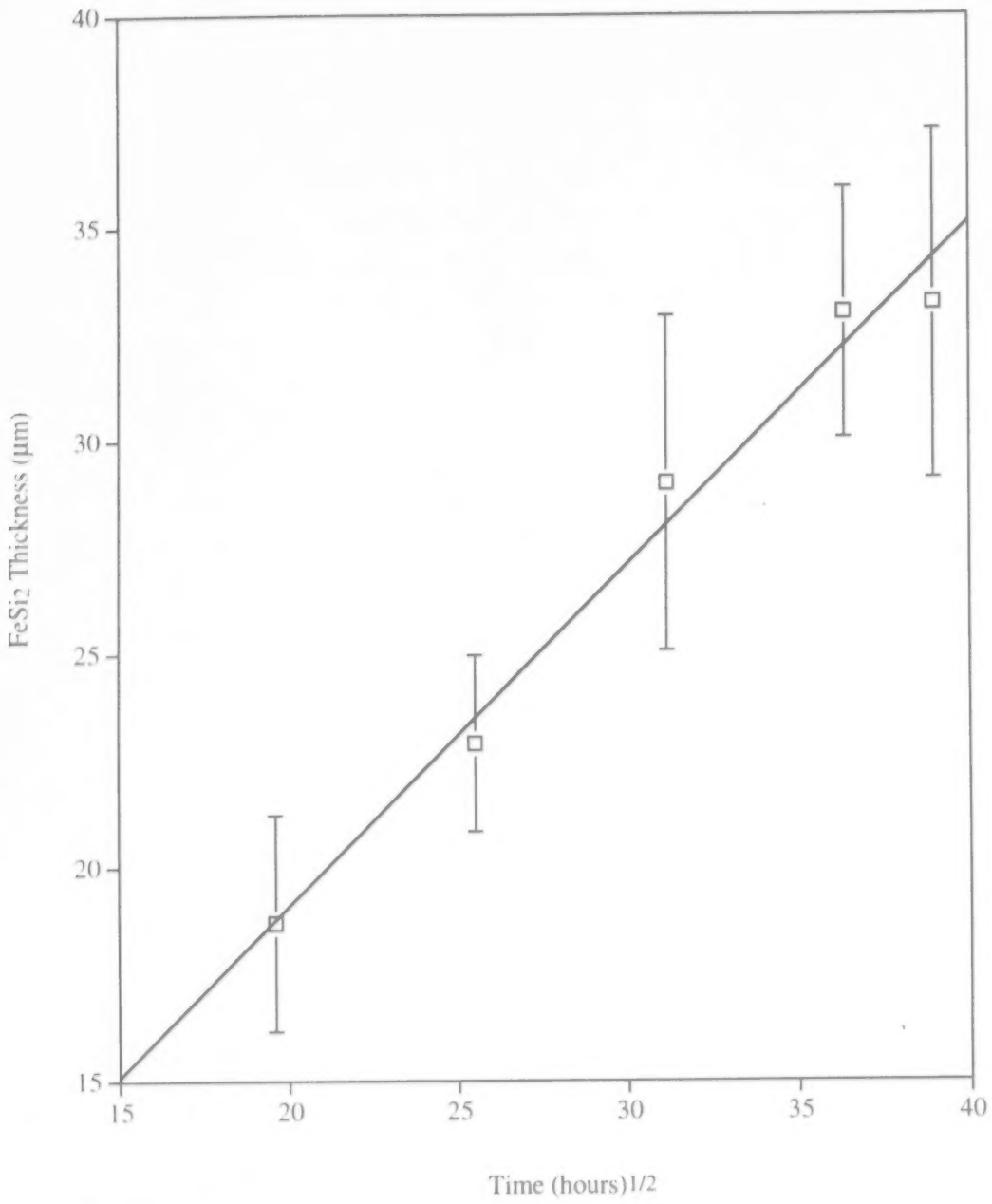

Figure 4-7. β-$FeSi_2$ layer thickness as a function of annealing time at 710°C in bulk diffusion couples. The thicknesses are plotted against the square root of time. The linear regression shows the kinetics to be parabolic. Error bars represent one standard deviation (±) in the thickness measurements.

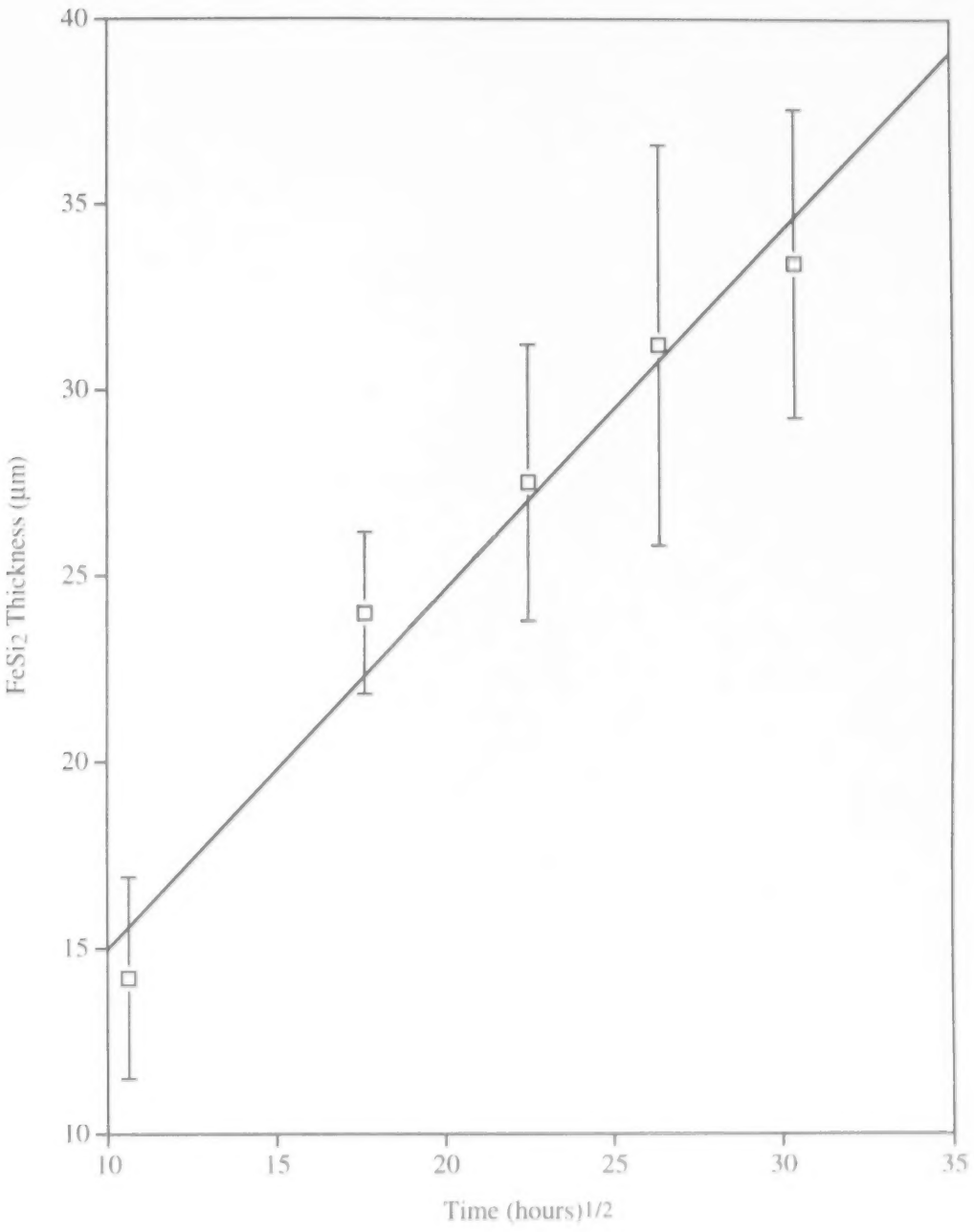

Figure 4-8. β-$FeSi_2$ layer thickness as a function of annealing time at 750°C in bulk diffusion couples. The thicknesses are plotted against the square root of time. The linear regression shows the kinetics to be parabolic. Error bars represent one standard deviation (±) in the thickness measurements.

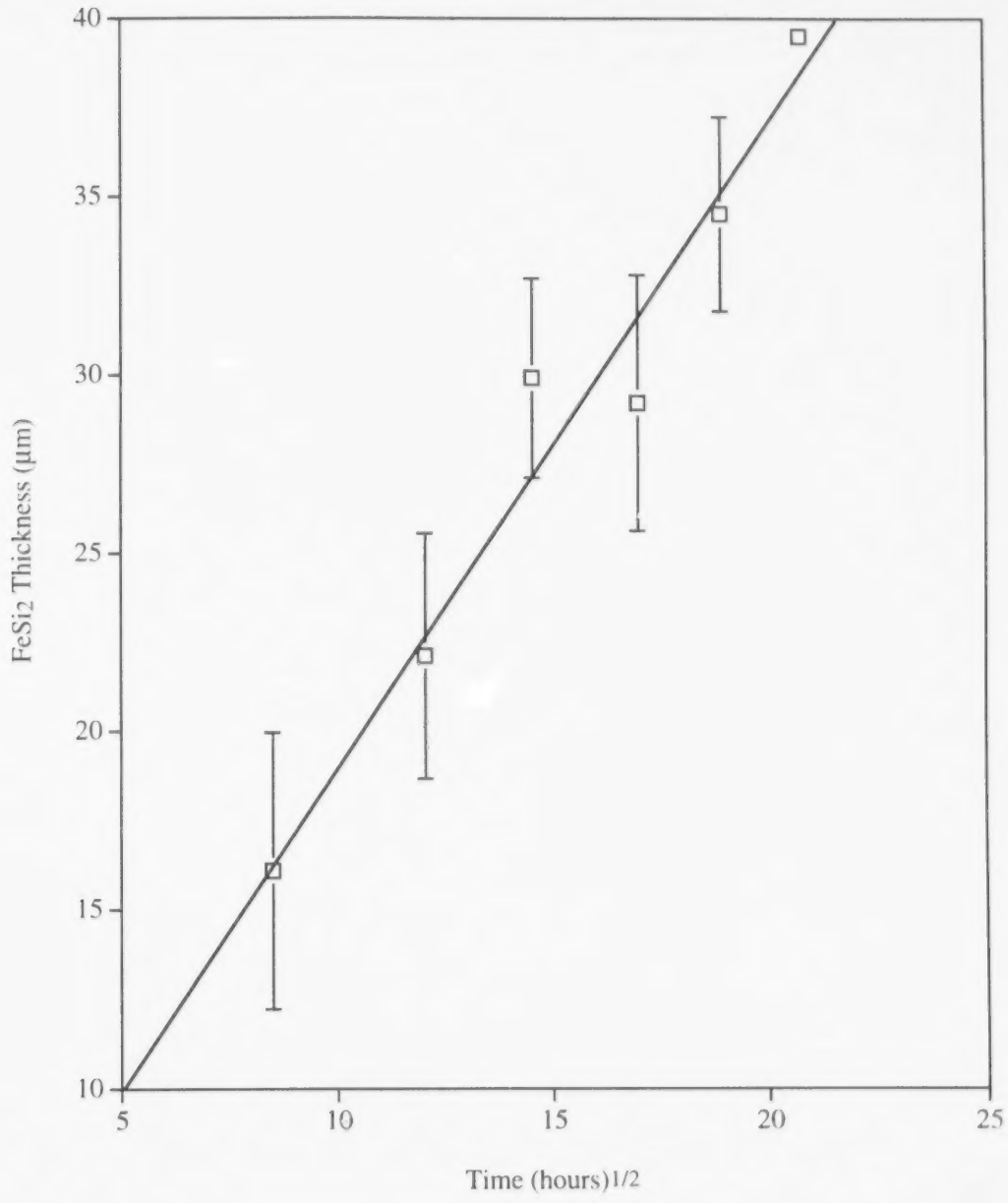

Figure 4-9. β-$FeSi_2$ layer thickness as a function of annealing time at 800°C in bulk diffusion couples. The thicknesses are plotted against the square root of time. The linear regression shows the kinetics to be parabolic. Error bars represent one standard deviation (±) in the thickness measurements. It was not possible to calculate an error for the last data point, as explained in the text.

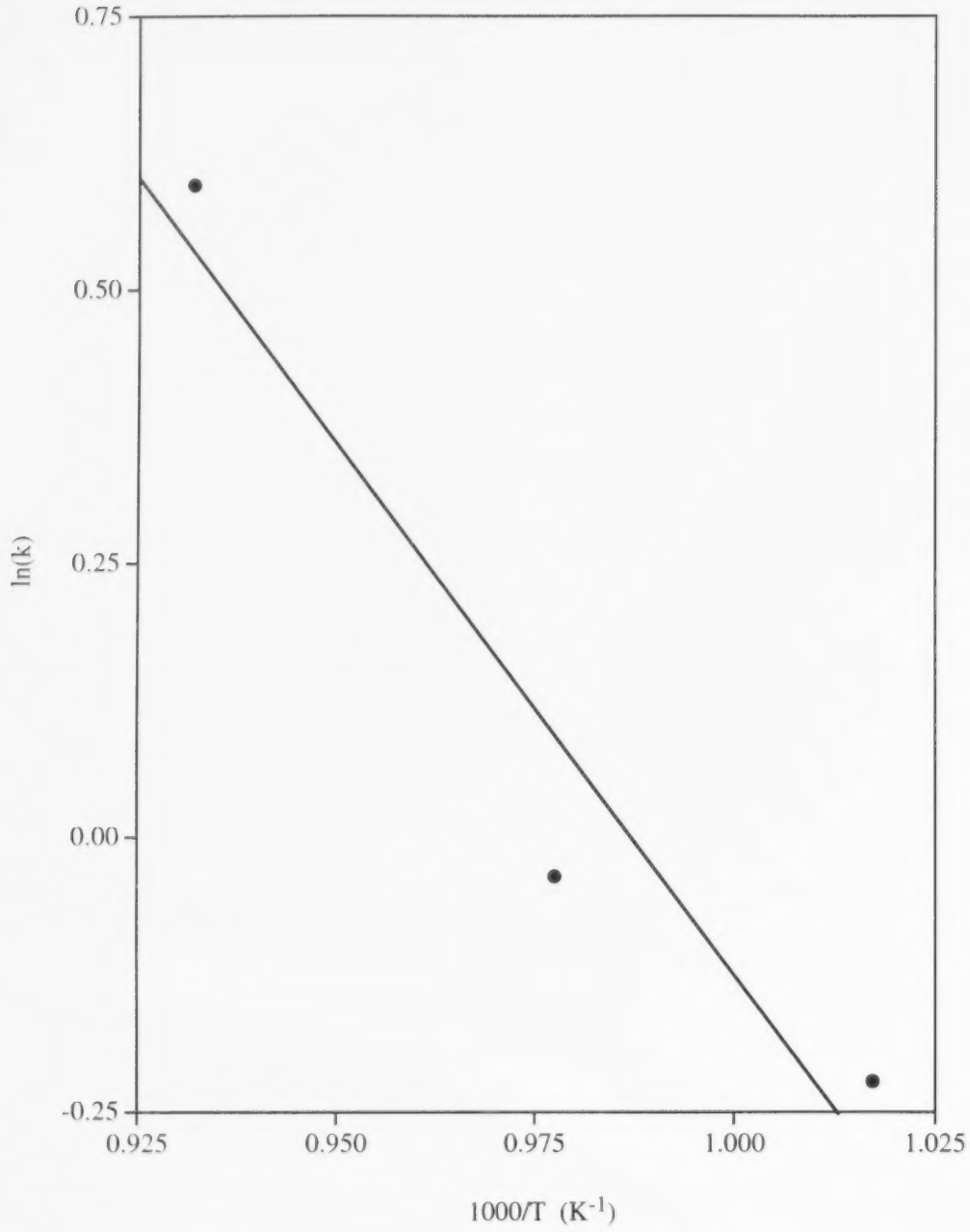

Figure 4-10. Plot to determine the activation energy of β-$FeSi_2$ growth in the bulk diffusion couples. The natural logarithm of the parabolic rate constant (k) is linear with the reciprocal of absolute temperature (T) according to Equation 4. The activation energy is calculated to be 80.4 kJ/mol or 0.83 eV.

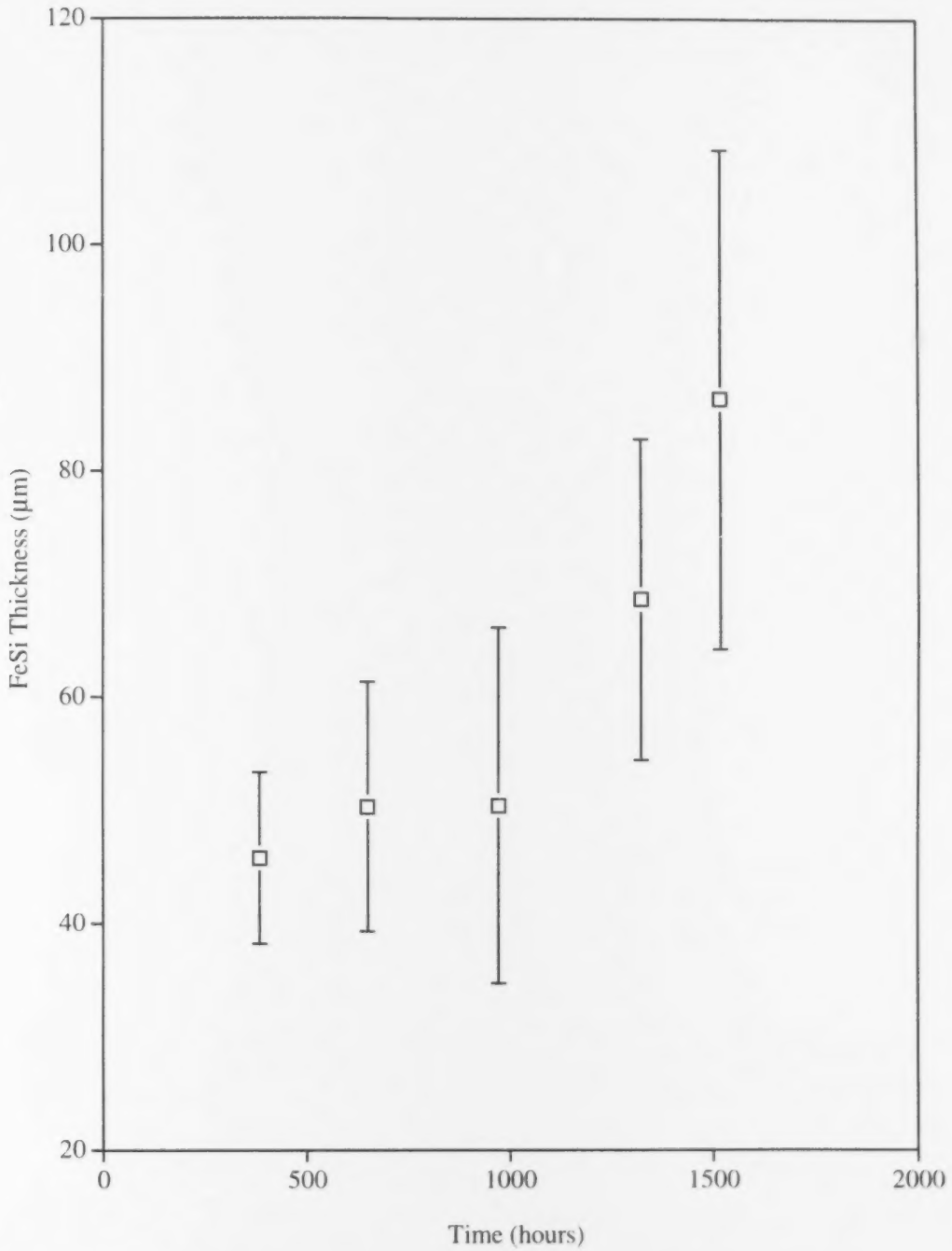

Figure 4-11. FeSi layer thickness as a function of annealing time at 710°C in bulk diffusion couples. Error bars represent one standard deviation (±) in the thickness measurements.

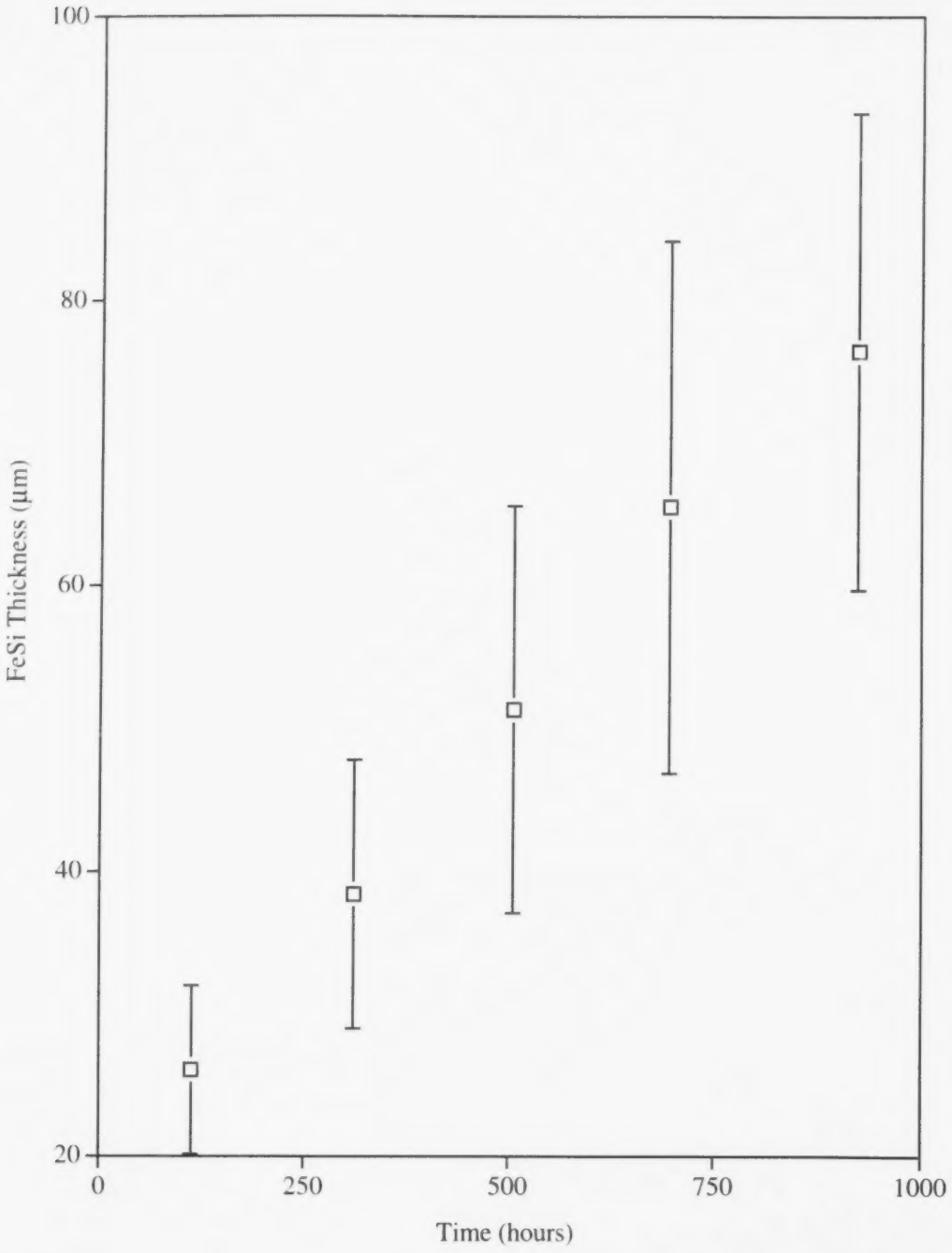

Figure 4-12. FeSi layer thickness as a function of annealing time at 750°C in bulk diffusion couples. Error bars represent one standard deviation (±) in the thickness measurements.

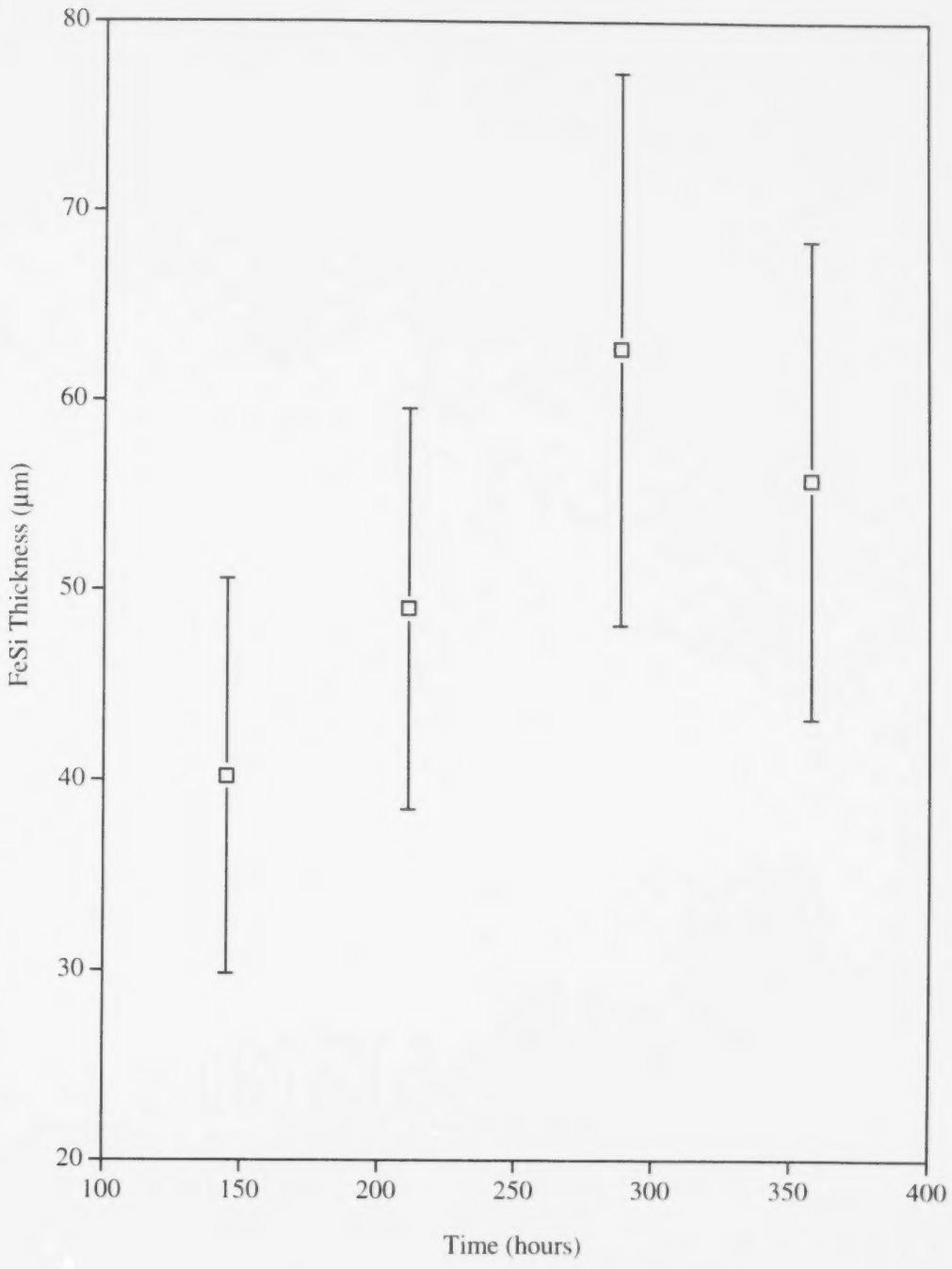

Figure 4-13. FeSi layer thickness as a function of annealing time at 800°C in bulk diffusion couples. Error bars represent one standard deviation (±) in the thickness measurements.

Figure 4-14. Backscattered electron image of bulk diffusion couple with β-$FeSi_2$ locally consumed. This couple was annealed for 2070 hours at 750°C.

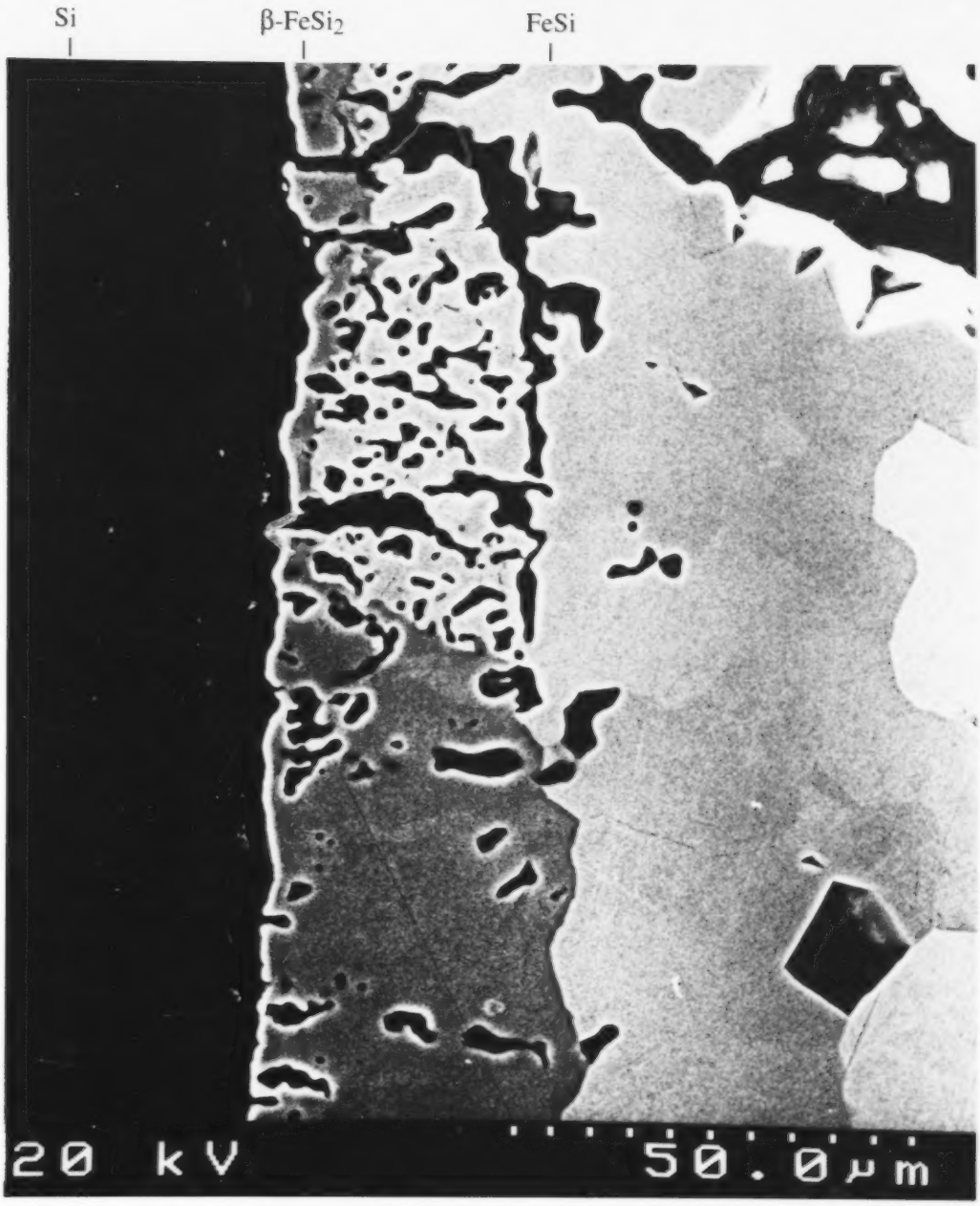

Figure 4-15. Secondary electron image of bulk diffusion couple with step change in β-$FeSi_2$ layer thickness.

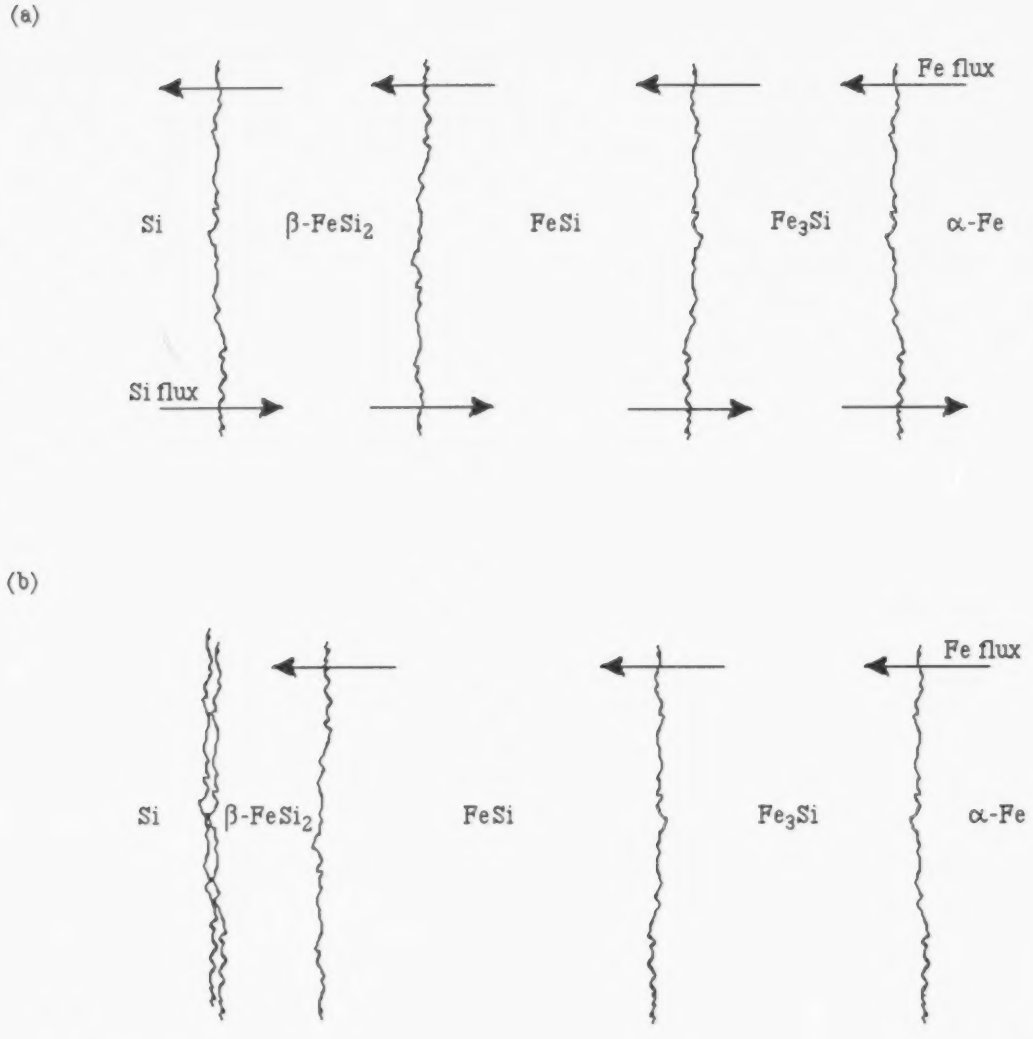

Figure 4-16. Schematic explaining the consumption of the β-$FeSi_2$ layer in bulk diffusion couples subjected to sufficiently long anneals. In (a) there is continuous contact along the Si/β-$FeSi_2$ interface and both Fe and Si diffuse across all the interfaces. In (b) recent displacement at the Si/β-$FeSi_2$ interface has reduced the contact area between the two phases. The diffusion of Si is greatly reduced while the diffusion of Fe continues as in (a). The Fe-Si diffusion couple has effectively become a Fe-β-$FeSi_2$ couple and FeSi and Fe_3Si grow thicker at the expense of β-$FeSi_2$ and Fe.

Chapter 5 Comparison of Thin Film and Bulk Diffusion Couple Results

The thin film diffusion couple results are in good agreement with the results of the bulk diffusion couple work. The same three iron silicides, Fe_3Si, FeSi and β-$FeSi_2$, were observed in both cases. In both situations, the three silicides were arranged in the couples in the expected order. Closest to the Si was the β-$FeSi_2$, which was adjacent to the FeSi, which was followed by the Fe_3Si.

In the bulk diffusion couples, the maximum solubility of Si in α-Fe was found to be about 5 atomic percent. In the thin film couples, there was considerable Si dissolved in the iron film, although accurate determination of the Si content was not possible. As expected, the solubility of Fe in Si was very low in both types of couples.

The bulk diffusion couples contained all three silicide phases, which grew simultaneously, while the thin film couples were observed to have at most two silicides present at the same time. The most significant cause of this difference is the limitless supply of iron in the bulk case versus the very limited supply of iron in the thin film case. In the thin film experiments many samples were annealed at temperatures too low to nucleate β-$FeSi_2$. Those films that were annealed at sufficient temperatures ($\geq$600°C) to produce β-$FeSi_2$, exhausted their supplies of iron very rapidly and the Fe_3Si (assuming it formed) was then consumed by the other silicides. At these higher temperatures, annealing times could not be made short enough to find Fe_3Si remaining in the films. In the bulk diffusion couples, Fe_3Si grows into the Fe layer as it is consumed by the FeSi.

In contrast to the information given by the phase diagram, Fe_3Si in the bulk diffusion couples was found to have a constant 3:1 stoichiometry. The thin film EDS analyses of Fe_3Si were not quantitatively accurate but they did indicate little variability in the stoichiometry of the phase in thin film form as well.

References

1 O. Kubaschewski, *Iron--Binary Phase Diagrams*, Springer-Verlag, New York (1982), p. 136.

2 M. C. Bost and J. E. Mahan, J. Appl. Phys. **58**, 2696 (1985).

3 M. C. Bost and J. E. Mahan, J. Appl. Phys. **64**, 2034 (1988).

4 A. Rizzi, H. Moritz, and H. Lüth, in SPIE Vol. 1361, 827 (1990).

5 A. Rizzi, H. Moritz, and H. Lüth, J. Vac. Sci. Technol. A **9**, 912 (1991).

6 K. Lefki, P. Muret, N. Cherief, and R. C. Cinti, J. Appl. Phys. **69**, 352 (1991).

7 M. De Crescenzi, G. Gaggiotti, N. Motta, F. Patella, A. Balzarotti, G. Mattogno, and J. Derrien, Surf. Sci. **251/252**, 175 (1991).

8 C. A. Dimitriadis and J. H. Werner, J. Appl. Phys. **68**, 93 (1990).

9 N. E. Christensen, Phys. Rev. B **42**, 7148 (1990).

10 W. Raunau, H. Niehus, T. Schilling, and G. Comsa, Surf. Sci. **286**, 203 (1993).

11 W. Raunau, H. Niehus, and G. Comsa, Surf. Sci. Lett. **284**, L375 (1993).

12 M. Powalla and K. Herz, Appl. Surf. Sci. **70/71**, 593 (1993).

13 Ch. Stuhlmann, J. Schmidt, and H. Ibach, J. Appl. Phys. **72**, 5905 (1992).

14 K. Radermacher, O. Skeide, R. Carius, J. Klomfaß, and S. Mantl, Mat. Res. Soc. Symp. Proc. **320**, 115 (1994).

15 B. Rösen, D. Freundt, Ch. Dieker, D. Gerthsen, A. Rizzi, R. Carius, and H. Lüth, Mat. Res. Soc. Symp. Proc. **320**, 139 (1994).

16 M. Powalla and K. Herz, Appl. Surf. Sci. **65/66**, 482 (1993).

17 H. C. Cheng, L. J. Chen, and T. R. Your, Mat. Res. Soc. Symp. Proc. **25**, 441 (1984).

18 K. Takayanagi, Y. Tanishiro, M. Takahashi, and S. Takahashi, J. Vac. Sci. Technol. A **3**, 1502 (1985).

19 A. Brodde, E. Harazim, R. Kliese, B. Röttger, and H. Neddermeyer, Ber. Bunsenges. Phys. Chem. **95**, 1434 (1991).

20 L. J. Chen and K. N. Tu, *Epitaxial Growth of Transition-Metal Silicides on Silicon*, North-Holland, Amsterdam (1991).

21 H. C. Cheng, T. R. Yew, and L. J. Chen, J. Appl. Phys. **57**, 5246 (1985).

22 H. von Känel, K. A. Mäder, E. Müller, N. Onda, and H. Sirringhaus, Phys. Rev. B, **45**, 13807 (1992).

23 Y. Dusausoy, J. Protas, R. Wandji, and B. Roques, Acta. Cryst. **B27**, 1209 (1971).

24 R. Eppenga, J. Appl. Phys. **68**, 3027 (1990).

25 N. Onda, J. Henz, E. Müller, H. von Känel, C. Schwarz, and R. E. Pixley, Helv. Phys. Acta **64**, 197 (1991).

26 J. Chevrier, V. Le Thanh, S. Nitsche, and J. Derrien, Appl. Surf. Sci. **56-58**, 438 (1992).

27 J. Alvarez, J. J. Hinarejos, E. G. Michel, and R. Miranda, Surf. Sci. **287/288**, 490 (1993).

28 U. Kafader, C. Pirri, P. Wetzel, and G. Gewinner, Appl. Surf. Sci. **64**, 297 (1993).

29 M. G. Grimaldi, P. Baeri, C. Spinella, and S. Lagomarsino, Appl. Phys. Lett. **60**, 1132 (1992).

30 N. Onda, J. Henz, E. Müller, K. A. Mäder, and H. von Känel, Appl. Surf. Sci. **56-58**, 421 (1992).

31 X. W. Lin, J. Desimoni, H. Bernas, Z. Liliental-Weber, and J. Washburn, Mat. Res. Soc. Symp. Proc. **311**, 293 (1993).

32 R. Kern, G. Le Lay, and J. J. Metois, in E. Kaldis (ed.), *Current Topics in Materials Science*, North-Holland, Amsterdam (1979), p. 153.

33 T. Urano, T. Ogawa, T. Kanaji, and F. Fujimoto, J. Vac. Sci. Technol. A **5**, 2046 (1987).

34 T. Urano and T. Kanaji, Appl. Surf. Sci. **33/34**, 68 (1988).

35 S. Kennou, N. Cherief, R. C. Cinti, and T. A. Nguyen Tan, Surf. Sci. **211/212**, 685 (1989).

36 J. M. Gallego and R. Miranda, J. Appl. Phys. **69**, 1377 (1991).

37 J. M. Gallego, J. Alvarez, J. J. Hinarejos, E. G. Michel, and R. Miranda, Surf. Sci. **251/252**, 59 (1991).

38 S. Lagomarsino, F. Scarinci, G. Savelli, C. Giannini, P. Castrucci, and M. G. Grimaldi, J. Appl. Phys. **71**, 1224 (1992).

39 K. N. Tu, G. Ottaviani, U. Gösele, and H. Föll, J. Appl. Phys. **54**, 758 (1983).

40 S. S. Lau, J. S. -Y. Feng, J. O. Olowolafe, and M. -A. Nicolet, Thin Solid Films **25**, 415 (1975).

41 J. Alvarez, J. J. Hinarejos, E. G. Michel, J. M. Gallego, A. L. Vazquez de Parga, J. de la Figuera, C. Ocal, and R. Miranda, Appl. Phys. Lett. **59**, 99 (1991).

42 Q. -G. Zhu, H. Iwasaki, E. D. Williams, and R. L. Park, J. Appl. Phys. **60**, 2629 (1986).

43 N. Cherief, C. D'Anterroches, R. C. Cinti, T. A. Nguyen Tan, and J. Derrien, Appl. Phys. Lett. **55**, 1671 (1989).

44 S. Degroote, M. H. Langelaar, T. Kobayashi, J. Dekoster, J. De Wachter, R. Moons, L. Niesen, and G. Langouche, Mat. Res. Soc. Symp. Proc. **320**, 133 (1994).

45 K. Radermacher, S. Mantl, Ch. Dieker, H. Lüth, and C. Freiburg, Thin Solid Films **215**, 76 (1992).

46 U. Erlesand, M. Östling, and K. Bodén, Appl. Surf. Sci. **53**, 153 (1991).

47 A. Goetzberger, Z. Phys. **142**, 182 (1955).

48 J. Alvarez, J. J. Hinarejos, E. G. Michel, and R. Miranda, Surf. Sci. **269/270**, 1011 (1992).

49 F. Namavar, F. H. Sanchez, J. I. Budnick, A. H. Fasihuddin, and H. C. Hayden, Mat. Res. Soc. Symp. Proc. **74**, 487 (1987).

50 X. W. Lin, J. Desimoni, H. Bernas, Z. Liliental-Weber, and J. Washburn, Mat. Res. Soc. Symp. Proc. **320**, 97 (1994).

51 D. J. Oostra, D. E. W. Vandenhoudt, C. W. T. Bulle-Lieuwma, and E. P. Naburgh, Appl. Phys. Lett. **59**, 1737 (1991).

52 T. D. Hunt, K. J. Reeson, R. M. Gwilliam, K. P. Homewood, R. J. Wilson, R. S. Spraggs, B. J. Sealy, C. D. Meekison, G. R. Booker, and P. Oberschachtsiek, Mat. Res. Soc. Symp. Proc. **260**, 239 (1992).

53 K. Radermacher, S. Mantl, Ch. Dieker, and H. Lüth, Appl. Phys. Lett. **59**, 2145 (1991).

54 D. Gerthsen, K. Radermacher, Ch. Dieker, and S. Mantl, J. Appl. Phys. **71**, 3788 (1992).

55 V. V. Tokarev, A. V. Kibardin, T. M. Pyatkova, and D. I. Zarovsky, Appl. Surf. Sci. **44**, 235 (1990).

56 H. Sirringhaus, N. Onda, E. Müller-Gubler, P. Müller, R. Stalder, and H. von Känel, Phys. Rev. B **47**, 10567 (1993).

57 H. Sirringhaus, N. Onda, E. Müller-Gubler, P. Müller, St. Zehnder, and H. von Känel, Surf. Sci. **287/288**, 1019 (1993).

58 H. von Känel, R. Stalder, H. Sirringhaus, N. Onda, and J. Henz, Appl. Surf. Sci. **53**, 196 (1991).

59 H. von Känel, U. Kafader, P. Sutter, N. Onda, H. Sirringhaus, E. Müller, U. Kroll, C. Schwarz, and S. Goncalves-Conto, Mat. Res. Soc. Symp. Proc. **320**, 73 (1994).

60 H. von Känel, N. Onda, H. Sirringhaus, E. Müller-Gubler, S. Goncalves-Conto, and C. Schwarz, Appl. Surf. Sci. **70/71**, 559 (1993).

61 K. M. Geib, J. E. Mahan, R. G. Long, M. Nathan, and G. Bai, J. Appl. Phys. **70**, 1730 (1991).

62 K. Konuma, J. Vrijmoeth, P. M. Zagwijn, E. Vlieg, and J. F. van der Veen, Appl. Surf. Sci. **70/71**, 564 (1993).

63 O. P. Karpenko, C. H. Olk, G. L. Doll, J. F. Mansfield, and S. M. Yalisove, Mat. Res. Soc. Symp. Proc. **320**, 103 (1994).

64 X. Wallart, J. P. Nys, O. Dehaese, and G. Vincent, Appl. Surf. Sci. **70/71**, 598 (1993).

65 J. E. Mahan, K. M. Geib, G. Y. Robinson, R. G. Long, Y. Xinghua, G. Bai, M. - A. Nicolet, and M. Nathan, Appl. Phys. Lett. **56**, 2126 (1990).

66 L. J. Chen, W. Lur, and J. Y. Cheng, Thin Solid Films **191**, 221 (1990).

67 D. Snell and D. G. Ivey, J. Mater. Sci. Mater. in Electr. **4**, 47 (1993).

68 F. Sirotti, M. DeSantis, X. Jin, and G. Rossi, Appl. Surf. Sci. **65/66**, 800 (1993).

69 D. J. Srolovitz and S. A. Safran, J. Appl. Phys. **60**, 247 (1986).

70 K. T. Miller, F. F. Lange, and D. B. Marshall, J Mater. Res. **5**, 151 (1990).

71 T. P. Nolan, R. Sinclair, and R. Beyers, J. Appl. Phys. **71**, 720 (1992).

72 H. C. Cheng, T. R. Yew, and L. J. Chen, Appl. Phys. Lett. **47**, 128 (1985).

73 D. G. Ivey and D. Wang, Can. J. Phys. **70**, 860 (1992).

74 G. Ottaviani, J. Vac. Sci. Technol. **16**, 1112 (1979).

75 G. Ottaviani and C. Nobili, Thin Solid Films **163**, 111 (1988).

76 H. C. Swart and G. L. P. Berning, Appl. Surf. Sci. **78**, 77 (1994).

77 C. Chemelli, D. D'Angelo, G. Girardi, and S. Pizzini, Appl. Surf. Sci. **68**, 173 (1993).

78 L. Zhang and D. G. Ivey, J. Appl. Phys. **71**, 4314 (1992).

79 L. Zhang and D. G. Ivey, Mat. Res. Soc. Symp. Proc. **260**, 257 (1992).

80 L. Zhang, Ph.D. Thesis, University of Alberta (1993).

81 L. Zhang and D. G. Ivey, Mat. Res. Soc. Symp. Proc. **311**, 299 (1993).

82 L. Zhang and D. G. Ivey, Thin Solid Films **245**, 234 (1994).

83 L. Zhang and D. G. Ivey, Can. Metall. Q., accepted June, 1994.

84 U. Gösele and K. N. Tu, J. Appl. Phys. **53**, 3252 (1982).

85 K. N. Tu, Ann. Rev. Mater. Sci. **15**, 147 (1985).

86 U. Gösele and K. N. Tu, J. Appl. Phys. **66**, 2619 (1989).

87 R. M. Walser and R. W. Bené, Appl. Phys. Lett. **28**, 624 (1976).

88 R. W. Bené, J. Appl. Phys. **61**, 1826 (1987).

89 F. M. d'Heurle and P. Gas, J. Mater. Res. **1**, 205 (1986).

90 F. M. d'Heurle, J. Vac. Sci. Technol. A **7**, 1467 (1989).

91 G. Ottaviani, Thin Solid Films **140**, 3 (1986).

92 R. Pretorius, Mater. Res. Soc. Symp. Proc. **25**, 15 (1984).

93 R. Pretorius, Vacuum **41**, 1038 (1990).

94 R. Pretorius, A. M. Vredenberg, F. W. Saris, and R. de Reus, J. Appl. Phys. **70**, 3636 (1991).

95 Y. Zheng, A. Taccoen, M. Gandais, and J. F. Pétroff, J. Appl. Cryst. **26**, 388 (1993).

96 T. Rosenqvist, *Principles of Extractive Metallurgy (2nd. ed.)*, McGraw-Hill, New York (1983).

97 F. A. Shunk, *Constitution of Binary Alloys (2nd. supplement)*, McGraw-Hill, New York (1969).

Appendix A: Iron Silicide Atomic Lattice Positions

Lattice positions are given as fractions of the unit cell dimensions. All unit cell angles are 90°.

Table A-1: Lattice Positions of α-Fe (a=b=c=0.2866 nm)

Position #	X	Y	Z	Atom Present
1	0.0000	0.0000	0.0000	Fe
2	0.5000	0.5000	0.5000	Fe

Table A-2: Lattice Positions of α_2 Fe_3Si (a=b=c=0.284 nm)

Position #	X	Y	Z	Atom Present
1	0.0000	0.0000	0.0000	50% Si; 50% Fe
2	0.5000	0.5000	0.5000	Fe

Table A-3: Lattice Positions of $FeSi_{(CsCl)}$ (a=b=c)

Position #	X	Y	Z	Atom Present
1	0.0000	0.0000	0.0000	Fe
2	0.5000	0.5000	0.5000	Si

Table A-4: Lattice Positions of α_1 Fe_3Si (a=b=c=0.564 nm)

Position #	X	Y	Z	Atom Present
1	0.0000	0.0000	0.0000	Si
2	0.0000	0.5000	0.5000	Si
3	0.5000	0.0000	0.5000	Si
4	0.5000	0.5000	0.0000	Si
5	0.5000	0.5000	0.5000	Fe
6	0.5000	0.0000	0.0000	Fe
7	0.0000	0.5000	0.0000	Fe
8	0.0000	0.0000	0.5000	Fe
9	0.2500	0.2500	0.2500	Fe
10	0.2500	0.7500	0.7500	Fe
11	0.7500	0.7500	0.2500	Fe
12	0.7500	0.2500	0.7500	Fe
13	0.7500	0.7500	0.7500	Fe
14	0.7500	0.2500	0.2500	Fe
15	0.2500	0.7500	0.2500	Fe
16	0.2500	0.2500	0.7500	Fe

Table A-5: Lattice Positions of ε-FeSi (a=b=c=0.449 nm)

Position #	X	Y	Z	Atom Present
1	0.1370	0.1370	0.1370	Fe
2	0.6370	0.3630	0.8630	Fe
3	0.8630	0.6370	0.3630	Fe
4	0.3630	0.8630	0.6370	Fe
5	0.8420	0.8420	0.8420	Si
6	0.3420	0.6580	0.1580	Si
7	0.1580	0.3420	0.6580	Si
8	0.6580	0.1580	0.3420	Si

Table A-6: Lattice Positions of β-$FeSi_2$ (a=0.9863 nm b=0.7791 nm c=0.7833 nm)

Position #	X	Y	Z	Atom Present
1	0.2147	0.0000	0.0000	Fe
2	0.7854	0.0000	0.0000	Fe
3	0.2147	0.5000	0.5000	Fe
4	0.7854	0.5000	0.5000	Fe
5	0.7147	0.5000	0.0000	Fe
6	0.2854	0.5000	0.0000	Fe
7	0.7147	0.0000	0.5000	Fe
8	0.2854	0.0000	0.5000	Fe
9	0.0000	0.3086	0.3150	Fe
10	0.0000	0.6914	0.6850	Fe
11	0.5000	0.3086	0.1850	Fe
12	0.5000	0.6914	0.8150	Fe
13	0.5000	0.8086	0.3150	Fe
14	0.5000	0.1914	0.6850	Fe
15	0.0000	0.8086	0.1850	Fe
16	0.0000	0.1914	0.8150	Fe
17	0.1282	0.2747	0.0512	Si
18	0.1282	0.7254	0.9488	Si
19	0.1282	0.2254	0.5512	Si
20	0.1282	0.7747	0.4488	Si
21	0.8718	0.7254	0.9488	Si
22	0.8718	0.2747	0.0512	Si
23	0.8718	0.7747	0.4488	Si
24	0.8718	0.2254	0.5512	Si
25	0.6282	0.7747	0.0512	Si
26	0.6282	0.2254	0.9488	Si
27	0.6282	0.7254	0.5512	Si
28	0.6282	0.2747	0.4488	Si
29	0.3718	0.2254	0.9488	Si
30	0.3718	0.7747	0.0512	Si

Table A-6 (continued)

31	0.3718	0.2747	0.4488	Si
32	0.3718	0.7254	0.5512	Si
33	0.3727	0.0450	0.2261	Si
34	0.3727	0.9550	0.7739	Si
35	0.3727	0.4550	0.7261	Si
36	0.3727	0.5450	0.2739	Si
37	0.6273	0.9550	0.7739	Si
38	0.6273	0.0450	0.2261	Si
39	0.6273	0.5450	0.2739	Si
40	0.6273	0.4550	0.7261	Si
41	0.8727	0.5450	0.2261	Si
42	0.8727	0.4550	0.7739	Si
43	0.8727	0.9550	0.7261	Si
44	0.8727	0.0450	0.2739	Si
45	0.1273	0.4550	0.7739	Si
46	0.1273	0.5450	0.2261	Si
47	0.1273	0.0450	0.2739	Si
48	0.1273	0.9550	0.7261	Si

Table A-7: Lattice Positions of γ-$FeSi_2$ (a=b=c=0.539 nm)

Position #	X	Y	Z	Atom Present
1	0.0000	0.0000	0.0000	Fe
2	0.0000	0.5000	0.5000	Fe
3	0.5000	0.0000	0.5000	Fe
4	0.5000	0.5000	0.0000	Fe
5	0.2500	0.2500	0.2500	Si
6	0.2500	0.7500	0.7500	Si
7	0.7500	0.2500	0.7500	Si
8	0.7500	0.7500	0.2500	Si
9	0.7500	0.7500	0.7500	Si
10	0.7500	0.2500	0.2500	Si
11	0.2500	0.7500	0.2500	Si
12	0.2500	0.2500	0.7500	Si

Appendix B: Crystallographic Interplanar Spacings

Crystallographic interplanar spacings for the various phases are listed, by descending spacing, below. Only "allowed" reflections are included.

Table B-1: Crystallographic Interplanar Spacings for α-Fe

Distance (nm)	Planes	Distance (nm)	Planes
0.2029	110	0.0908	310
0.1435	200	0.0828	222
0.1172	211	0.0767	321
0.1015	220	0.0718	400

Table B-2: Crystallographic Interplanar Spacings for α_1 Fe_3Si

Distance (nm)	Planes	Distance (nm)	Planes	Distance (nm)	Planes
0.3256	111	0.1294	331	0.0953	531
0.2820	200	0.1261	420	0.0940	442
0.1994	220	0.1151	422	0.0940	600
0.1701	311	0.1085	511	0.0892	620
0.1628	222	0.1085	333	0.0860	533
0.1410	400	0.0997	440	0.0850	622

Table B-3: Crystallographic Interplanar Spacings for α_2 Fe_3Si

Distance (nm)	Planes	Distance (nm)	Planes	Distance (nm)	Planes
0.2840	100	0.1159	211	0.0856	311
0.2008	110	0.1004	220	0.0820	222
0.1640	111	0.0947	221	0.0788	320
0.1420	200	0.0947	300	0.0759	321
0.1270	210	0.0898	310	0.0710	400

Table B-4: Crystallographic Interplanar Spacings for FeSi

Distance (nm)	Planes	Distance (nm)	Planes	Distance (nm)	Planes
0.3175	110	0.1420	310	0.1089	322
0.2592	111	0.1354	311	0.1058	411
0.2245	200	0.1296	222	0.1030	331
0.2008	210	0.1245	320	0.1004	420
0.1833	211	0.1200	321	0.0980	421
0.1587	220	0.1123	400	0.0957	332
0.1497	221	0.1089	410	0.0917	422

Table B-5: Crystallographic Interplanar Spacings for β-$FeSi_2$

Distance (nm)	Planes	Distance (nm)	Planes	Distance (nm)	Planes
0.4930	200	0.3056	220	0.2395	312
0.4818	111	0.2847	221	0.2391	131
0.3915	002	0.2824	311	0.2168	023
0.3895	020	0.2761	022	0.2114	132
0.3487	021	0.2465	400	0.2086	402
0.3297	112	0.2409	222	0.2083	420
0.3066	202	0.2400	113	0.2013	421